Geoscience BC

MINERALS

Summary of Activities 2022

Geoscience BC Report 2023-01

Geoscience BC

GEOSCIENCE BC
SUMMARY OF ACTIVITIES 2022:
MINERALS

Geoscience BC Report 2023-01

This publication is also available, free of charge, as colour digital files in Adobe Acrobat® PDF format from the Geoscience BC website: http://www.geosciencebc.com/updates/summary-of-activities/.

When using information from this publication in other publications or presentations, due acknowledgment should be given to Geoscience BC. The recommended reference is included on the title page of each paper. The complete volume should be referenced as follows:

Geoscience BC (2023): Geoscience BC Summary of Activities 2022: Minerals; Geoscience BC, Report 2023-01, 78 p.

Summary of Activities: Minerals (Geoscience BC)
Annual publication

ISSN 2562-8623 (Print)
ISSN 2562-8631 (Online)

Geoscience BC
1101–750 West Pender Street
Vancouver, British Columbia V6C 2T7
Canada

Front cover photo and credit: A view across British Columbia’s Golden Triangle, captured during fieldwork conducted on Scottie Resources Corp. properties in 2022. Photo by A. Hutchison.

Foreword

It has been another busy and exciting year at Geoscience BC. We launched a membership program early in 2022 and introduced 'Project Concepts', which are outlines of future research programs, in July. And throughout, we continued to support leading-edge geoscience research in British Columbia, highlights of which are presented in our annual *Summary of Activities* publication. Papers are published in two separate volumes: *Energy and Water*, and this volume, *Minerals*. Both volumes are available in print and online via www.geosciencebc.com.

Summary of Activities 2022: Minerals

This *Summary of Activities 2022: Minerals* volume contains eight papers from ongoing Geoscience BC projects and 2022 Geoscience BC Scholarship recipients that are within Geoscience BC's strategic focus area of minerals. The papers are divided into two sections, based on Geoscience BC's strategic objectives of

1) Identifying New Natural Resource Opportunities, and
2) Advancing Science and Innovative Geoscience Technologies.

The 'Identifying New Natural Resource Opportunities' section starts off with Mitchinson introducing a new project that will integrate electromagnetic and gravity data to resolve the deep geology of the Quesnel terrane in central British Columbia (BC). This is followed by two Geoscience BC 2022 scholarship recipients examining mineral deposits in BC's Golden Triangle. Hutchison et al. consider the Blueberry zone of the Scottie Gold Mine project, and Ng et al. report on work at the Brucejack deposit of Newcrest Mining Ltd.

All five papers in the 'Advancing Science and Innovative Geoscience Technologies' section are led by Geoscience BC Scholarship 2022 recipients. Eaton et al. investigate the use of unsupervised machine learning to improve and expedite the identification of Cu-porphyry–related mineralization. Lu et al. consider the reactivity of ultramafic minerals and tailings for carbon capture and storage. Iulianella Phillips et al. contribute an update on using microbes as biosensors to see through overburden materials, and Hendi et al. consider the use of fibre-optic sensors in geoscience projects. Finally, Shapka-Fels summarizes the development and highlights results of selected Finite-Discrete Element Method models of Red Chris mine operations.

Geoscience BC Minerals Publications 2022

Geoscience BC published the following nine Minerals geoscience reports in 2022:

- Nine technical papers in the **Geoscience BC Summary of Activities 2021: Minerals** volume (Geoscience BC Report 2022-01)
- **Mineralogical and Geochemical Vectors within Advanced Argillic-Altered Rocks of British Columbia**, by F. Bouzari, R.G. Lee, C.J.R. Hart and B.I. van Straaten (Geoscience BC Report 2022-03/MDRU Publication 456)
- **A Geo-Exploration Atlas of the Mt. Milligan Porphyry Copper-Gold District**, by F.A.M. Devine, P. Kowalczyk and D.R. Heberlein (Geoscience BC Report 2022-04)
- **Identification of New Porphyry Potential Under Cover in British Columbia**, by D.E. Mitchinson, D. Fournier, C.J.R. Hart, T. Astic, D.C. Cowan and R.G. Lee (Geoscience BC Report 2022-07/MDRU Publication 457)
- **Surficial Geology, Drift Thickness and Till Sampling Suitability Maps (NTS 093A/13; 093G/01, 07, 09, 10, 16), British Columbia**, by Palmer (Geoscience BC Report 2022-08)
- **Geology and Mineral Potential of the Western Skeena Arch: Evolution of an Arc-Transverse Structural Corridor, West-Central British Columbia**, by J.J. Angen, C.J.R. Hart, J.L. Nelson and M. Rahimi (Geoscience BC Report 2022-09/BCGS Open File 2019-09/MDRU Publication 458)
- **Developments in the Real-Time Detection of Buried Mineralization and Geological Structures Using Soil Gas Concentrations**, by R.E. Lett, D.A. Sacco, E. Elder and C. Knox (Geoscience BC Report 2022-12)
- **Georeferencing and Data Capture of 2019–2021 National Instrument 43-101 Reports in British Columbia to Update the Existing Dataset**, by N.D. Barlow, J.R. Barlow and K.E. Flower (Geoscience BC Report 2022-13)
- **Summary Report on U-Pb and Ar-Ar Age Dating, Penticton Map Sheet (082E)**, by T. Höy, J. Gabites and R. Friedman (Geoscience BC Report 2022-16)

All releases of Geoscience BC reports, maps and data are published on our website and announced through our website and e-mail updates. Most final reports and data can be viewed or accessed through our Earth Science Viewer at https://gis.geosciencebc.com/esv/?viewer=esv.

Looking Forward: 2023 and Beyond

Project Concepts

As Geoscience BC looks ahead to 2023 and beyond, we are working with partners and members to develop project concepts: proposed research relating to critical minerals and metals, geological carbon capture and storage, generating cleaner energy (including geothermal, hydrogen and low carbon intensity natural gas), and monitoring and mitigating greenhouse gas emissions. These are designed for a collaborative funding model with input and contributions from federal and provincial governments, industry, trusts and others. Geoscience BC is currently applying for research funding and reaching out to prospective project sponsors for all project concepts.

New project concepts include 'Critical Minerals and Metals in BC Mine Tailings and Waste Rock Facilities', which would study tailings and waste rock from some of BC's current and past mining operations to see if they may host economic concentrations of critical minerals or metals, and new 'Regional-Scale Geophysical and Geochemical Surveys', which would help focus critical mineral and metal greenfields exploration in the province. Finally, the project concept 'CO_2 Storage in Ultramafic Rocks: Development of a Pilot-Scale Demonstration Project' would continue the development of an innovative method for storing carbon outside of sedimentary basins.

Membership

Geoscience BC membership opportunities make it easy for a wide range of partners to learn about new project concepts, as well as support, provide input, network and stay up to date on Geoscience BC minerals, energy and water research. Corporate, Individual, Student and Associate memberships provide a variety of opportunities to suit industry, academia, communities, Indigenous groups and governments as we work toward shared goals. Geoscience BC launched the membership program early in 2022 and, as of mid-December 2022, has 140 members.

Acknowledgments

Geoscience BC would like to thank all authors and reviewers of the *Summary of Activities* for their contributions to this volume. RnD Technical is also acknowledged for its work in editing and assembling both volumes.

Geoscience BC would like to thank all members, project sponsors and champions for their ongoing support of public geoscience. As well, Geoscience BC would like to express our appreciation for the leaders and volunteers in British Columbia's mineral exploration, mining and energy sectors who support our organization through their guidance and their use and recognition of the data and information that we collect and distribute.

Christa Pellett
Vice President, Minerals
Geoscience BC
www.geosciencebc.com

Contents

Identifying New Natural Resource Opportunities

D.E. Mitchinson: Integrated interpretation of electromagnetic and gravity data to resolve deep geology and aid mineral exploration in the Quesnel terrane, central British Columbia 1

A. Hutchison, M. Stewart, J. Hanley and R.C. Stewart: Timing and origin of gold mineralization in the Blueberry Zone of the Scottie Gold Mine project, Stikine terrane, northwestern British Columbia 13

K.M.H. Ng, A.E. Williams-Jones, D.F. McLeish, J.R. Clark and S. Wafforn: Insights from syn- to postmineralization dikes into the origin of the Brucejack high-grade gold-silver epithermal deposit, northwestern British Columbia 25

Advancing Science and Innovative Geoscience Technologies

B. Eaton, A. Steiner, S. Barker and L. Heagy: Investigating unsupervised machine-learning classification of British Columbia copper-porphyry ore and indicator minerals using micro-X-ray–fluorescence core scanners 37

X. Lu, X. Wang and G.M. Dipple: Characterizing reactivity of ultramafic minerals and tailings in British Columbia for carbon capture and storage 45

B.P. Iulianella Phillips, R.L. Simister, C.J.R. Hart and S.A. Crowe: Microbial biosensors in through-cover mineral exploration 55

S. Hendi, E. Eberhardt and M. Gorjian: Review of fibre-optic applications in the geosciences in British Columbia 63

T. Shapka-Fels: Summary of a numerical investigation of the Red Chris operations in northern British Columbia using the Finite-Discrete Element Method 71

Integrated Interpretation of Electromagnetic and Gravity Data to Resolve Deep Geology and Aid Mineral Exploration in the Quesnel Terrane, Central British Columbia (Parts of NTS 093A, B, G, H, J, K, N, O, 094C, D)

D.E. Mitchinson, Mineral Deposit Research Unit, Department of Earth and Ocean Sciences, The University of British Columbia, Vancouver, British Columbia, dmitch@eoas.ubc.ca

Mitchinson, D.E. (2023): Integrated interpretation of electromagnetic and gravity data to resolve deep geology and aid mineral exploration in the Quesnel terrane, central British Columbia (parts of NTS 093A, B, G, H, J, K, N, O, 094C, D); *in* Geoscience BC Summary of Activities 2022: Minerals, Geoscience BC, Report 2023-01, p. 1–12.

Introduction

A nearly 300 km swath of the central Quesnel terrane of British Columbia (BC) is covered by glacial till deposits (Figure 1). With limited direct access to bedrock for mapping, geology is largely inferred here. This makes it difficult to confidently link geological formations along the terrane, to unravel geological history and environments, and to fully understand the mineral potential of the region. One of the best means of mapping geology beneath this till cover is through collection and analysis of geophysical data. Previous geophysical-data interpretations for this region have relied mostly on magnetic data, which provides significant insight into bedrock lithology and structure. Magnetic surveys, however, respond only to rocks that contain magnetic minerals. Other geophysical methods may distinguish between lithological units where magnetic data cannot. Electromagnetic (VTEM) and gravity data collected for Geoscience BC's QUEST Project in 2007 have been underused to interpret geology of the Quesnel terrane beneath cover, yet show promise for distinguishing between volcanic units and identifying intrusive rocks (magnetic or nonmagnetic) and structure. This project aims to explore and define the ability of VTEM and gravity data to distinguish lithological units beneath cover in the Quesnel terrane, and to corroborate features interpreted previously from magnetic data. The project addresses two Geoscience BC Strategic Plan objectives:

- Advancing Science and Innovative Geoscience Technologies: The project will explore whether new geological information can be derived from underused electromagnetic and gravity data.
- Identifying New Natural Resource Opportunities: The project will provide further insight into geology beneath cover and, by association, mineral-deposit environments in the Quesnel terrane.

This publication is also available, free of charge, as colour digital files in Adobe Acrobat® PDF format from the Geoscience BC website: http://geosciencebc.com/updates/summary-of-activities/.

Background

Quesnel Terrane Geology and Mineral Deposits

The Quesnel terrane is a volcanic-arc terrane of the Canadian Cordillera that formed between the Late Paleozoic and the Mesozoic, amalgamating onto the western edge of the ancestral North American craton (Nelson and Colpron, 2007). The geology of the terrane is dominated by mafic volcanic, volcaniclastic and sedimentary rocks and subduction-related intrusive bodies that are found exposed all along the north-striking terrane. Volcanic flows of Eocene to Pleistocene age blanket the Mesozoic geology in parts of the belt (e.g., Chilcotin Group rocks; Mathews, 1989).

British Columbia is a significant producer of Canada's copper (Natural Resources Canada, 2021), with most of the output coming from the province's porphyry-copper deposits. Porphyry-copper and -gold mineralization in the Quesnel terrane are known to be linked to magmatic events that correlate with the late development of the terrane. Specifically, four belts of intrusive rocks associated with porphyry mineralization have been identified in the southern Quesnel terrane, ranging in age from Late Triassic to Early Jurassic (Logan and Schiarizza, 2011; Logan and Mihalynuk, 2014). Alkalic porphyry deposits, known to be associated with two of the identified magmatic belts in the Quesnel terrane, are of particular economic interest due to their elevated abundances of gold and platinum-group metals (Jensen and Barton, 2000; Thompson et al., 2001; Hanley et al., 2020). Alkalic porphyry deposits currently being mined in the Quesnel terrane include the Mount Milligan, Mount Polley, New Afton and Copper Mountain deposits. Other notable developed porphyry properties include the Lorraine and Mouse Mountain properties.

In the central Quesnel terrane, there is excellent potential for porphyry mineralization similar to known occurrences in the northern and southern parts of the terrane; however, there is limited bedrock exposure due to overlying till deposits. Much of the geological understanding of the Quesnel terrane is derived from its northern and southern extents, where there is more topographic relief, less cover

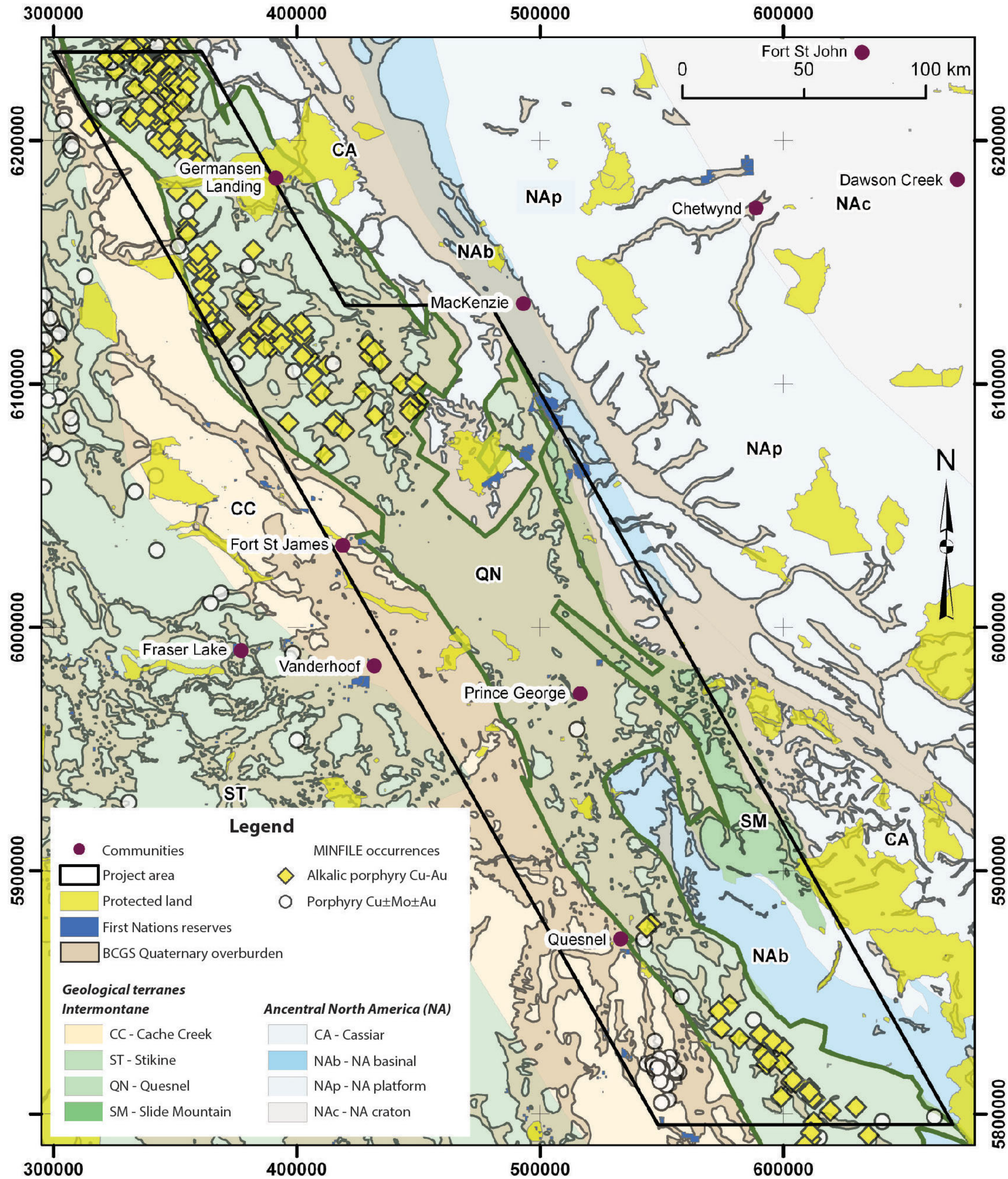

Figure 1. The study area for this project corresponds to Geoscience BC's QUEST Project study area. The light-brown region shows the distribution of Quaternary overburden mapped by the BC Geological Survey (Cui et al., 2017). Significant porphyry copper±gold±molybdenum and porphyry copper-gold occurrences are known in the northern and southern extents of the project area. Bedrock geology is largely obscured in the region around Prince George, limiting understanding of the full mineral potential of the central Quesnel terrane. Project area outlined in black. Quesnel terrane outlined in dark green. Locations of porphyry and other mineral occurrences from MINFILE BC (BC Geological Survey, 2020). Map co-ordinates in UTM Zone 10, NAD 83.

and better outcrop exposure. Recently, Quesnel terrane stratigraphy in the Bridge Lake–Quesnel River area of south-central BC was detailed by Schiarizza (2019). These detailed stratigraphic studies are used, in part, to guide understanding of geophysical patterns explored in this project.

Previous Geophysical Investigations in the Quesnel Terrane

There has been significant interest in improving knowledge of bedrock geology through the central Quesnel terrane due to its high mineral prospectivity. The best means of imaging the subsurface where there is surficial cover limiting direct geological observation is through remote sensing. Gravity and VTEM surveys over the most heavily till-covered regions of the Quesnel terrane were commissioned by Geoscience BC in 2007 (Geotech Limited, 2008; Sander Geophysics Limited, 2008), enhancing opportunities to discover new information about the subsurface of this terrane. Mira Geoscience Ltd. completed 1-D to 3-D geophysical inversions of the QUEST electromagnetic, gravity and magnetic data, and ran cluster analyses on the resulting models to identify geophysical domains.

A geological and structural interpretation for the central Quesnel terrane, using primarily magnetic data, was completed by Sánchez et al. (2015). Mitchinson et al. (2022) also evaluated Quesnel magnetic data, along with gravity and electromagnetic data, specifically to target intrusive rocks that could act as hosts to porphyry deposits in the Quesnel terrane.

Data and Methodology

Public Data Available

This study focuses on gravity and VTEM data collected as part of Geoscience BC's QUEST Project (Barnett and Kowalczyk, 2008). These data have not been widely used in interpretations of bedrock geology of the Quesnel terrane, yet geological information is represented in the data.

Gravity data were collected by Sander Geophysics (Sander Geophysics Ltd., 2008) at a survey-line spacing of 2 km. The data were inverted by Mira Geoscience (Mira Geoscience Ltd., 2009), and more recently by the University of British Columbia Geophysical Inversion Facility (UBC-GIF) as part of Geoscience BC's 'Identification of New Porphyry Potential Under Cover in British Columbia' Project (Mitchinson et al., 2022). Gravity-data maps and 3-D models of density can be used for geological interpretations (Figure 2a). Gravity 2-D–gridded data have cell sizes of 250 m^2 and inversion-model cell sizes of 500 m^2 near surface, so these data are best suited to interpreting regional trends in geology.

Electromagnetic data were collected by Geotech (Geotech Ltd., 2008). Survey lines were spaced 4 km apart, with data collected along the line every 0.1 second, which equates to a reading approximately every 2–3 m. These data were inverted by Mira Geoscience (Mira Geoscience Ltd., 2009). The inversion process involved completing 1-D inversions at each data point and then stitching the 1-D inversions together along the line to yield a pseudo–2-D inversion. With frequent along-line data, there is detailed information along a data transect and in the recovered inversion models. The 4 km distance between VTEM lines makes high resolution, between-line interpolation unreliable. However, even with the more detailed information lost, generation of isosurfaces from inversion models can still reveal broad trends in resistive and conductive domains that are useful for regional interpretation (Figure 2b).

In addition to gravity and VTEM data and models, Natural Resources Canada magnetic data (Natural Resources Canada, 2020) will be evaluated. Rock lithological, lithogeochemical and physical property data were sourced from the BC Geological Survey (BCGS; Han et al., 2016; Cui et al., 2017; BC Ministry of Energy, Mines and Low Carbon Innovation, 2020) and the Geological Survey of Canada (Enkin, 2018). Rock-type information derived from the geochemical and petrophysical databases are especially useful for linking geophysical responses to observed bedrock geology. To utilize the rock descriptions from public physical-property and geochemical datasets, which are often very detailed and/or not standardized, a simplified lithological code consistent across databases was established for broad-scale integration against the geophysical data.

Interpretation products from Barnet and Williams (2009), Fraser and Hodgkinson (2009), Mira Geoscience (2009) and Sánchez et al. (2015) will also be used in this work, to compare previous interpretations to new interpretations from VTEM and gravity data.

Methodology

Geophysical data and models were compiled in 3-D GIS platforms SKUA-GOCAD™ and Geoscience Analyst Pro. BC Geological Survey geology maps and other relevant data, including drilling, sampling and geochemical databases, that provide direct observations about bedrock geology, were imported into 3-D software for exploratory data analysis and preliminary identification of correlations between geophysical and geological data.

Initial observations indicated that VTEM inversions provide information about geological structure and texture. Guided by these observations, geological interpretations were made along each VTEM inversion line. Specifically, resistive bodies reflecting cohesive intrusions and massive volcanic deposits were digitized. Apparent faults and contacts were also identified as vertical or dipping conductors. VTEM model trends correlate extremely well with gravity-

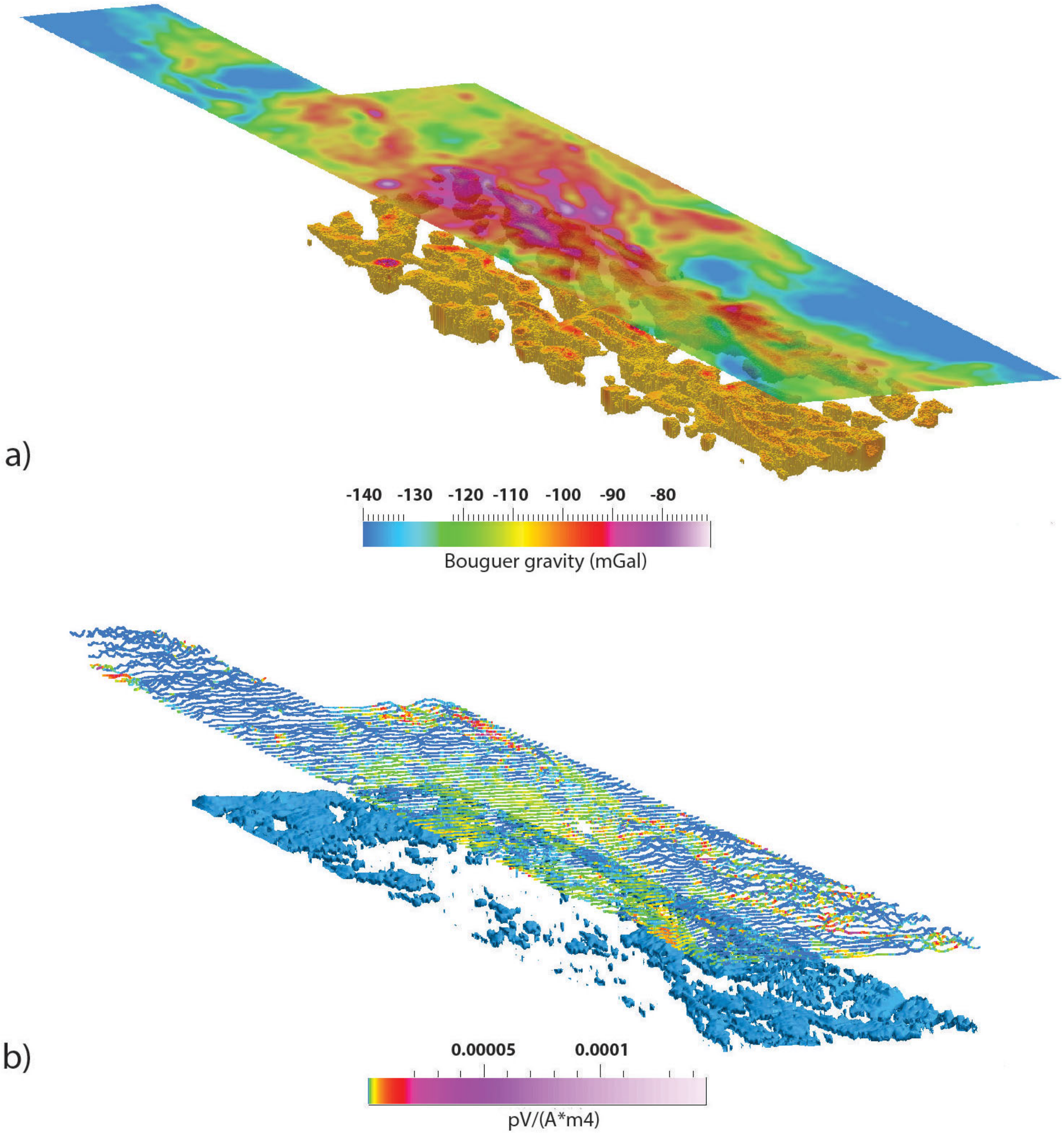

Figure 2. Gravity and electromagnetic (VTEM) data and models focused on for this project: **a)** QUEST Bouguer gravity data and density isosurface at a cut-off of 2.69 g/cm^3 from inversions completed as part of Geoscience BC's 'Identification of New Porphyry Potential Under Cover in British Columbia' Project (Mitchinson et al., 2022). **b)** Electromagnetic (VTEM) data and conductivity isosurface (emphasizing low-conductivity regions) at a cut-off of 0.06 S/m (Siemens/metre) from VTEM inversions completed by Mira Geoscience (Mira Geoscience Ltd., 2009). Abbreviations: A, Ampere(s); m, metre(s); mGal, milligal(s); ms, millisecond(s); pV, picovolt(s).

model trends, and geophysical domains based on these models will be used to update geological interpretations and/or add geophysically derived geological detail through the areas of thickest glacial cover in the central Quesnel terrane.

Preliminary Observations and Interpretations

Trends in VTEM Data and Models

Electromagnetic inversion models prove to be an excellent source of geological information. This is clear when VTEM inversion models are compared to geological maps from the BCGS (Figure 3). Some of the key geological features identified in VTEM inversion models are demonstrated in a series of sections in Figure 4.

Figure 4a shows stitched 1-D VTEM inversion models from the northern end of the QUEST Project area. At the western end of these sections, resistive regions characterize intrusive rocks of the Early Jurassic to Cretaceous Hogem Plutonic Suite, as well as a Cretaceous granodiorite (Jean Marie stock). Takla Group volcanic sedimentary rocks are variable in their conductivity, likely indicating a mix of porous and more massive volcanic stratigraphy. High resistivities characterize mapped augite-bearing basalts. Volcanic agglomerates of the Chuchi Lake succession are mostly conductive, and adjacent Nechako Plateau sedimentary rocks are strongly conductive. The eastern ends of these sections pass through geology near the Mount Milligan deposit. The large pluton north of the Mount Milligan mine is resistive.

Figure 4b shows several sections crosscutting geology at the approximate latitude of the Mount Polley mine. In the west, Chilcotin Group volcanic rocks are strongly conductive. These are known to commonly be highly vesicular (Bevier, 1983), and resulting high porosities would likely enhance conductivity. The Granite Mountain Batholith and adjacent tonalitic intrusive rocks are highly resistive. Cache Creek Complex sedimentary and volcanic rocks are variably conductive, with apparent alternating resistive and conductive stratigraphy. As in the northern sections, Triassic pyroxene basalt is resistive. At the eastern end of the sections, syenitic to monzodioritic rocks hosting the Mount Polley deposit are resistive.

Gravity and Magnetic Data Trends

The VTEM data and models appear to show close spatial correlation with gravity data (Figure 5). This correlation is seen in physical-property data trends and could be, in part, related to rock porosity (Mitchinson et al., 2021). Increased porosity reduces rock mass overall, lowering density relative to an equivalent nonporous rock. Resistivity also decreases with increased porosity. Some of the major trends in gravity and VTEM models are identified in Figure 5. An interesting trend is the spatially correlated resistivity highs and density highs that trend north to northwest through the centre of the project area ('A' labels in Figure 5). Similar correlations are found where pyroxene-bearing basaltic rocks have been mapped in the Mount Milligan and Mount Polley areas.

Massive intrusive bodies that are more felsic in nature, such as felsic intrusions, or metamorphosed felsic or sedimentary domains often exhibit high resistivities correlated with gravity lows ('B' labels in Figure 5). In these cases, the high resistivities suggest low porosities, with apparent low densities attributed to the bulk composition of the rocks, which is dominated by low-density felsic minerals such as quartz, feldspar and albite.

The third major trend between density and resistivity is correlated resistivity lows and gravity lows that are characteristic of more porous sedimentary and volcaniclastic rocks ('C' labels in Figure 5).

Magnetic response, in general, is subdued through the central Quesnel terrane. Three primary sources of magnetic anomalies are indicated in Figure 6. Magnetic volcanic stratigraphy ('a' labels in Figure 6) is found in the southern part of the project area, with more voluminous magnetite-bearing units surrounding Mount Polley. This magnetic volcanic stratigraphy extends southward into the southern Quesnel terrane, where it seems to continue along the western edge of the terrane, possibly beneath recent volcanic deposits (Thomas et al., 2011).

Magnetic highs extending through the central part of the project area are mostly related to discrete, magnetite-bearing, intermediate to ultramafic intrusive bodies ('b' labels in Figure 6; Mitchinson et al., 2022) and recent Chilcotin Group basalt deposits ('c' labels in Figure 6).

The Hogem Plutonic Suite in the northern part of the project area is largely magnetic, and the Early Jurassic phases of this suite define an anomalous trend extending south and then southeast toward the large magnetic intrusion north of the Mount Milligan deposit.

Conclusions

Summary of Geophysical Trends in the Central Quesnel Terrane

From preliminary investigations, QUEST VTEM data and models spatially correlate strongly with gravity data and models from the central Quesnel terrane, distinguishing massive volcanic and intrusive domains from more permeable and porous sedimentary-rock–dominated domains. Magnetic response is weak throughout much of the central Quesnel terrane, with the exception of magnetite-bearing intrusive bodies and occurrences of recent Chilcotin Group basalt deposits. The paucity of magnetic volcanic stratigra-

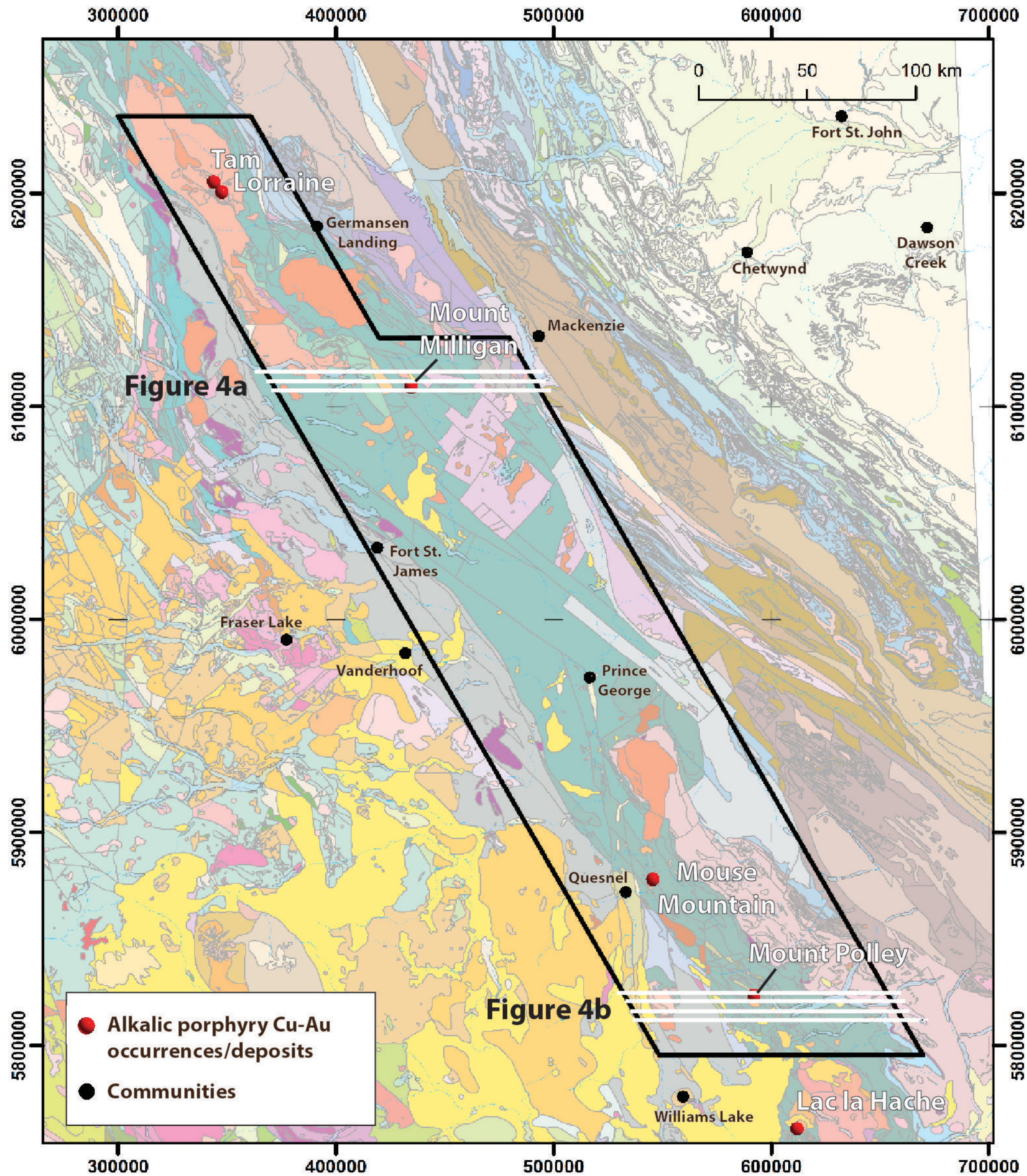

Figure 3. White traces indicate the locations of VTEM inversion models shown in Figure 4. Details are examined from two areas, one in the northern part of the project area near the Mount Milligan deposit and the other in the southern part of the area near the Mount Polley deposit. Project area outlined in black. Geology from BCGS (Cui et al., 2017). Map co-ordinates in UTM Zone 10, NAD 83.

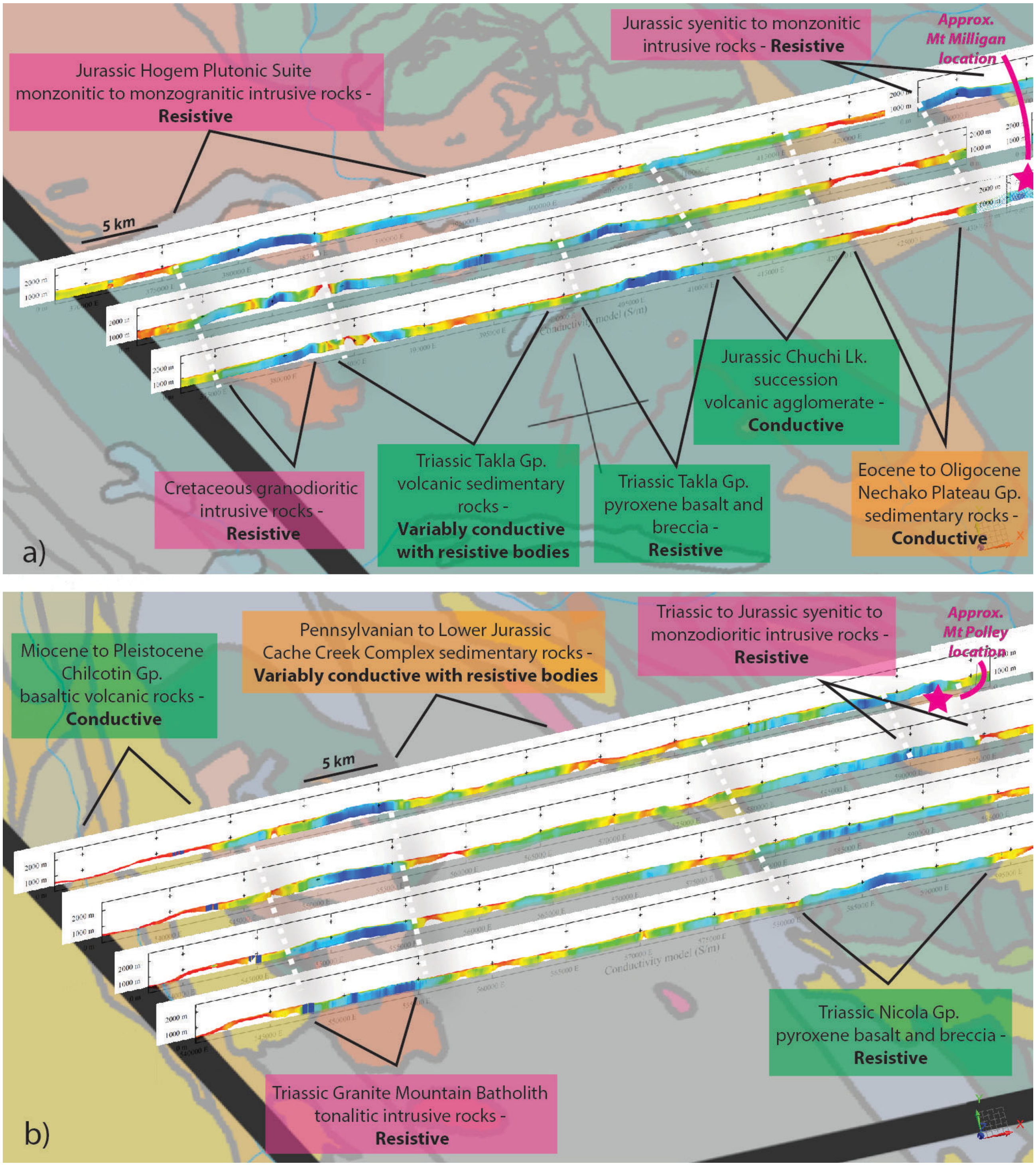

Figure 4. VTEM inversion models from Mira Geoscience (Mira Geoscience Ltd., 2009) superimposed on the BCGS bedrock geology map of BC (Cui et al., 2017): **a)** northern project area sections from Figure 3; **b)** southern project area sections from Figure 3. Inversion models show conductivity data, with red representing high-conductivity (low-resistivity) regions and blue representing low-conductivity (high-resistivity) regions. Pink text boxes highlight electromagnetic characteristics of intrusive rock units, green boxes highlight characteristics of volcanic rock units, and orange boxes highlight characteristics of sedimentary rock units.

phy through the central Quesnel terrane suggests the presence of volcanic assemblages, or volcanic deposits, that differ from the more strongly magnetic stratigraphy found surrounding, and south of, the Mount Polley mine.

Future Work and Deliverables

Available geological maps and geophysical data and models will continue to be explored to further advance hypotheses and data-relationship trends developed to this point. In addition to visual assessment and interpretations of geophysical trends, relationships between data and models will be investigated more quantitatively through application of data querying and cluster analysis of inversion models.

The key project outputs will be 2-D maps with overlain geophysical interpretations summarizing new insights gained through this integrated data analysis.

The project will be concluded in mid-2023, and project deliverables will include

- shapefiles and DXF files of interpreted geological features,
- geology map(s) with newly interpreted features,

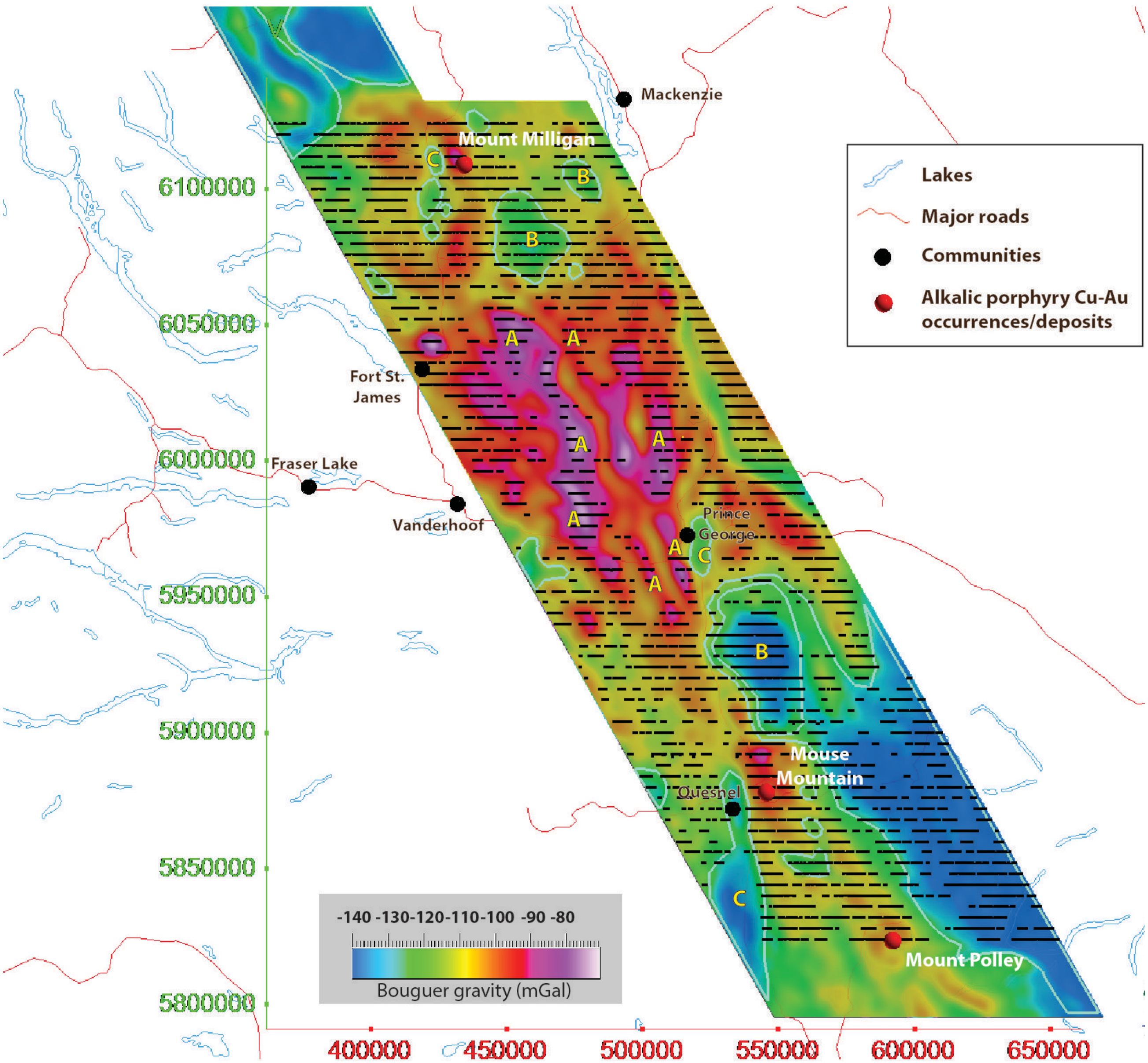

Figure 5. Correlations between resistivity domains from VTEM inversion models and gravity data. Background map is Bouguer gravity and black east-west lines indicate resistive regions along VTEM inversion sections. 'A' labels indicate regions where resistivity highs and gravity highs are co-located and are likely to represent massive, dense, volcanic deposits (low porosities and permeabilities) or ultramafic intrusive rocks. 'B' labels tag regions where resistivity highs correlate with gravity lows and represent massive felsic intrusive or massive metamorphosed bodies. 'C' labels indicate areas where resistivity lows correlate with density lows in porous sedimentary rock units. Map coordinates in UTM Zone 10, NAD 83. Abbreviation: mGal, milligal(s).

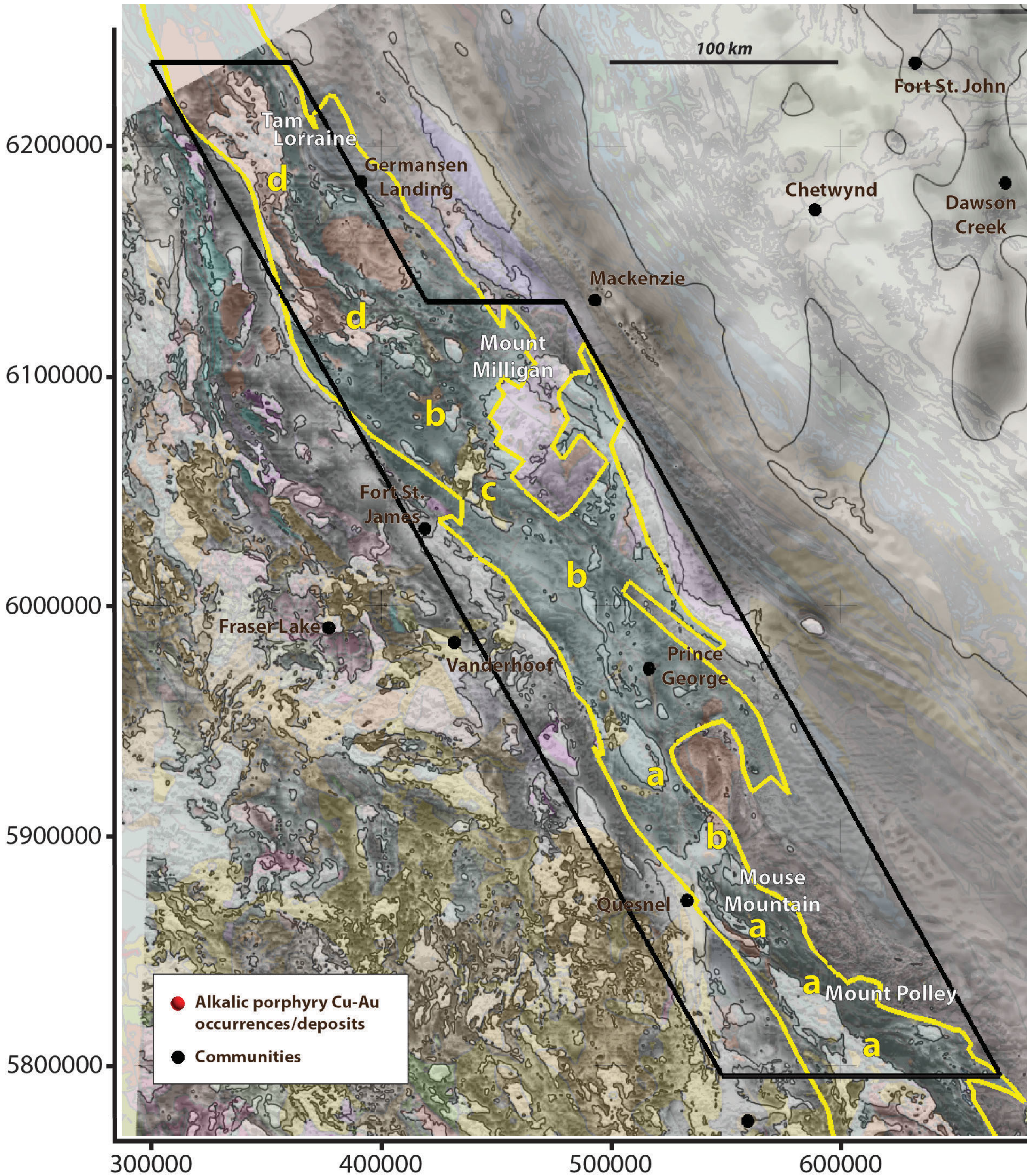

Figure 6. Natural Resources Canada magnetic data (Natural Resources Canada, 2020) in greyscale over the project area, with a contour at 0 nT (white regions are >0 nT). The figure highlights the primary magnetic features seen in the project area. The project area is outlined in black. The Quesnel terrane is outlined in yellow (Colpron and Nelson, 2011), with 'a' labels indicating magnetic volcanic stratigraphy, 'b' labels identifying several areas where magnetic anomalies are associated with discrete mapped and inferred intrusive bodies, 'c' labels indicating magnetic Chilcotin Group basalts, and 'd' labels corresponding to magnetic Hogem Plutonic Suite intrusive rocks.

- map package for ArcGIS and/or Geoscience Analyst, and
- report.

Interpretations from these largely underused geophysical datasets will provide new insights into the beneath-cover geology of the central Quesnel terrane that will be used to help understand how geology there relates to the northern and southern Quesnel terranes, and to identify potential mineral deposit environments and new exploration targets.

Acknowledgments

The author wishes to thank Geoscience BC and the Geoscience BC Minerals Technical Advisory Committee for funding this project. Many individuals, including C. Hart, D. Fournier, T. Astic and D. Cowan, have provided valuable feedback and guidance throughout earlier and current investigations of these data. The author gratefully acknowledges P. Kowalczyk and J. Logan for early reviews of this report.

References

Barnett, C.T. and Kowalczyk, P.L. (2008): Airborne electromagnetics and airborne gravity in the QUEST Project area, Williams Lake to Mackenzie, British Columbia (parts of NTS 093A, B, G, H, J, K, N, O; 094C, D); *in* Geoscience BC Summary of Activities 2007, Geoscience BC, Report 2008-1, p. 1–6, URL <http://www.geosciencebc.com/i/pdf/SummaryofActivities2007/SoA2007-Barnett.pdf> [October 2020].

Barnett, C.T. and Williams, P.M. (2009): Using geochemistry and neural networks to map geology under glacial cover; Geoscience BC, Report 2009-03, 27 p. URL <https://cdn.geosciencebc.com/project_data/QUESTdata/GBCReport2009-3/GBC_Report_2009-3.pdf> [October 2022].

Bevier, M.L. (1983): Implications of chemical and isotopic composition for petrogenesis of Chilcotin Group basalts, British Columbia; Journal of Petrology, v. 24, no. 2, p. 207–226, URL <https://doi.org/10.1093/petrology/24.2.207>.

BC Geological Survey (2020): MINFILE BC mineral deposits database; BC Ministry of Energy, Mines and Low Carbon Innovation, BC Geological Survey, URL <http://minfile.ca> [July 2019].

BC Ministry of Energy, Mines and Low Carbon Innovation (2020): Assessment Report Indexing System (ARIS); BC Ministry of Energy, Mines and Low Carbon Innovation, BC Geological Survey, URL <https://www2.gov.bc.ca/gov/content/industry/mineral-exploration-mining/british-columbia-geological-survey/assessmentreports> [May 2020].

Colpron, M. and Nelson, J.L. (2011): Yukon terranes – a digital atlas of terranes for the northern Cordillera; Yukon Geological Survey, URL <http://data.geology.gov.yk.ca/Compilation/2> [November 2020].

Cui, Y., Miller, D., Schiarizza, P. and Diakow, L.J. (2017): British Columbia digital geology; BC Ministry of Energy, Mines and Low Carbon Innovation, BC Geological Survey, Open File 2017-8, 9 p., URL <http://cmscontent.nrs.gov.bc.ca/geoscience/PublicationCatalogue/OpenFile/BCGS_OF2017-08.pdf> [June 2019].

Enkin, R.J. (2018): Canadian rock physical property database: first public release; Geological Survey of Canada, Open File 8460, 1 ZIP file, URL <https://doi.org/10.4095/313389>.

Fraser, S.J. and Hodgkinson, J.H. (2009): An investigation using SiroSOM for the analysis of QUEST stream-sediment and lake-sediment geochemical data; Geoscience BC Report 2009-14, CSIRO Report EM MDU P2009/983, 64 p., URL <https://cdn.geosciencebc.com/project_data/GBC_Report2009-14/GBC_Report_2009-14.pdf> [October 2022].

Geotech Limited (2008): Report on a helicopter-borne versatile time domain electromagnetic (VTEM) geophysical survey: QUEST project, central British Columbia (NTS 93A, B, G, H, J, K, N, O and 94C, D); Geoscience BC, Report 2008-4, 35 p., URL <http://www.geosciencebc.com/i/project_data/QUESTdata/report/7042-GeoscienceBC_final.pdf> [June 2019].

Han, T., Rukhlov, A.S., Naziri, M. and Moy, A. (2016): New British Columbia lithogeochemical database: development and preliminary data release; BC Ministry of Energy and Mines, BC Geological Survey GeoFile 2016-4, 6 p. URL <https://cmscontent.nrs.gov.bc.ca/geoscience/PublicationCatalogue/GeoFile/BCGS_GF2016-04.pdf> [August 2022].

Hanley, J., Kerr, M., LeFort, D., Warren, M., MacKenzie, M. and Sedge, C. (2020): Enrichment of platinum-group elements (PGE) in alkali porphyry Cu-Au deposits in the Canadian Cordillera: new insights from mineralogical and fluid inclusion studies; *in* Porphyry Deposits of the Northwestern Cordillera of North America: a 25 Year Update, E.R. Sharman, J.R. Lang, and J.B. Chapman (ed.), Canadian Institute of Mining, Metallurgy, and Petroleum, Special Volume 57, p. 88–109.

Jensen, E.P. and Barton, M.D. (2000): Gold deposits related to alkaline magmatism; *in* Gold in 2000, S.G. Hagemann and P.E. Brown (ed.), Society of Economic Geologists Reviews, v. 13, p. 279–314.

Logan, J.M. and Mihalynuk, M.G. (2014): Tectonic controls on Early Mesozoic paired alkaline porphyry deposit belts (Cu-Au±Ag-Pt-Pd-Mo) within the Canadian Cordillera; Economic Geology, v. 109, p. 827–858, <https://doi.org/10.2113/econgeo.109.4.827>.

Logan, J.M. and Schiarizza, P. (2011): Geology of the Quesnel and Stikine terranes and associated porphyry deposits; *in* Exploration Undercover; A Practical Example Using the QUEST Study Area, Geoscience BC Workshop, URL <http://www.geosciencebc.com/i/pdf/Presentations/UnderCoverWS2011/Talk_4_Schiarrizza.pdf> [January 2020].

Mathews, W.H. (1989): Neogene Chilcotin basalts in south central BC: geology, ages and geomorphic history; Canadian Journal of Earth Sciences, v. 26, no. 5, p. 969–982, URL <https://doi.org/10.1139/e89-078>.

Mira Geoscience Limited (2009): QUEST Project: 3D inversion modelling, integration, and visualization of airborne gravity, magnetic, and electromagnetic data, BC, Canada; Geoscience BC, Report 2009-15, 87 p., URL <http://www.geosciencebc.com/reports/gbcr-2009-15/> [November 2022].

Mitchinson, D.E., Fournier, D., Hart, C.J.R., Astic, T., Cowan, D.C. and Lee, R.G. (2022): Identification of new porphyry potential under cover in British Columbia; Geoscience BC, Report 2022-07 (and MDRU Publication 457), 97 p., URL <https://cdn.geosciencebc.com/project_data/

GBCReport2022-07/GBC2022-07%20MDRU457%20Identification%20of%20New%20Porphyry%20Potential%20Under%20Cover%20in%20British%20Columbia.pdf> [October 2022].

Mitchinson, D.E., Hart, C.J.R. and Fournier, D. (2021): Uncovering porphyry-deposit potential in the Quesnel terrane of central British Columbia using geology and 3-D geophysics (parts of NTS 093A, B, G, H, J, K, O); *in* Geoscience BC Summary of Activities 2020: Minerals, Geoscience BC, Report 2021-01, p. 11–24.

Nelson, J. and Colpron, M. (2007): Tectonics and metallogeny of the British Columbia, Yukon and Alaskan Cordillera, 1.8 Ga to the present; *in* Mineral Deposits of Canada: A Synthesis of Major Deposit-Types, District Metallogeny, the Evolution of Geological Provinces, and Exploration Methods, W.D. Goodfellow, (ed), Geological Association of Canada, Mineral Deposits Division, Special Publication 5, p. 755–791, <https://cmscontent.nrs.gov.bc.ca/geoscience/PublicationCatalogue/External/EXT060.pdf> [November 2022].

Natural Resources Canada (2020): Canadian Airborne Geophysical Data Base; Natural Resources Canada, URL <http://gdr.agg.nrcan.gc.ca/gdrdap/dap/search-eng.php> [October 2019].

Natural Resources Canada (2021): Copper facts; Natural Resources Canada, URL <https://www.nrcan.gc.ca/our-natural-resources/minerals-mining/minerals-metals-facts/copper-facts/20506> [October 2021].

Sánchez, M.G., Bissig, T. and Kowalczyk, P. (2015): Interpretation map of magnetic and gravity datasets, QUEST area, central British Columbia; Geoscience BC, Report 2015-15, scale 1:500 000, URL <http://www.geosciencebc.com/reports/gbcr-2015-15/> [May 2020].

Sander Geophysics Limited (2008): Airborne gravity survey, Quesnellia region, British Columbia; Geoscience BC, Report 2008-8, 121 p., URL <http://www.geosciencebc.com/i/project_data/QUESTdata/GBCReport2008-8/Gravity_Technical_Report.pdf> [November 2022].

Schiarizza, P. (2019): Geology of the Nicola Group in the Bridge Lake–Quesnel River area, south-central British Columbia; *in* Geological Fieldwork 2018, BC Ministry of Energy, Mines and Petroleum Resources, BC Geological Survey, Paper 2019-01, p. 15–30, URL <https://cmscontent.nrs.gov.bc.ca/geoscience/PublicationCatalogue/Paper/BCGS_P2019-01-02_Schiarizza.pdf> [September 2022].

Thomas, M.D., Pilkington, M., Anderson, R.G. and Mareschal, J-C. (2011): Geological significance of high-resolution magnetic data in the Quesnel terrane, central British Columbia; Canadian Journal of Earth Sciences, v. 48, p. 1065–1089, URL <https://doi.org/10.1139/e10-109>.

Thompson, J.F.H., Lang, J.R. and Stanley, C.R. (2001): Platinum group elements in alkaline porphyry deposits, British Columbia; *in* Exploration and Mining in British Columbia 2001, BC Ministry of Energy, Mines and Low Carbon Innovation, Mines Branch, p. 57–64.

Timing and Origin of Gold Mineralization in the Blueberry Zone of the Scottie Gold Mine Project, Stikine Terrane, Northwestern British Columbia (NTS 104D/01)

A. Hutchison[1], **Department of Geology, Saint Mary's University, Halifax, Nova Scotia and Mount Royal University, Calgary, Alberta, alex.hutchison@smu.ca**

M. Stewart, Department of Geology, Mount Royal University, Calgary, Alberta

J. Hanley, Department of Geology, Saint Mary's University, Halifax, Nova Scotia

R.C. Stewart, Serac Exploration Ltd., Vancouver, British Columbia

Hutchison, A., Stewart, M., Hanley, J. and Stewart, R.C. (2023): Timing and origin of gold mineralization in the Blueberry zone of the Scottie Gold Mine project, Stikine terrane, northwestern British Columbia (NTS 104D/01); *in* Geoscience BC Summary of Activities 2022: Minerals, Geoscience BC, Report 2023-01, p. 13–24.

Introduction

The 'Golden Triangle' is a mineral district in northwestern British Columbia (BC) that encompasses gold and porphyry-copper deposits, epithermal polymetallic deposits and volcanogenic massive-sulphide (VMS) base- and precious-metal deposits. The Golden Triangle contains the Scottie Gold Mine project, which consists of over thirty mineralized zones located within the Iskut–Stewart–Kitsault belt of the Stikine terrane. The Scottie Gold Mine project comprises three main zones across approximately 4 km: the Blueberry zone, the Scottie Gold Mine zone and the Domino zone. The mineralization trend of the Blueberry zone has a north-south orientation and is juxtaposed against the easterly trend of the Scottie Gold Mine and Domino zones. The focus of this study is to determine the timing and origin of gold mineralization in the Blueberry zone of the Scottie Gold Mine project, with the larger objective of determining the relationship between the Blueberry mineralization trend and the Scottie Gold mine mineralization trend. This will be done by combining detailed field mapping and drillcore sampling with petrography, whole-rock and mineral chemical analyses, as well as microanalytical methods (e.g., fluid-inclusion systematics), to achieve several specific outcomes:

- describe the hostrock units, alteration assemblages and ore-zone mineralogy for the Blueberry zone
- determine which minerals are typically associated with gold
- establish a paragenesis for the Blueberry zone that will be integrated with the deformation history
- compare the timing and style of gold mineralization in the Blueberry zone with those in the Scottie Gold Mine and Domino zones

This research aims to improve ore-deposit models and revise exploration criteria for epithermal-porphyry gold deposits in northwestern BC.

Background

Regional Geology

The Cordilleran orogeny resulted in terrane accretion along the western margin of the North American craton beginning in the Early to Middle Jurassic (Colpron et al., 2015). The tectonic domains of the Cordilleran Orogen are, from inboard to outboard, the Intermontane terranes, the Insular terranes, the Arctic terranes as well as the Mesozoic and younger arc and accretionary terranes (Nelson and Colpron, 2007). The terranes of the Intermontane belt were the earliest to be accreted and consist predominantly of island-arc terranes that developed in the peri-Laurentian realm (Nelson and Colpron, 2007). The Stikine terrane is one of these Intermontane island-arc terranes and preserves evidence of island-arc magmatism, sedimentation and deformation from its initial development, in the Late Devonian to Late Triassic, through to terminal collision with the North American craton (Evenchick et al., 2010; Colpron et al., 2015; Milidragovic et al., 2016). The Stikine terrane is subdivided into four stratigraphic units that are all separated by unconformities: the Devonian–Permian Stikine assemblage, the Upper Triassic Stuhini Group, the Lower to Middle Jurassic Hazelton Group and the Upper Jurassic to Lower Cretaceous Bowser Lake Group (Figure 1; Nelson et al., 2013). The Stikine terrane contains the major precious- and base-metal deposits that together define the area known as the 'Golden Triangle.' The development of the mineral deposits in the Golden Triangle was most prominent between the Late Triassic to Middle Jurassic and deposit types include Cu±Au±Mo porphyry deposits, Au-Ag epithermal deposits and VMS deposits (e.g., Barresi et al., 2015; Cutts et al., 2015). The intrusions associated with these mineral deposits can be subdivided into three groups based on their

---

[1]*The lead author is a 2022 Geoscience BC Scholarship recipient.*

This publication is also available, free of charge, as colour digital files in Adobe Acrobat® PDF format from the Geoscience BC website: http://geosciencebc.com/updates/summary-of-activities/.

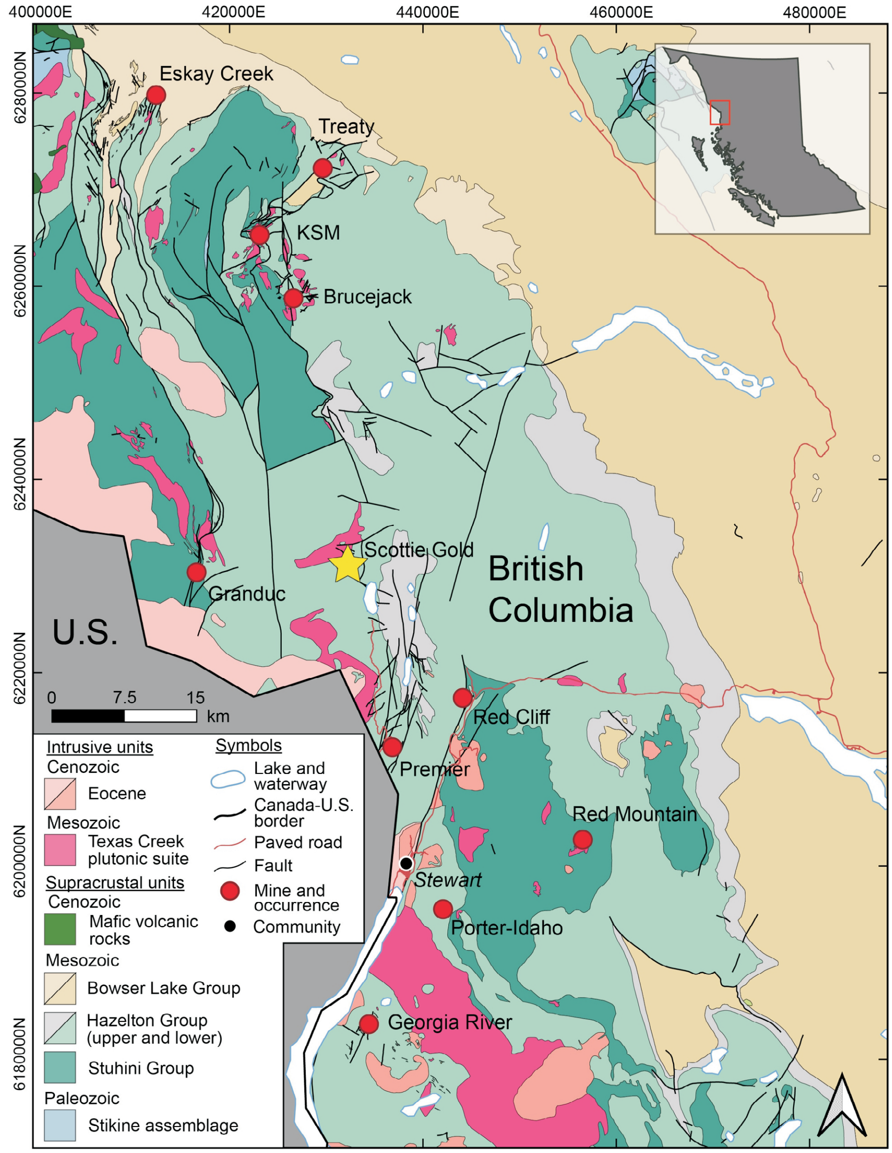

Figure 1. Regional geology of the Iskut–Stewart–Kitsault mineral belt (modified after Cui et al., 2017); the yellow star indicates the location of the Scottie Gold Mine project. All co-ordinates are in UTM Zone 9, NAD 83.

ages: late Triassic (ca. 222–210 Ma), terminal Triassic (205–201 Ma) and early Jurassic (197–190 Ma; Barresi et al., 2015). The Stuhini and Hazelton groups are associated both spatially and temporally with these mineralizing intrusions (Barresi et al., 2015).

The Hazelton Group is one of the major mineralization-hosting sequences within the Golden Triangle and comprises the study area (Figure 1). It unconformably overlies the Upper Triassic Stuhini Group, which consists of submarine mafic to intermediate volcanic rocks and epiclastic rocks, including shale, siltstone and limestone units; it is itself unconformably overlain by the sedimentary rocks of the Upper Jurassic to Lower Cretaceous Bowser Lake Group (Nelson and Kyba, 2014; Nelson et al., 2018). The Hazelton Group hosts substantial amounts of metallic ore (Au, Ag, Cu) and is comagmatic and coeval with several plutonic suites, including the latest Triassic Tatogga suite and the Early Jurassic Texas Creek and Brucejack Lake suites (Evenchick et al., 2010; Voordouw and Branson, 2021; Nelson et al., 2022). The Hazelton Group is subdivided into upper and lower sequences, and the units within each of these sequences vary from north to south (Nelson et al., 2018). In the Unuk River–lower Iskut River–Stewart area, the lower Hazelton Group consists of the basal siliciclastic Jack Formation and the Snippaker unit, as well as the Betty Creek Formation (Nelson et al., 2018). The Betty Creek Formation is predominantly andesite with lesser occurrences of felsic pyroclastic rocks and their epiclastic products; it also contains the Unuk River andesite unit, the Johnny Mountain dacite unit and the Brucejack

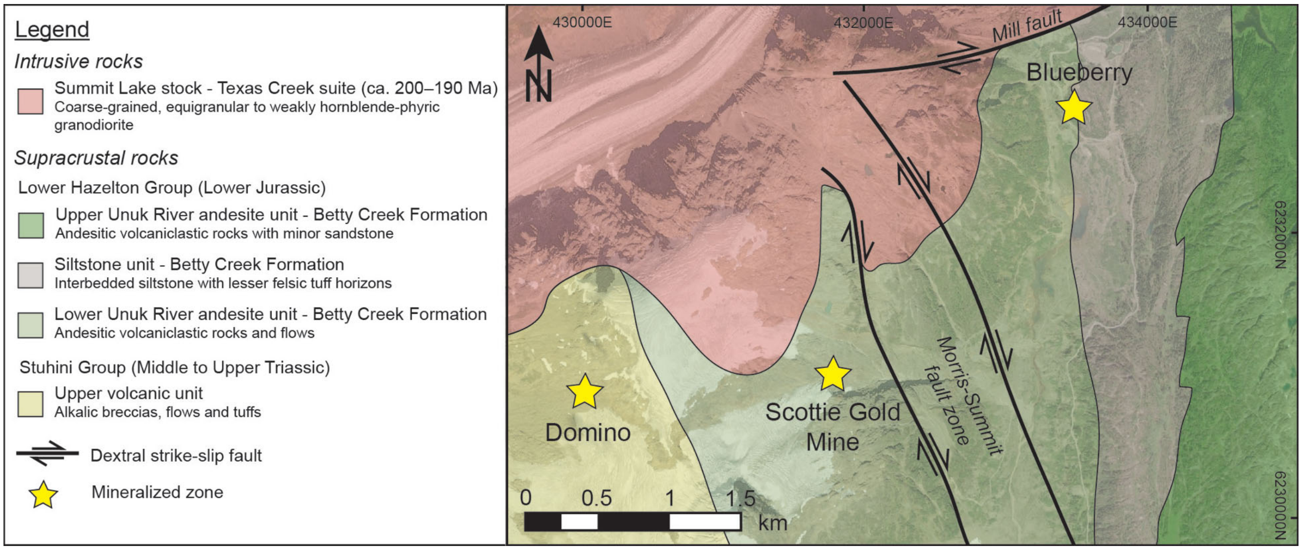

Figure 2. Geology of the Scottie Gold Mine project area. All co-ordinates are in UTM Zone 9, NAD 83.

Lake felsic unit (Nelson et al., 2018). The Unuk River andesite unit has been dated at ca. 197 Ma using U-Pb zircon geochronology (Nelson et al., 2018). In the study area, the upper Hazelton Group contains the Spatsizi, Quock and Mount Dilworth formations (Nelson et al., 2018).

Deposit Geology

The Scottie Gold Mine project is located approximately 30–35 km north of Stewart, BC, and comprises the Blueberry, Scottie Gold Mine and Domino zones (Figure 2). The Scottie Gold Mine project area is underlain by rocks of the Stuhini and Hazelton groups and intruded by Early Jurassic Texas Creek plutons (Figure 1; Stanley et al., 2022). The hostrocks to the Domino zone are alkalic volcanic flows, breccia and tuff of the Stuhini Group (Stanley et al., 2022); the hostrocks to the Scottie Gold Mine zone are volcaniclastic rocks and flows of the lower Unuk River andesite, which belongs to the Betty Creek Formation (Figure 2; Stanley et al., 2022). The Blueberry zone is interpreted to be located at the contact between the lower Unuk River andesite and the siltstone unit, which also belongs to the Betty Creek Formation (Figure 2; Stanley et al., 2022). This siltstone unit will herein be referred to as the 'Betty Creek siltstone unit'. The contact between the lower Unuk River andesite and the Betty Creek siltstone unit defines a steeply dipping, northerly mineralization trend, whereas mineralization at the Domino and Scottie Gold Mine zones defines an easterly trend (Voordouw and Branson, 2021). The contact at the Blueberry zone exhibits strong and pervasive chlorite-pyrite-carbonate alteration and this alteration zone is approximately 15 to 30 m thick (Voordouw and Branson, 2021). Drilling and surficial mapping support the presence of east-northeast-striking mineralized-vein structures that intersect the Blueberry zone contact and may be indicative of high-grade gold mineralization. The highest concentrations of gold mineralization have been documented along north-plunging ore shoots that occur at the intersection between the contact and these crosscutting veins (e.g., Blueberry vein; Voordouw and Branson, 2021). The Blueberry zone is also separated from the Scottie Gold Mine and Domino zones by the Morris-Summit fault zone (Figure 2; Stanley et al., 2022); however, the relationship between this fault zone and mineralization is currently unknown.

Methodology

During the 2021 field season, three 2020 drillholes were relogged and mapping of the surficial materials was completed at the Blueberry zone, with the goal of documenting changes in lithology, alteration and mineralization (including hydrothermal vein types). Samples were initially selected to ensure representative coverage of all vein and alteration styles. Using available assay data, additional samples were selected using the following criteria: zones with high sulphide content and high gold concentrations, zones with high sulphide content and low gold concentrations, and zones with low sulphide content and high gold concentrations. These additional samples were collected to examine the relationship between gold and sulphide mineralization, and to determine why gold concentrations do not always correlate with sulphide zones. Two of three drillholes were selected from the northern half of the property (SR20–48 and SR20–55; Mumford, 2021) and the third drillhole was selected from the southern half of the property (SR20–45; Mumford, 2021). Drillcore samples, outcrop samples and pulps were sent to ALS-Geochemistry (Terrace, BC) for processing and analysis to evaluate Au, Ag, Co, Cu, Pb and Zn tenors, but also to generate a geochemical database for study purposes. Pulp samples are previously sampled, pulverized and assayed core samples for which a new aliquot was re-assayed. Drillcore and outcrop samples underwent the following sample-preparation and analytical procedures:

- determination of Au by fire assay of 30 g samples (for low-range determination between 0.005 to 10 ppm)
- determination of Au by fire assay, with gravimetric finish of 30 g samples (for high-range determination between 0.05 to 10 000 ppm)
- four-acid digestion, with inductively coupled plasma–mass spectrometry (ICP-MS) finish of 0.25 g samples
- four-acid digestion, with overlimit methods using 0.4 g samples (ALS, 2022).

Pulps underwent the following procedures:

- determination of Au by fire assay of 30 g sample, with a range between 0.005 and 10 ppm
- four-acid digestion, with ICP-MS finish of 0.25 g sample (ALS, 2022).

Thirty-six thin sections were produced at Vancouver Petrographics Ltd. (Vancouver, BC) from core (23 sections) and outcrop (13 sections) samples for petrographic work and to facilitate ongoing microanalysis at Saint Mary's University in Halifax, Nova Scotia. Transmitted- and reflected-light microscopy, scanning electron microscopy (SEM) and micro-X-ray–fluorescence (μXRF) spectrometry enabled detailed petrography and semiquantitative chemical analysis of minerals. Transmitted- and reflected-light microscopy was performed using an Olympus BX51 microscope at Saint Mary's University; photomicrographs were taken using a microscope-mounted, high-resolution digital camera.

Scanning Electron Microscope (SEM)

Backscattered-electron (BSE) imaging and semiquantitative energy-dispersive–X-ray spectroscopy (EDS) analysis of sulphides, silicates and other associated accessory phases (including gold carriers) were performed at Saint Mary's University using a TESCAN MIRA3 LMU field emission–scanning electron microscope (FE-SEM) equipped with a X-Max 80 mm^2 large area silicon drift detector (SDD) energy-dispersive–X-ray spectrometer manufactured by Oxford Instrument. The electron-beam spot size was ~10 nm in diameter and the accelerating voltage used was 20 kV, together with a beam current of ~0.3 nA. The INCA software published by ETAS was used for data reduction and EDS-spectrum acquisition. This technique was used on thin sections created from both field and core samples to better understand general mineralogy as well as the timing of gold mineralization within the overall mineral-assemblage paragenesis.

Micro-X-Ray Fluorescence

False-colour element-abundance maps were produced using a Bruker M4 Tornado Plus μXRF spectrometer at Saint Mary's University to map major-, minor- and trace-element distribution on the surface of thin-section offcuts. Analyses were conducted under vacuum using a Rh X-ray source operated at an accelerating voltage of 50 kV and beam current of 600 μA, focused to a 20 μm diameter excitation spot size. Data was processed using software developed for the Bruker M4 Tornado scanner. The detector throughput was 275 000 cps and calibration was carried out on Zr. Pixels in element-abundance maps are spaced at 40 to 80 μm and the count time per pixel was 30 ms.

Results

Surficial Mapping

Surficial mapping at the Blueberry zone during the 2021 field season improved spatial definition of the contact between the lower Unuk River andesite unit to the west and the Betty Creek siltstone unit to the east; the results of this mapping exercise are summarized in Figure 3. Within the map area, the lower Unuk River andesite unit is characterized by medium green-grey andesitic tuff with ash- to lapilli-sized grains. The Betty Creek siltstone unit is dominantly dark green, fine grained and bedded, but along-strike lithofacies variations are observed. In the northernmost section of the map area, this unit is dominated by argillite, which is very fine grained, dark grey to black and overprinted by intense silicification. In the southern portion of the map area, the siltstone is interbedded with cream-coloured felsic pyroclastic beds. The contact between the andesite and the siltstone appears to be gradational; however, it is completely overprinted by alteration. The zone of intense alteration along the contact has been broken out as a separate unit on the map because it obscures the exact location and nature of the contact (Figures 3, 4a–c). Figure 4a shows an outcrop from the northern extent of the map area; where the contact zone is crosscut by a medium green-grey, altered and weakly mineralized porphyritic lamprophyre dike with euhedral hornblende laths. An example of a southern outcrop and hand sample within the contact zone is shown in Figure 4b and c, respectively. The contact zone is also crosscut at a high angle by several interpreted faults. These faults are not exposed at surface, but the units are clearly offset and the faults have been intersected in drillcore.

Alteration

Alteration at the Blueberry zone is localized at the contact between the lower Unuk River andesite unit and the Betty Creek siltstone unit. The alteration is most intense at the contact and decreases in intensity moving outward from the contact zone. The alteration styles observed within the contact zone are the following:

- weak to moderate carbonate and silica alteration with a patchy to pervasive distribution (Figure 5a)

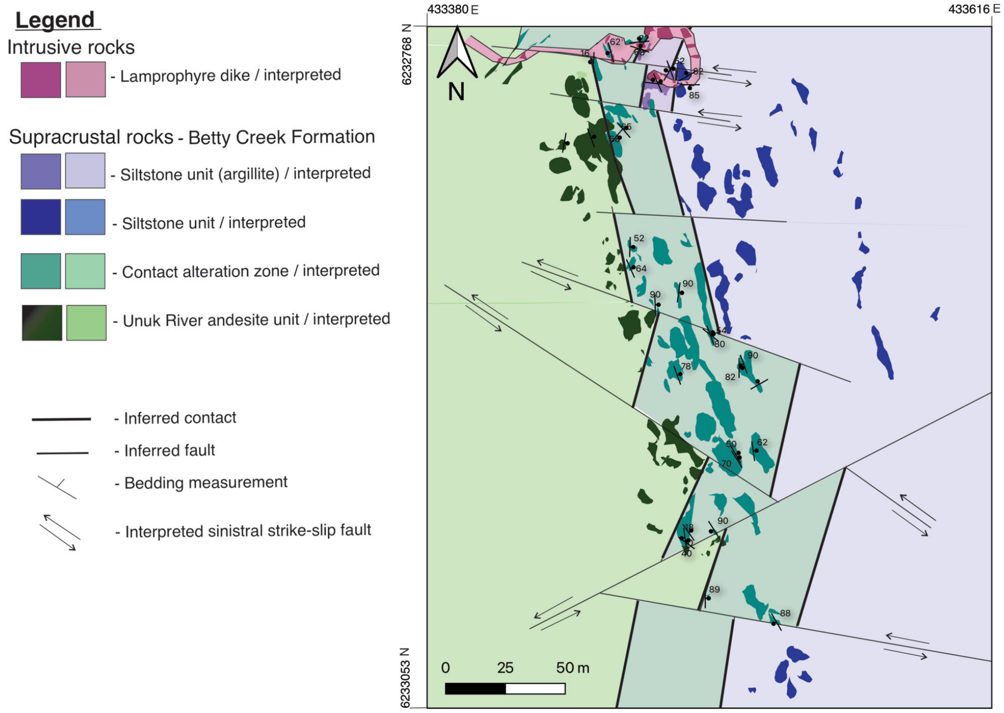

Figure 3. Geology of the Blueberry zone of the Scottie Gold Mine project. All co-ordinates are in UTM Zone 9, NAD 83.

- weak to moderate chlorite alteration that is dominantly patchy (Figure 5b), but also locally occurs as pervasive or fracture-controlled alteration, as vein selvages or along bedding planes
- moderate to strong sericite alteration that is typically patchy and less frequently pervasive (Figure 5a–c)
- weak epidote alteration that is patchy (Figure 5c) or within vein selvages

Sericite alteration is typically most closely associated with sulphide mineralization; however, this is a preliminary observation and the relative timing of the various alteration styles and their relationship to sulphide and gold mineralization are currently under investigation.

Sulphide Mineralization

Sulphide mineralization in the Blueberry zone occurs both within the zone of intense alteration along the andesite–siltstone contact (the 'contact zone'; Figure 3) and along a series of faults that crosscut the contact at a high angle. These mineralization styles are described below.

Contact Zone

Mineralization in the contact zone is disseminated, within veins and along vein selvages. Based on fieldwork, drill-core observations and transmitted- and reflected-light microscopy, the dominant base-metal sulphide minerals present within the contact zone are, in descending order of abundance, pyrrhotite, pyrite, sphalerite, chalcopyrite, arsenopyrite, galena and molybdenite. The average modal sulphide abundance across the entire contact zone is approximately 2–4 vol %; however, mineralized veins contain 10–50 vol % sulphides. Pyrrhotite and pyrite (with lesser chalcopyrite) occur disseminated within the groundmass, within massive sulphide veins (~1–3 cm wide), along the margins of quartz-carbonate veins, along bedding planes and within pyrite-dominated stringers. Pyrrhotite is the most abundant sulphide mineral and is present as anhedral masses that tend to be mottled, often surrounding other sulphide minerals (pyrite, chalcopyrite, arsenopyrite; Figure 6a–c). Pyrite is present as subhedral to euhedral crystals (<0.5–6 mm) in two forms: mottled (Figure 6a–c) and inclusion-free. Chalcopyrite is spatially associated with pyrite but is less abundant. It occurs as anhedral patches and is often disseminated around pyrite crystals or within fractures cutting pyrite crystals (Figure 6b). Where arsenopyrite is present, it tends to be concentrated in patches of euhedral to subhedral crystals up to ~3 mm wide (Figure 6a, c) and, like pyrite, it occurs as mottled and inclusion-free varieties. Inclusion-free arsenopyrite defines a linear fabric within the groundmass, separate from other sulphide minerals (Figure 6a), whereas mottled arsenopyrite is typically surrounded by pyrrhotite. The two arsenopyrite varieties also vary chemically, with inclusion-free arsenopyrite being enriched in both Sb and Co, whereas mottled arsenopyrite is enriched only in Co (1.37–3.53 wt % Sb and 2.99–3.69 wt % Co, and 4.89–29.15 wt % Co, respectively, in mottled arsenopyrite). Sphalerite is most commonly present within extensional quartz-

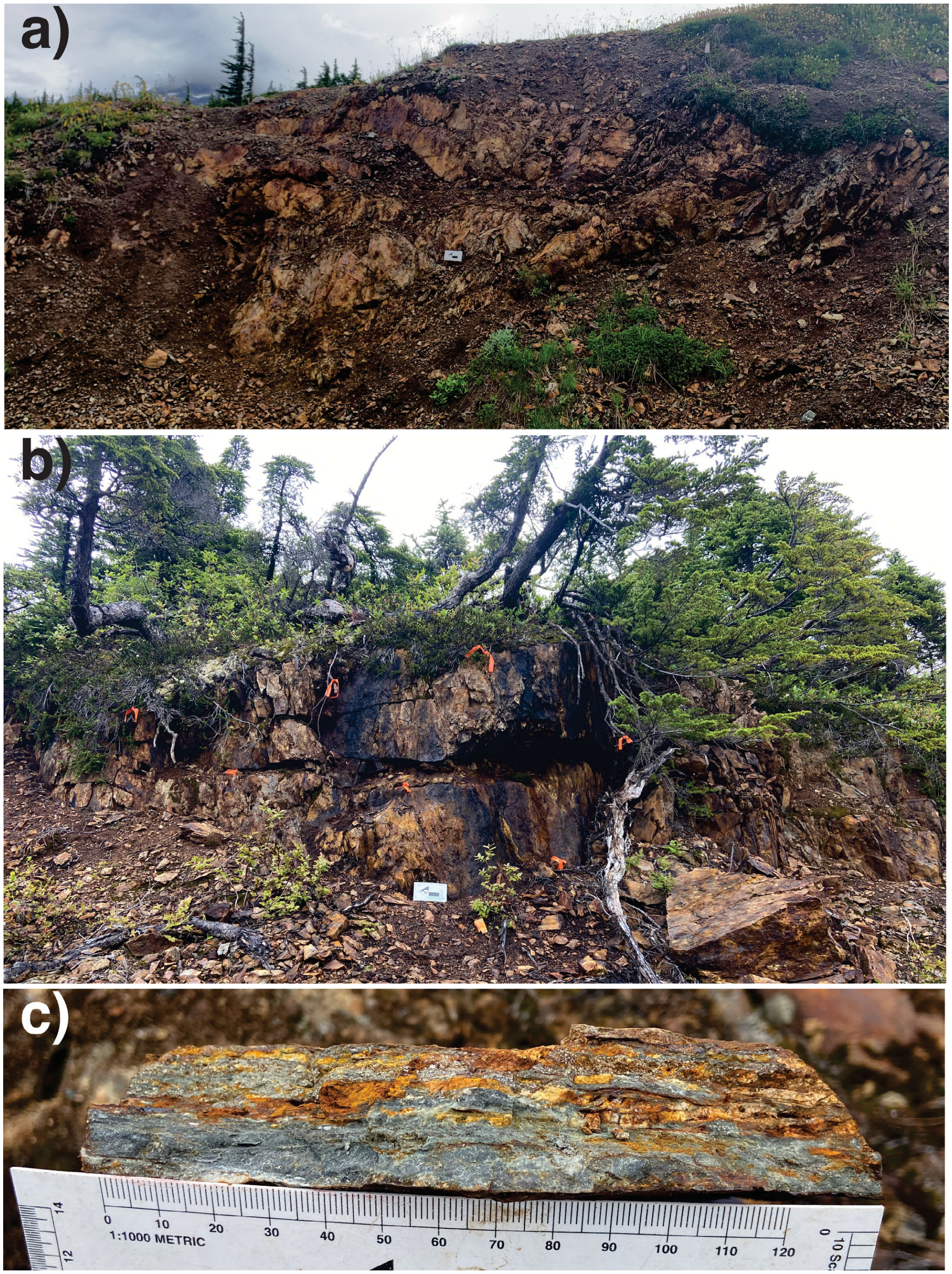

Figure 4. Field photographs showing outcrops within the gossanous central alteration zone of the Blueberry zone: **a)** northern outcrop; **b)** southern outcrop; **c)** hand sample from southern outcrop (12 cm scale card used for reference).

carbonate veins and larger extensional quartz-carbonate veins (<1–3 cm wide) also contain trace amounts of galena and molybdenite. Sphalerite occurs as inclusions within pyrrhotite and filling fractures within Co-rich arsenopyrite. Molybdenite typically occurs as isolated subhedral crystals ranging from 10 to 40 μm in width and its relationship to other sulphide minerals is unclear. The exception is galena that often occurs as inclusions within molybdenite. It appears that sulphides are less abundant extending into the sedimentary side of the contact relative to the andesite side, but mineralization is uniformly distributed within the main alteration zone. Arsenopyrite is an exception and tends to be concentrated dominantly in the southern half of the Blueberry zone.

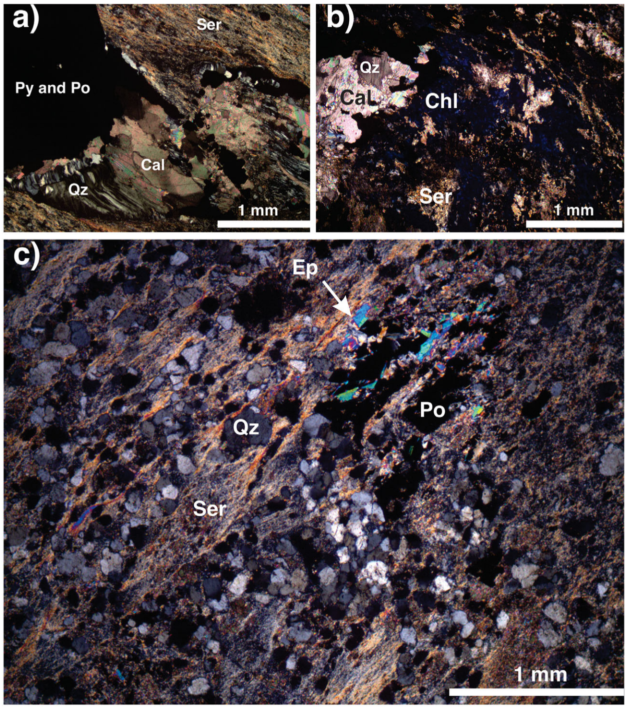

Figure 5. Photomicrographs taken in cross-polarized light of the dominant alteration minerals at the contact zone between the lower Unuk River andesite unit and the Betty Creek siltstone unit: **a)** patchy calcite (Cal) and kink-banded quartz (Qz) spatially associated with sulphide minerals and presence of very fine-grained sericite (Ser) in the groundmass; **b)** patchy carbonate and quartz crystals within a groundmass of fine- to very fine-grained chlorite (Chl) and sericite; **c)** rounded, subhedral quartz crystals crosscut by very fine-grained sericite and patchy, medium-grained epidote (Ep) crystals spatially associated with pyrrhotite (Po). Abbreviation: Py, pyrite.

Both mineralized and barren veins are observed within the contact zone and these veins can be classified into four main types:

- quartz-dominated veins consisting of fine- to medium-grained intergrown quartz crystals
- type-1 calcite-dominated veins consisting of fine- to very fine-grained calcite and defined by the absence of sulphide minerals
- type-2 calcite-dominated veins consisting of very fine-grained calcite and defined by the presence of sulphide minerals along the centre axes of the veins, with alteration minerals like epidote and accessory minerals like apatite
- extensional quartz-calcite veins containing some sulphides

The dominant sulphides in type-2 calcite veins are pyrrhotite and pyrite, and the average modal abundance of sulphides in these veins is ~30–50%. The dominant sulphides in the extensional veins are sphalerite, molybdenite and galena, and the modal abundance of sulphides in these veins is ~10–15%.

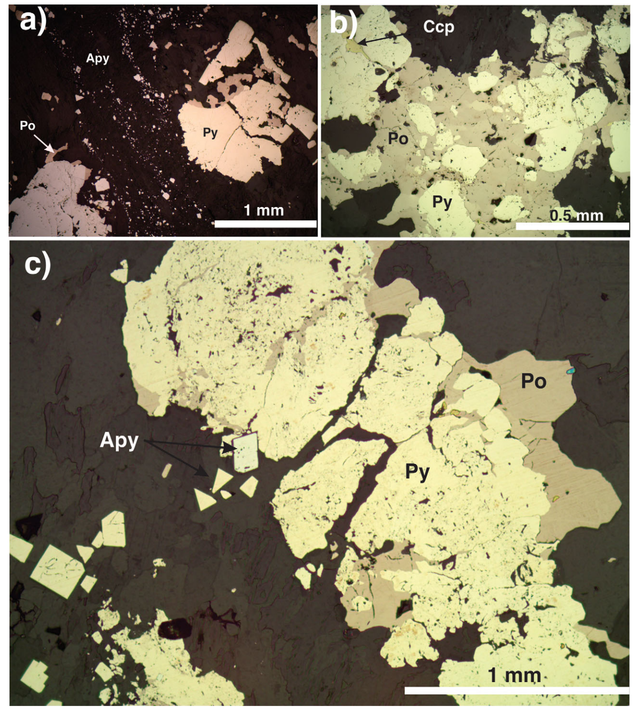

Figure 6. Sulphide-mineral relationships of the Blueberry zone shown in reflected light: **a)** mottled pyrite (Py) surrounded by pyrrhotite (Po), with euhedral to subhedral arsenopyrite (Apy) crystals defining a linear fabric; **b)** mottled pyrite surrounded by chalcopyrite (Ccp) and pyrrhotite; **c)** mottled pyrite surrounded by pyrrhotite, with an early arsenopyrite crystal near the centre.

Mineralized Crosscutting Structures

Several faults are interpreted as crosscutting the contact zone at a high angle (Figure 3) and drill results to date indicate that at least three of these structures host mineralization, which ranges from disseminated to semi-massive, with pyrrhotite, pyrite and sphalerite as the dominant sulphide minerals. These structures are interpreted to be significant for the distribution and localization of mineralization along the contact zone. However, additional work is required to correlate the surface trace of the faults with the mineralized structures intersected in drillcore and to determine the relationship between mineralization in the contact zone and the crosscutting faults. Additional drillcore samples were collected from these structures in 2022 and analyses of these samples are currently underway.

Gold Occurrences

The highest gold concentrations returned during the 2020 drilling program were intersected within the altered contact zone of the northernmost drillholes of the Blueberry Zone (SR20–48 and SR20–55). The highest gold-bearing intervals in SR20–48 are at downhole depths of 18.07–19.08 m (82.1 g/t) and 68.62–70.35 m (69.8 g/t; Mumford, 2021). The highest gold-bearing interval in SR20-55 is at a downhole depth of 78.97–79.75 m (47.9 g/t; Mumford, 2020). In both intervals, gold is spatially associated with sulphide minerals, including pyrite, arsenopyrite, pyrrhotite and molybdenite. Where it is associated with pyrite, gold occurs as 5–10 μm diameter inclusions (Figure 7a, b) within euhedral to subhedral mottled pyrite crystals. Gold associated with arsenopyrite also occurs as inclusions; arsenopyrite crystals containing gold are typically subhedral, mottled and Co-rich (Figure 7c). Where gold occurs with molybdenite, they exhibit a close spatial relationship, with observed intergrowth textures between gold and molybdenite (Figure 7d).

Discussion

A preliminary paragenesis for alteration, veining and associated mineralization on a time scale spanning magmatic to late magmatic-hydrothermal events is being developed.

Mineralization

Key textures constrain overall sulphide-mineral paragenesis. Pyrite, pyrrhotite (Figure 7a–c) and chalcopyrite (Figure 6b) tend to be spatially associated with one another, therefore broadly coeval. As stated earlier, pyrite is present as subhedral to euhedral crystals in two forms: mottled and inclusion free. Dissolution and reprecipitation of pyrite likely resulted in the mottled appearance, but later conditions allowed pyrite to grow and maintain a subhedral shape. This indicates potentially two generations of pyrite, whereby the mottled form (Figure 7b) is an earlier generation in comparison to the inclusion-free form (Figure 7a). Pyrite grains range from <0.5 to 2 mm in width. Textural relationships between the mottled-type pyrite, pyrrhotite, chalcopyrite and mottled arsenopyrite are shown in Figures 6b (chalcopyrite) and 7a–c. This pyrite likely precipitated first in the sulphide-mineral sequence, whereas chalcopyrite and, later, pyrrhotite infilled the space around the earlier subhedral pyrite owing to the general subhedral to euhedral nature of pyrite. Chalcopyrite is less abundant relative to pyrite; it forms as anhedral patches and is often disseminated in available space near pyrite crystals. Like pyrite, arsenopyrite is also present in two forms: mottled and inclusion free. Unmottled or inclusion-free arsenopyrite is euhedral and occurs as lineations away from other sulphide minerals within groundmass. The timing relationship between the linear wash of unmottled arsenopyrite (Figure 6a) in relation to pyrrhotite and pyrite in these images is not evident, though the single mottled crystal slightly to the left of centre in Figure 6c appears to be early in relation to pyrite and pyrrhotite. The unmottled arsenopyrite tends to

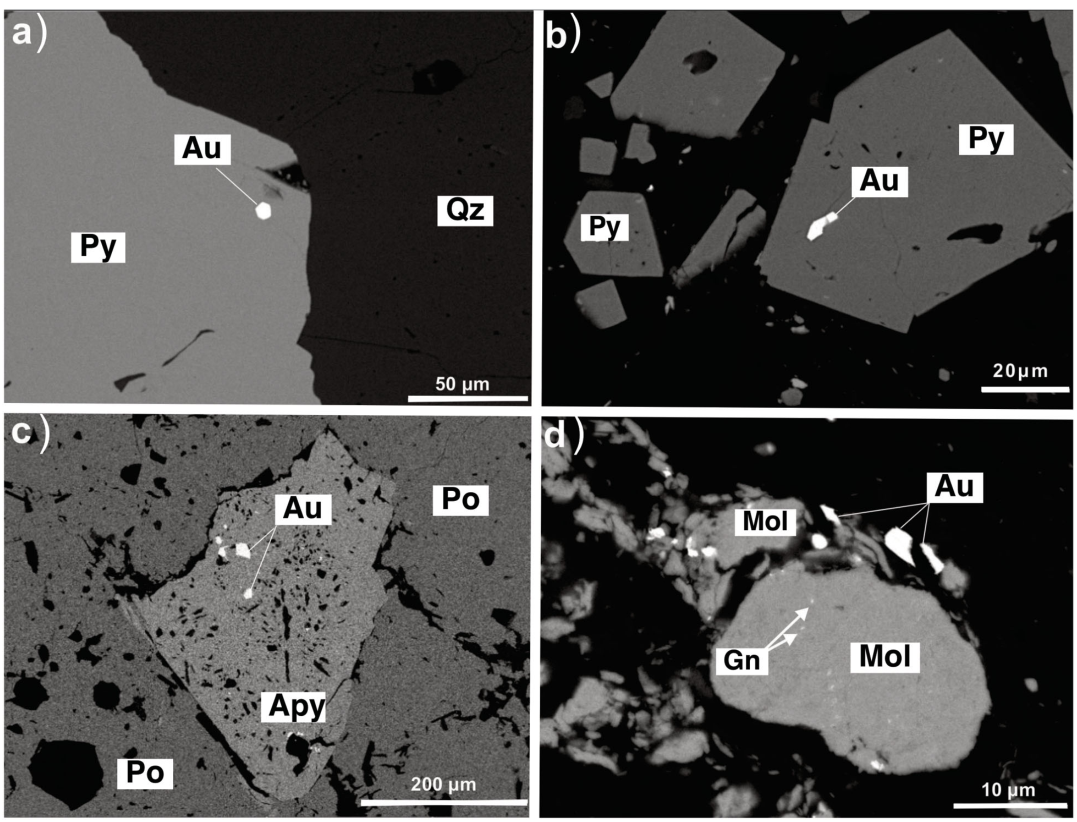

Figure 7. Backscattered-electron images of gold mineralization and associated sulphide minerals in the Blueberry zone: **a)** gold (Au) grain within an inclusion-free pyrite (Py) crystal; **b)** euhedral to subhedral pyrite crystals with some mottling and gold occupying an open space in a pyrite crystal; **c)** heavily mottled Co-rich arsenopyrite (Apy) crystal surrounded by mottled pyrrhotite (Po) and gold occupying open spaces in the arsenopyrite crystal; **d)** small gold grains (<1–3 μm) spatially associated with larger (up to 20 μm) crystals of molybdenite (Mol), as well as flecks of galena (Gn) visible within the molybdenite crystals. Abbreviation: Qz, quartz.

be a combination of both the Sb- and Co-enriched varieties. Mottled arsenopyrite is enriched only in Co and surrounded by pyrrhotite, although the open spaces of Co-enriched arsenopyrite contain gold inclusions (Figure 7c). Pyrrhotite is most abundant relative to the other sulphide minerals and is present as anhedral crystals. It is commonly found surrounding other sulphide minerals (pyrite, chalcopyrite and arsenopyrite), indicating late precipitation relative to the other sulphides.

Sphalerite inclusions occur in pyrrhotite, indicating that it postdates the precipitation of pyrrhotite; also, sphalerite commonly infills cracks in Co-rich arsenopyrite associated with pyrrhotite (not shown here). Galena is included within molybdenite, therefore likely coprecipitating with it (Figure 7d). Lastly, whereas intergrowths of gold and molybdenite are indicative of coprecipitation, no other obvious crosscutting relationships with other sulphides are observed for molybdenite.

Alteration

With respect to alteration, petrographic work suggests epidote alteration, carbonatization, silicification and chloritization all occurred during the magmatic stage. In addition to quartz associated with veining at the contact alteration zone, there is evidence of silica flooding throughout the groundmass, which is crosscut by later chlorite alteration. There is also evidence of chlorite crosscut by silica, indicating that silica may have been precipitated broadly coevally with chlorite in the groundmass. Sericite is introduced coevally with chlorite and toward the latter end of silica precipitation. Figure 5c shows coarse epidote crystals (relative to sericite grain size in the groundmass) precipitated near sulphide minerals (e.g., pyrrhotite). The subhedral shape of the pyrrhotite crystals sharing crystal boundaries with epidote suggests that epidote and pyrrhotite precipitated at a similar time. Sericite may have also been broadly coeval to late in terms of pyrrhotite precipitation, as crystal boundaries appear to be torn off the crystal in places but also growing together in others. Sericite and epidote appear to most commonly coprecipitate with sulphide mineralization. Sericitization occurs late in the system (magmatic to late magmatic/hydrothermal stage) and, in terms of alteration minerals, occurs nearest in time to the late precipitation of sulphide minerals. Sericite appears to overprint all other alteration minerals but indicates coeval precipitation with pyrrhotite. The exact relationship is unclear.

Vein and Structural Styles

It is important to constrain the relationship between the crosscutting structures and the contact zone. In particular, if the abundance of sulphides, sulphide mineralogy and associated gold content vary along the contact zone, understanding the role that crosscutting veins played in the development of these variations in the Blueberry zone would be beneficial to the deposit model. It would be useful to understand which structures transported the mineralizing fluid(s) and the timing of these events relative to one another; this information could then be paired with the microscopic evidence of these veining events (in addition to macroscopic evidence). In further developing the time scale described above, the following veining events are recognized:

- early quartz-dominated veining associated with the magmatic stage, consisting of fine- to medium-grained intergrown quartz crystals
- type-1 calcite-dominated veins, defined by a lack of sulphide minerals and the presence of fine- to very fine-grained calcite, that crosscut and, therefore, postdate the early quartz veins but are also still considered to be within the magmatic stage
- type-2 calcite-dominated veins containing sulphide minerals and considered to be associated with the transition from the magmatic to later magmatic-hydrothermal stage as there is a sulphide component, as well as alteration minerals like epidote and apatite (type-2 calcite veins)

Gold Occurrences

Along the mineralized contact zone, gold is associated with pyrite, pyrrhotite, arsenopyrite and molybdenite. Pyrite, pyrrhotite and arsenopyrite typically exhibit a close spatial relationship (occasionally with sphalerite) in the presence of gold, whereas sphalerite, galena and molybdenite commonly occur together within extensional, gold-bearing quartz-carbonate veins. This indicates that gold occurs in two distinct textural settings (and, therefore, distinct timings): disseminated with pyrite, pyrrhotite and arsenopyrite in veins and groundmass; and with disseminated and patchy sphalerite and molybdenite in quartz-carbonate veins. These two textural relationships involving gold may indicate changing conditions within a single hydrothermal mineralizing event (e.g., fluid temperature, pH, gold complexing) or that more than one gold-mineralizing event occurred. Gold was deposited during a magmatic-hydrothermal mineralizing event and later remobilized. The timing of gold mineralization in relation to other sulphide minerals is complex. Gold occurs within the open space of euhedral to subhedral pyrite crystals, indicating possible late precipitation of gold relative to pyrite. Additionally, gold is intergrown with subhedral to anhedral pyrite crystals, suggesting that it is coeval with this type of pyrite. This could mean the timing of pyrite and gold formation could be close and/or overlap. Pyrrhotite is present following the precipitation of arsenopyrite, but the timing between pyrrhotite and gold precipitation is unknown. The mottled texture of the pyrrhotite could be a result of alteration (Figures 6b, c, 7c).

Molybdenite and Arsenopyrite

Molybdenum mineralization along the western margin of the Stikine terrane precipitated during two distinct time periods: in the Lower Jurassic (Febbo et al., 2015), hosted within Au-Cu-Ag-Mo porphyry deposits associated with the Texas Creek plutonic suite; and in the early Eocene to Oligocene (Nelson and Colpron, 2007), hosted within Cu-Au-Mo– and Mo–porphyry deposits associated with intrusions of the mid-Cretaceous to mid-Eocene Coast Plutonic Complex or with small, Oligocene granitic intrusions. Given these disparate ages and a lack of textural clarity as to which generation of gold comes first in the overall deposit paragenesis, it is unclear whether gold associated with molybdenite represents early- or late-stage mineralization. This will be resolved through Re-Os radiometric dating of molybdenite. Additionally, gold is observed in open-space fillings associated with arsenopyrite crystals (Figure 7c), suggesting that gold precipitation postdates Co-rich arsenopyrite. A Re-Os age for arsenopyrite would thus provide a maximum age for gold precipitation. Given that gold may postdate arsenopyrite and be coeval with molybdenite, combined Re-Os radiometric dating of molybdenite and arsenopyrite together could tightly constrain the age of gold mineralization.

Co-Rich Arsenopyrite Versus Sb-Rich Arsenopyrite

Understanding the genetic relationship between gold and the different forms of arsenopyrite (i.e., Co- and Sb-rich) is potentially important to understanding the nature of gold mineralization at the Blueberry zone. Although Co- and Sb-enriched arsenopyrite occur together, they also occur isolated from one another. Notably, where Sb is present in arsenopyrite, gold is not. However, Co-enriched arsenopyrite also occurs with Sb-enriched arsenopyrite, both in the unmottled, euhedral form and with crystals showing alignment within the groundmass. In contrast, the mottled, subhedral Co-rich form of arsenopyrite contains gold in open-space fillings. Observations support that gold precipitation may have been more favourable under Sb-absent conditions, or when conditions were not suitable for Sb precipitation in pyrite.

Summary and Conclusions

The Blueberry zone is one of three main zones within the Scottie Gold Mine project. Locally, the host lithological units are the lower Unuk River andesite unit in the west and the Betty Creek siltstone unit in the east; the host units are separated by a north-trending contact. Based on field and drillcore observations, the contact between the two units appears to be gradational. Whether this is the case, or that the contact has been obscured by alteration and/or faulting remains unresolved. It is likely that this central alteration zone acted as a conduit for mineralizing fluids. In addition to mineralization at the contact, mineralization in the Blueberry zone also occurs along faults that cut the contact at a high angle. The relationship between mineralization in the contact zone and in the crosscutting faults is unclear and should be resolved. Samples were collected from outcrop and drillcore (from both the contact zone and the crosscutting structures) to petrographically characterize hostrock lithology, the main alteration and vein styles, and the nature of gold mineralization, as well as to provide additional samples for assay. All work completed to date has been related to the contact zone and future work will incorporate data from the mineralized crosscutting structures, enabling a detailed description of mineralization at the Blueberry zone to be constructed.

In conclusion, the dominant alteration styles identified in the contact zone are predominantly weak to moderate carbonate alteration and silicification, weak to moderate chlorite alteration distributed in a variety of ways (patchy, disseminated, fracture-controlled, within vein selvages and along bedding planes), moderate to strong sericitization and weak epidote alteration. The sulphide minerals at the contact zone are, in order of decreasing abundance, pyrrhotite, pyrite, sphalerite, chalcopyrite, arsenopyrite, galena and molybdenite. Both Co-rich and Sb-rich arsenopyrite have been observed in samples from the contact zone and gold exhibits a stronger relationship with Co-rich arsenopyrite than Sb-rich arsenopyrite. Gold likely precipitated in the late stages of the system given the nature of gold as inclusions in the open spaces of arsenopyrite and pyrite. A key aspect of the mineralization to consider is whether gold has been remobilized or not, which will require further study.

Future Work

Additional samples were collected in 2022 along the mineralized structures that crosscut the contact zone. These samples will be used to investigate the influence of these structures on gold mineralization in the Blueberry zone. Gold concentrations vary significantly along the contact zone and it is important to understand if and how the crosscutting structures influence these variations in gold mineralization. Additionally, by gaining an understanding of the nature of each vein, it may be possible to identify the timing of the mineralizing fluid as well as the conduit(s) the fluids may have used. Given that magmatic to late magmatic-hydrothermal sulphide-rich calcite veining has been observed on a microscopic scale, a comparative study to see if these microscopic veining events coincide with the larger scale features responsible for gold mineralization would be useful. During a visit to the field in 2022, additional drillcore samples were also collected for fluid-inclusion work. Work planned for the remainder of this study includes

- detailed petrography of samples from the mineralized crosscutting structures to characterize the alteration and mineralization for comparison with those in the contact zone;

- Re-Os radiometric dating of molybdenite and arsenopyrite associated with gold to determine the timing of gold mineralization;
- fluid-inclusion analysis of quartz from mineralized veins to characterize the mineralizing fluid(s); and
- laser-ablation inductively coupled plasma–mass spectrometry on individual pyrite grains to be used as a proxy for the chemical evolution of mineralization in the Blueberry zone.

The results of this detailed study on the Blueberry zone will be compared with the results of a parallel study on the Scottie Gold Mine zone to determine if these two zones belong to the same ore system and, if so, how the zones are related.

Acknowledgments

Funding for this project is provided by Scottie Resources Corp., Serac Exploration Ltd., Geoscience BC and the Natural Sciences and Engineering Research Council of Canada (NSERC) through the iMAGE-CREATE project. The authors particularly thank D. Guestrin of Serac Exploration Ltd. for his thoughtful and insightful comments, which greatly contributed to improving the manuscript.

References

ALS (2022): Geochemistry, 2022 schedule of services and fees; ALS, 50 p., URL <https://www.alsglobal.com/en/geochemistry/geochemistry-fee-schedules> [October 2022].

Barresi, T., Nelson, J.L., Dostal, J. and Friedman, R. (2015): Evolution of the Hazelton arc near Terrace, British Columbia: stratigraphic, geochronological, and geochemical constraints on a Late Triassic–Early Jurassic arc and Cu–Au porphyry belt; Canadian Journal of Earth Sciences, v. 52, no. 7, p. 466–494, URL <https://doi.org/10.1139/cjes-2014-0155>.

Colpron, M., Crowley, J.L., Gehrels, G., Long, D.G.F., Murphy, D.C., Beranek, L. and Bickerton, L. (2015): Birth of the northern Cordilleran orogen, as recorded by detrital zircons in Jurassic synorogenic strata and regional exhumation in Yukon; Lithosphere, v. 7, no. 5, p. 541–562, URL <https://doi.org/10.1130/L451.1>.

Cui, Y., Miller, D., Schiarizza, P. and Diakow, L.G. (2017): British Columbia digital geology; BC Ministry of Energy, Mines and Low Carbon Innovation, BC Geological Survey, Open File 2017-8, 9 p., URL <https://cmscontent.nrs.gov.bc.ca/geoscience/publicationcatalogue/OpenFile/BCGS_OF2017-08.pdf> [November 2022].

Cutts, J.A., McNicoll, V.J., Zagorevski, A., Anderson, R.G. and Martin, K. (2015): U-Pb geochronology of the Hazelton Group in the McTagg anticlinorium, Iskut River area, northwestern British Columbia; *in* Geological Fieldwork 2014, BC Ministry of Energy, Mines and Low Carbon Innovation, BC Geological Survey, Paper 2015-1, p. 87–101, URL <https://cmscontent.nrs.gov.bc.ca/geoscience/publicationcatalogue/Paper/BCGS_P2015-01-05_Cutts.pdf> [November 2022].

Evenchick, C.A., Poulton, T.P. and McNicoll, V.J. (2010): Nature and significance of the diachronous contact between the Hazelton and Bowser Lake groups (Jurassic), north-central British Columbia; Bulletin of Canadian Petroleum Geology, v. 58, no. 3, p. 235–267, URL <https://doi.org/10.2113/gscpgbull.58.3.235>.

Febbo, G.E., Kennedy, L.A., Savell, M., Creaser, R.A. and Friedman, R.M. (2015): Geology of the Mitchell Au-Cu-Ag-Mo porphyry deposit, northwestern British Columbia, Canada; *in* Geological Fieldwork 2014, BC Ministry of Energy, Mines and Low Carbon Innovation, BC Geological Survey Paper 2015-1, p. 59–86, URL <https://cmscontent.nrs.gov.bc.ca/geoscience/PublicationCatalogue/Paper/BCGS_P2015-01-04_Febbo.pdf> [November 2022].

Milidragovic, D., Chapman, J.B., Bichlmaier, S., Canil, D. and Zagorevski, A. (2016): H_2O-driven generation of picritic melts in the Middle to Late Triassic Stuhini arc of the Stikine terrane, British Columbia, Canada; Earth and Planetary Science Letters, v. 454, p. 65–77, URL <https://doi.org/10.1016/j.epsl.2016.08.034>.

Mumford, T. (2020): Scottie Resources discovers new mineralization trend at Blueberry Zone, reports intercepts of 22.3 g/t over 6.1 m and 8.96 g/t over 13.7 m; Scottie Resources Corp., URL <https://scottieresources.com/news/2020/thefirstresultsfromblueberry/> [November 2022].

Mumford, T. (2021): Scottie discovers new mineralization trend at Blueberry Zone, reports intercepts of 10.2 g/t gold over 3.21 m and 1.31 g/t over 22.13 m; Scottie Resources Corp., URL <https://scottieresources.com/news/2021/scottie-discovers-new-mineralization-trend-at-blueberry-zone-reports-intercepts-of-10.2-g-t-gold-over-3.21-m-and-1.31-g-t-gold/> [November 2022].

Nelson, J. and Colpron, M. (2007): Tectonics and metallogeny of the British Columbia, Yukon and Alaskan Cordillera, 1.8 Ga to the present; *in* Mineral Deposits of Canada: a Synthesis of Major Deposit Types, District Metallogeny, the Evolution of Geological Provinces, and Exploration Methods, W.D. Goodfellow (ed.), Geological Association of Canada, Mineral Deposits Division, Special Publication, no. 5, p. 755–791.

Nelson, J.A.L. and Kyba, J. (2014): Structural and stratigraphic control of porphyry and related mineralization in the Treaty Glacier–KSM–Brucejack–Stewart trend of western Stikinia; *in* Geological Fieldwork 2013, BC Ministry of Energy, Mines and Low Carbon Innovation, BC Geological Survey Paper 2014-1, p. 111–140, URL <https://cmscontent.nrs.gov.bc.ca/geoscience/publicationcatalogue/Paper/BCGS_P2014-01-07_Nelson.pdf> [November 2022].

Nelson, J.A.L., Colpron, M. and Israel, S. (2013): The Cordillera of British Columbia, Yukon, and Alaska; *in* Tectonics, Metallogeny, and Discovery: the North American Cordillera and Similar Accretionary Settings, L. Colpron, T. Bissig, B.G. Rusk and J.F.H. Thompson (ed.), Society of Economic Geologists, Special Publications, v. 17, p. 53–109, URL <https://doi.org/10.5382/sp.17.03>.

Nelson, J.A.L., van Straaten, B. and Friedman, R. (2022): Latest Triassic–early Jurassic Stikine–Yukon-Tanana terrane collision and the onset of accretion in the Canadian Cordillera: insights from Hazelton Group detrital zircon provenance and arc–back-arc configuration; Geosphere, v. 18, no. 2, p. 670–696, URL <https://doi.org/10.1130/ges02444.1>.

Nelson, J., Waldron, J., van Straaten, B., Zagorevski, A. and Rees, C. (2018): Revised stratigraphy of the Hazelton Group in the

Iskut River region, northwestern British Columbia; *in* Geological Fieldwork 2017, BC Ministry of Energy, Mines and Low Carbon Innovation, BC Geological Survey Paper 2018-1, p. 15–38, URL <https://cmscontent.nrs.gov.bc.ca/geoscience/PublicationCatalogue/Paper/BCGS_P2018-01-02_Nelson.pdf> [November 2022].

Stanley, B., Nelson, J.L. and Friedman, R. (2022): LA-ICP-MS U-Pb data files, detrital zircon geochronology, and geochemistry of the Stuhini and Hazelton groups, Scottie gold mine area, northwestern British Columbia; BC Ministry of Energy, Mines and Low Carbon Innovation, BC Geological Survey GeoFile 2022-08, 5 p., URL <https://cmscontent.nrs.gov.bc.ca/geoscience/PublicationCatalogue/GeoFile/BCGS_GF2022-08.pdf> [November 2022].

Voordouw, R. and Branson, T. (2021): Technical report on the Scottie Gold Mine Property, British Columbia, Canada; National Instrument 43-101 report prepared for Scottie Resources Corporation, 77 p., URL <https://scottieresources.com/site/assets/files/3826/scot_ni43-101report_20210507.pdf> [November 2022].

Insights from Syn- to Postmineralization Dikes into the Origin of the Brucejack High-Grade Gold-Silver Epithermal Deposit, Northwestern British Columbia (NTS 104B)

K.M.H. Ng[1], Department of Earth and Planetary Sciences, McGill University, Montréal, Quebec, man.h.ng@mail.mcgill.ca

A.E. Williams-Jones, Department of Earth and Planetary Sciences, McGill University, Montréal, Quebec

D.F. McLeish, Department of Earth and Planetary Sciences, McGill University, Montréal, Quebec

J.R. Clark, Department of Earth and Planetary Sciences, McGill University, Montréal, Quebec

S. Wafforn, Newcrest Mining Limited, Vancouver, British Columbia

Ng, K.M.H., Williams-Jones, A.E., McLeish, D.F., Clark, J.R. and Wafforn, S. (2023): Insights from syn- to postmineralization dikes into the origin of the Brucejack high-grade gold-silver epithermal deposit, northwestern British Columbia (NTS 104B); *in* Geoscience BC Summary of Activities 2022: Minerals, Geoscience BC, Report 2023-01, p. 25–36.

Introduction

Precious- and base-metal mineralization in low- and intermediate-sulphidation epithermal systems is commonly distal to igneous intrusions. For example, auriferous fluids in low-sulphidation systems may be transported along basin-bounding structures that are kilometres long (Sillitoe and Hedenquist, 2005). Nonetheless, magmas are believed to be the thermal drivers of large-scale hydrothermal systems, as well as the principal contributors of precious metals to the epithermal realm (Gammons and Williams-Jones, 1997; Heinrich et al., 2004). At the Brucejack epithermal Au-Ag deposit in the Golden Triangle of northwestern British Columbia (BC), the absence of a recognized source intrusion for the auriferous vein system poses a challenge to constraining the timing and origin of the mineralization. However, dikes that cut the volcanic and volcaniclastic rocks that host the ore are common and believed to be syn- to postmineralization. In this paper, a summary of the geochemical characteristics of these dikes is presented to gain insight into the magmatic evolution of the potential source of the bonanza-grade gold mineralization.

The Brucejack deposit, which is situated in the Sulphurets mineral district (Figure 1a, b), is characterized by high-grade gold mineralization in carbonate-quartz veins and has a mineral resource, including measured, indicated and inferred categories, of 303.3 t (10.7 million oz.) of gold and 1771.8 t (62.5 million oz.) of silver (Tetra Tech, 2020); locally, gold grades reach 41 000 g/t in 0.5 m drillcore intervals (Board et al., 2020). This hyperenrichment of the gold has been attributed to colloidal transportation and deposition (McLeish et al., 2021). Several important genetic questions, however, remain unanswered, including the source of the gold.

In many epithermal systems, the highest gold and silver concentrations occur in veins and breccias that are interpreted to form as a result of the mixing of hot, low-salinity magmatic fluids, including condensed or contracted vapours, with cooler, meteoric water (Williams-Jones and Heinrich, 2005; Tosdal et al., 2009). In some cases, spatial and temporal associations with intrusive centres and associated porphyry deposits have been recognized (Hayba et al., 1985; Arribas et al., 1995; Hedenquist, 1995), which suggests late-stage magmatic fluids played a role in the formation of epithermal mineralization (Heinrich et al., 2004). Despite the lack of a recognized source intrusion at the Brucejack deposit, syn- to postmineralization dikes are evidence of at least a spatial association between the mineralization and magmatism. The dikes intrude most major hydrothermal domains in the deposit, including both mineralized and barren stockworks (Board et al, 2020). Locally, they cut early bonanza-grade quartz-carbonate veins but are generally cut by mineralized carbonate veins (McLeish, 2022); typically, however, the dikes are unmineralized. They are metre-wide, intermediate to mafic in composition and have trace– and rare-earth–element compositions similar to those of the host volcanic rocks (e.g., volcaniclastic andesite; Tombe, 2015) and therefore, likely share a similar magmatic origin. As the closest expression of magmatism that may be genetically linked to gold, these dikes provide an opportunity to target and fingerprint the potential source of fluids and mineralization at Brucejack.

A detailed petrographic and geochemical study of a suite of intermediate to mafic dikes that have a close spatial and

[1]*The lead author is a 2022 Geoscience BC Scholarship recipient.*

This publication is also available, free of charge, as colour digital files in Adobe Acrobat® PDF format from the Geoscience BC website: http://geosciencebc.com/updates/summary-of-activities/.

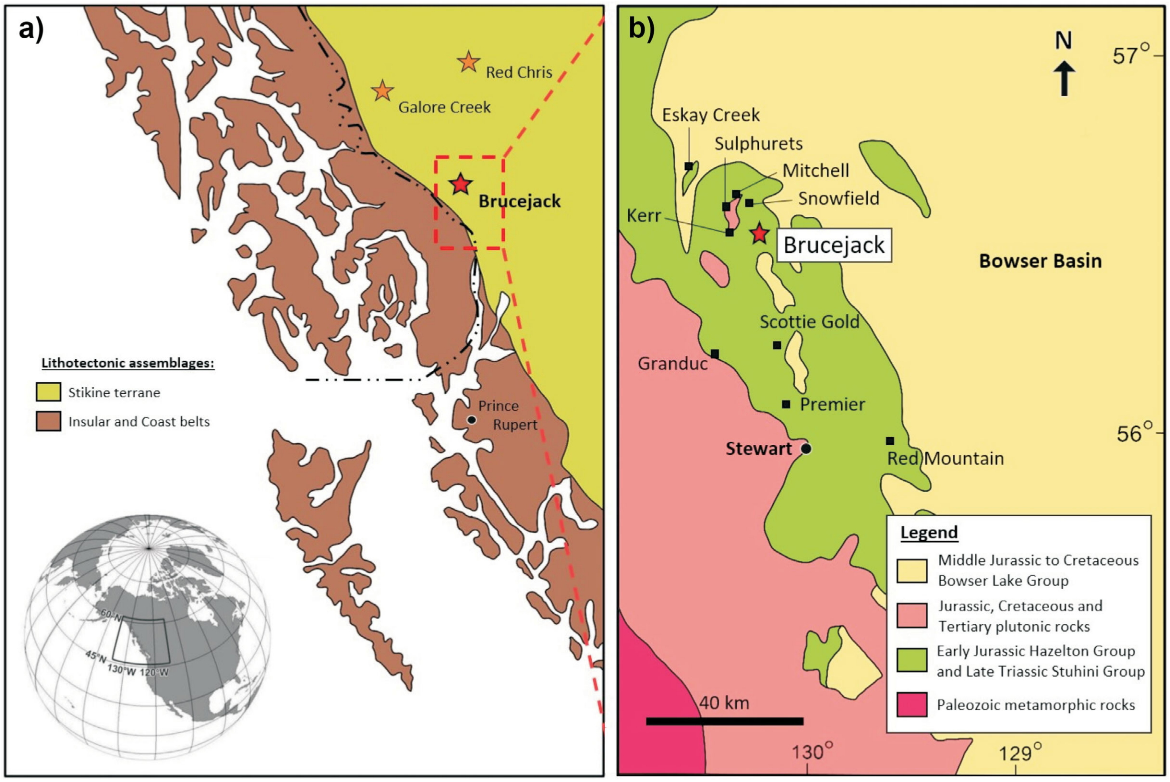

Figure 1. a) Regional geological setting of the Sulphurets mineral district in western Stikinia (modified from McLeish, 2013, with lithotectonic boundaries from Johnston, 2008). **b)** Select epithermal, volcanogenic massive-sulphide and porphyry-related deposits in the Brucejack mine area (modified from McLeish et al., 2018).

temporal association with the deposit was undertaken; the dikes are exposed in the mine and have been intersected in drillholes at depths >1 km beneath the main ore zones (Figure 2a, b).

Methods of Investigation

To better understand the spatial links between gold mineralization and syn-, late- and postmineralization dikes, a detailed review of the nature and distribution of dikes in the mapped and modelled vein corridors, including those within the Valley of the Kings mine area as well as in near-mine exploration areas (e.g., the West and Gossan Hill zones; Figure 2a, b), was conducted. Drillcore intervals of representative dike intersections from the deep-drilling program were sampled for whole-rock lithogeochemical analysis and compositional comparison with dikes in the current mine workings.

Core samples from the deep drillholes were collected at 0.5 to 1.5 m intervals and analyzed at ALS-Geochemistry (Vancouver, BC) for gold, as well as for major- and selected minor- and trace-element contents, using analytical packages ME-ICP61 and Au-AA26 (ALS, 2022). Pulp duplicates of 356 samples from the deep drillholes, including all major dikes and other intrusive units (Figure 2a, b), were analyzed for a wider spectrum of trace elements (including the rare-earth elements [REEs], Nb and Th) using analytical package ME-MS81d™ (ALS, 2022). In addition to the deep-drillhole samples, 24 dike samples sourced from within, or from drillholes immediately adjacent to, the Valley of the Kings and historic West zone mine workings were also sampled and analyzed at ALS-Geochemistry for major- and selected minor- and trace-element contents using analytical packages ME-XRF26, ME-MS81™, ME-MS61™ and F-ele82™ (ALS, 2022). All samples were subjected to lithium-borate fusion followed by digestion with a multi-acid solution, including hydrofluoric acid, to ensure near-complete extraction of the elements. All the data were processed and interpreted using the ioGAS™ software distributed by REFLEX.

Geological Setting, Mine Geology and Mineralization

Gold mineralization at the Brucejack deposit is hosted in the Early Jurassic Hazelton Group, comprising complexly deformed island-arc volcanic and volcano-sedimentary rocks of the Stikine terrane (Stikinia); the gold occurs in east- to east-northeast-trending ca.183 Ma epithermal veins (Board et al., 2020). The deposit is located along the Eskay Creek–Stewart trend of the Golden Triangle, together with Late Triassic and Early Jurassic subalkalic to alkalic porphyry and VMS deposits (Nelson et al., 2018), including Red Chris, Galore Creek, Kerr-Sulphurets-

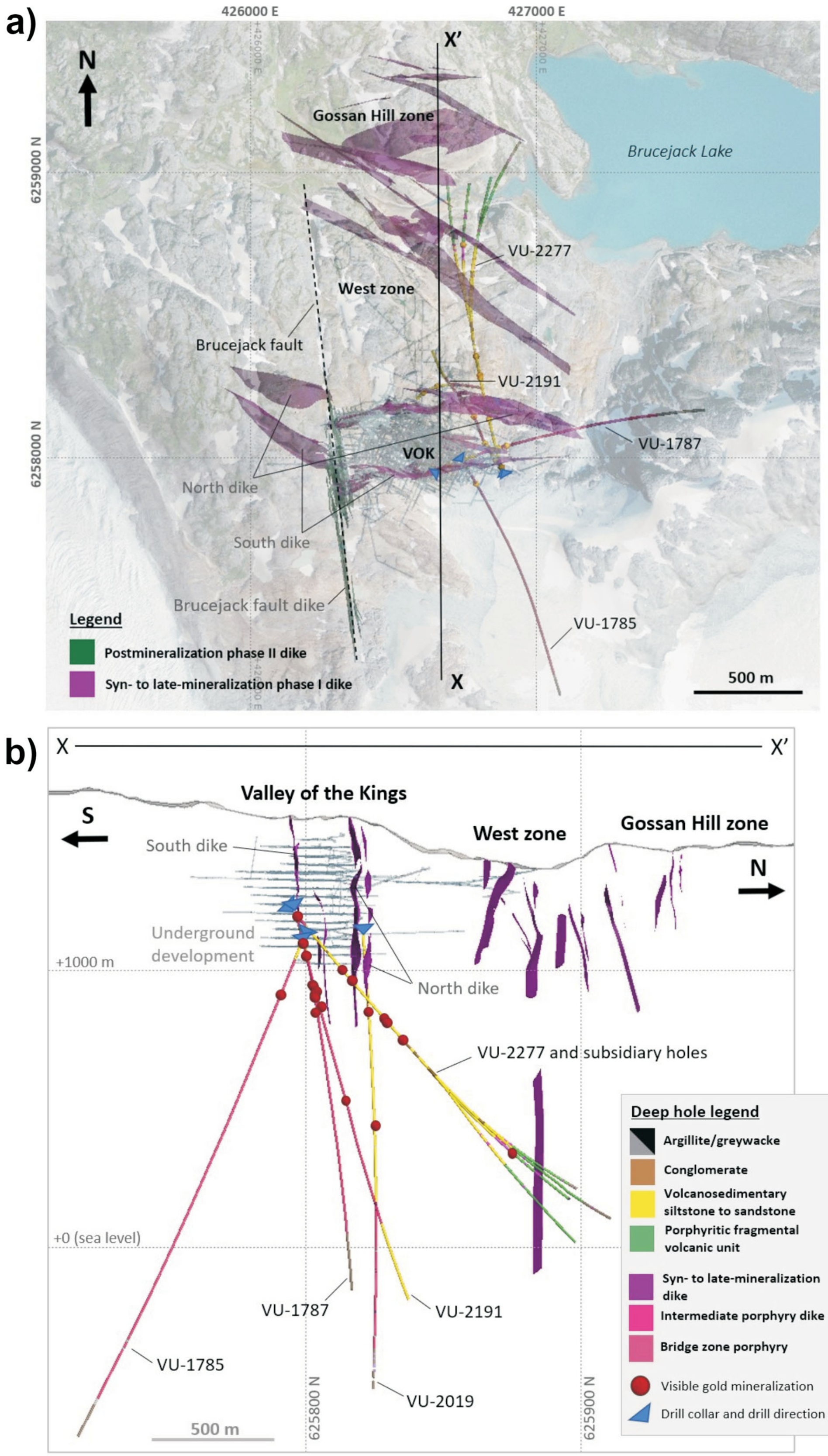

Figure 2. Valley of the Kings (VOK) zone and adjacent areas **a)** in plan view and **b)** in cross-section X-X', showing the extent of current mine development, the location and rock types of deep drillholes (e.g., VU-2277), the distribution of syn- to postmineralization dikes and intersections of bonanza-style gold in the deep holes.

Mitchell-Iron Cap and Eskay Creek. Stikinia is an allochthonous terrane, which evolved from an outboard intra-oceanic island-arc terrane within the peri-Laurentian realm during the mid-Paleozoic through to the initiation of end-on collision between the northern Stikinia microplate and the Yukon-Tanana terrane in the Late Triassic (212–200 Ma; Nelson et al, 2022). Closure of Stikinia against Quesnellia was initiated by counterclockwise rotation of the Stikinia arc and asymmetric advance of the Hazelton arc at ca. 189–185 Ma (Nixon et al., 2020). Ongoing accretion of Stikinia to the Laurentian margin and development of a back-arc tectonic regime occurred at ca. 185–178 Ma, which is coeval with the youngest lower Hazelton Group magmatism (Nelson et al., 2022).

The Valley of the Kings zone at Brucejack, which has been the focus of most of the current mine development, is located ~1 km southwest of Brucejack Lake (Figure 2a). The stratigraphy is characterized by a basal sequence of marine volcano-sedimentary rocks (ca. 195–194 Ma; Board et al., 2020; Nelson et al., 2022), including epiclastic volcanic sandstone, siltstone and mudstone, which are disconformably overlain by polymictic conglomerate comprising reworked, porphyritic intrusive and sedimentary pebbles to cobbles. The basal units were overlain by a transitional facies of fragmental andesite in a sandy matrix, which was succeeded by an upper andesitic volcanic sequence of agglomeratic latite flows and then by an uppermost andesitic to latitic potassium-feldspar–phyric crystal-tuff unit (Board et al. 2020; McLeish, 2022).

The Valley of the Kings zone experienced six stages of vein development (Tombe et al., 2018). Stage I and II veins are barren and consist of discontinuous pyrite-quartz-calcite stringers and translucent to white, microcrystalline quartz veinlets, respectively. Gold occurs predominantly in stage III to V quartz-carbonate-sericite veins, breccias and stockworks as electrum aggregates. Stage VI veins postdate mineralization and comprise quartz-calcite-chlorite tectonic-shear veins and/or tension gashes (Tombe et al., 2018). The auriferous veins crosscut most rock types (except postmineralization dikes), including all hydrothermally altered rock types and two generations of early foliation (Board et al., 2020).

The structures that focused the bonanza-grade quartz-carbonate stockworks were also exploited or locally cut by a generation of east-trending mafic dikes, here termed ‘phase I’ dikes, which have been interpreted as syn- to late mineralization, based on crosscutting relationships between the dikes and auriferous veins; phase I dikes cut, and are themselves cut, by auriferous veins (Tombe et al., 2018). Distinct from these dikes are a group of north-trending, postmineralization dikes, including the Brucejack fault dike (Figures 2a, 3e), which are referred to here as ‘phase II’ dikes; these dikes cut the auriferous veins and the phase I mafic dikes at high angles (Board et al., 2020). Drilling has demonstrated that intense phyllic alteration, bonanza-type gold mineralization, and the phase I and II dikes continue to at least 1300 m below the top of the present erosional surface in the Valley of the Kings zone (Figure 2b; McLeish, 2022), which exceeds the vertical extent (i.e., 50–700 m below the paleowater table) of most epithermal deposits (Hedenquist et al., 2000). In addition to the phase I and II dikes, five texturally and mineralogically distinct dikes have been encountered in deep exploration holes beneath the mine workings.

Spatial Distribution of Phase I and II Dikes in the Valley of the Kings Zone and Adjacent Areas

The syn- to late-mineralization phase I mafic dikes (i.e., North dike and South dike) respectively exploit two major east-trending, steeply dipping extensional and mineralized structures, the domain 13 and domain 20 faults (Figure 3a, b). These light green to milky green, aphanitic to fine-grained dikes, commonly metres to locally decimetres in width, exhibit moderate carbonate and chlorite alteration (Figure 3c, d). Calcite±chlorite–filled amygdules occur throughout the dikes, which have finely banded chilled margins. Phase I mafic dikes are porphyritic and are characterized by an aphanitic, magnetic groundmass that has been pervasively replaced by sericite and disseminated pyrite. Phenocrysts of hornblende and plagioclase have been replaced by sericite (Figures 3c, d, 4a). A 182.7 ±1.0 Ma U-Pb zircon age was obtained for North dike and is interpreted to provide a minimum age for the epithermal mineralization in the Valley of the Kings zone (Board et al., 2020).

In contrast, the postmineralization phase II dikes in the Valley of the Kings zone are dark grey to black, fine to medium grained, undeformed and relatively unaltered. They are characterized by poikilitic hornblende laths and fine-grained magnetite that is partly or fully enclosed by plagioclase oikocrysts (Figure 4b); these dikes exhibit weak propylitic alteration. The dikes are also steeply dipping, north-trending and occur proximal to, and along, the north-trending Brucejack fault, which crosscuts all hostrock types, gold mineralization and foliation (Board et al., 2020). Surface expressions of these dikes have been identified across the Valley of the Kings mine area and surrounding exploration areas, including metre-wide outcrops near the Gossan Hill zone (Figure 2a).

Numerous other dikes with variable orientation and composition (described below) were sampled from drillcore and outcrops adjacent to the mine areas, including veined syn- to late-mineralization dikes at Gossan Hill and relatively shallow-dipping dikes parallel to ore domains in the West zone (Figure 2b). Like the phase I mafic dikes in the Valley of the Kings zone, some of these dikes exploited

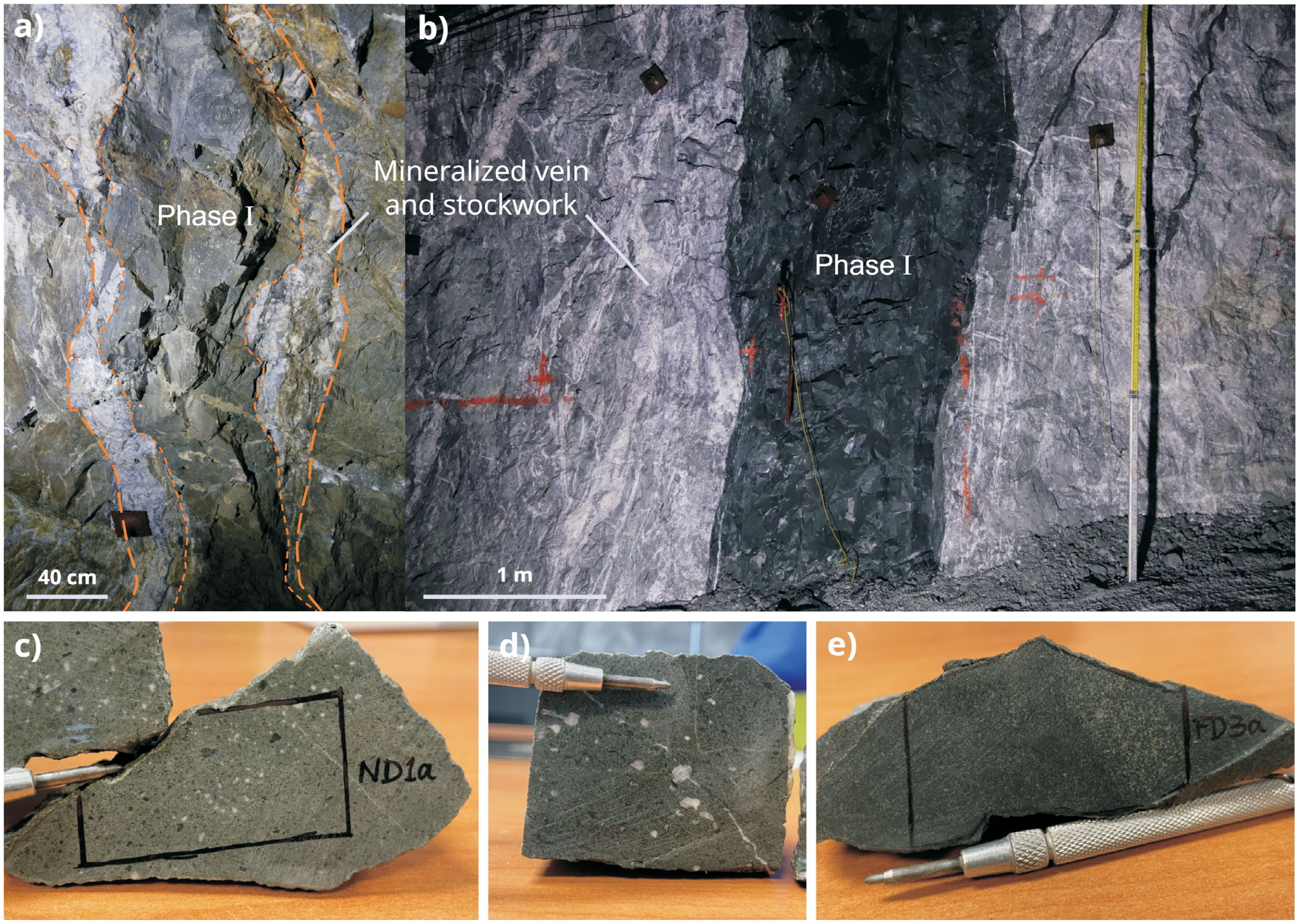

Figure 3. Representative photographs of mafic dikes showing the spatial relationships between mineralized quartz-carbonate stockworks and phase I mafic dikes underground in **a)** South dike and **b)** North dike, as well as in syn- to postmineralization dike hand samples from **c)** North dike phase I, **d)** South dike phase I and **e)** Brucejack fault dike phase II in the Valley of the Kings zone.

structural corridors similar to fault stockworks of mineralized domains 13 and 20, which host bonanza-grade gold and base-metal–sulphide mineralization.

The Vertical Extent of the Valley of the Kings Zone and Alteration

A deep-drilling program was conducted by Pretium Resources Inc. (acquired by Newcrest Mining Limited in 2022) between 2018 and 2020 to determine the vertical extent of gold mineralization beneath the Valley of the Kings zone and search for a potential magmatic source for the deposit. The dominant rock type in most of these holes is a variably altered (shallow phyllic alteration and deeper propylitic alteration) plagioclase- and hornblende-phyric porphyry, which is referred to by company geologists as the 'Bridge zone porphyry' because of its similarity to the main intrusive phase in the Bridge zone, a target of exploration near the Valley of the Kings zone. In drillholes VU-2277 and VU-2019 (Pretium Resources Inc., unpublished data, 2022), the main unit is a thick volcano-sedimentary package of sandy to silty sediments with local metre-thick interbeds of pebbly clast-supported oligomictic to polymictic conglomerates. The lowermost part of drillhole VU-2277 (Pretium Resources Inc., unpublished data, 2022) intersects a mafic, porphyritic fragmental volcanic unit that has an interval over 200 m long and is spatially associated with intermittent, metre-wide intermediate porphyry dikes (Figure 2b).

Mafic to intermediate dikes were encountered in all the deep holes and comprise both syn- to late-mineralization mafic–intermediate dikes and postmineralization mafic dikes, as well as other varieties of dikes (minor), which are described and classified below based on composition.

Results and Interpretation

Pervasive hydrothermal alteration and postmineralization metamorphism, up to subgreenschist facies (Board et al., 2020), have modified the primary compositions of the rocks in the Valley of the Kings zone and surrounding areas. As a result, mobile elements, such as potassium and sodium, cannot be used to assess the original compositions of most units. Therefore, relatively immobile elements (i.e.,

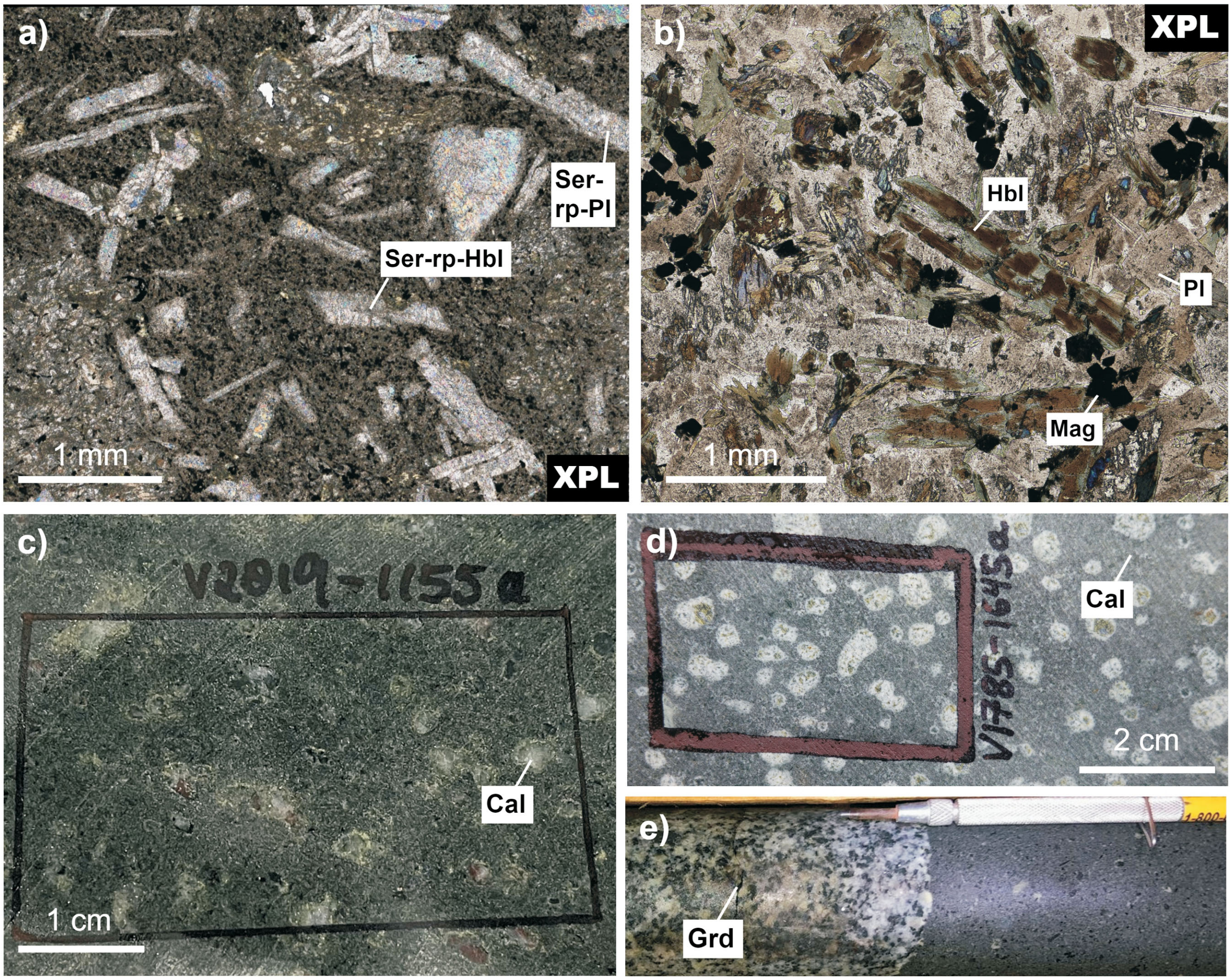

Figure 4. Photomicrographs of dikes from deep holes in the Brucejack deposit area and drillcore photographs of three texturally distinct intermediate to mafic dikes from Valley of the Kings mine workings: **a)** photomicrograph in cross-polarized light (XPL) of a syn- to late-mineralization phase I mafic dike containing sericite-replaced hornblende (Ser-rp-Hbl) and sericite-replaced plagioclase (Ser-rp-Pl) phenocrysts in a moderately sericitized groundmass; **b)** photomicrograph in cross-polarized light of a postmineralization phase II mafic dike containing large hornblende (Hbl) and plagioclase (Pl) phenocrysts that partly enclose smaller magnetite (Mag) euhedral crystals, which are also surrounded by groundmass; **c)** syn- to late-mineralization phase I mafic dike with calcite (Cal)-filled amygdule; **d)** relatively unaltered mafic dike with densely packed, calcite-(epidote)-filled vesicles; **e)** mafic to intermediate dike with a granodiorite (Grd) xenolith.

REEs and other high-field-strength elements [(HFSEs]) and their ratios were used to evaluate the primary geochemical characteristics of the dikes (Figure 5a, b). An immobile-element dataset of mine-hosted syn- to late-mineralization phase I dikes, including North and South dikes (Figure 2a, b), which are concordant with major mineralized domains, was evaluated and compared with a separate dataset for dikes intersected in the deep holes. Six types of texturally and geochemically distinct dikes were identified and are described below.

Syn- to Late-Mineralization Phase I Mafic Dikes

Metre-scale mafic dikes are common below the Brucejack deposit. They are aphanitic, green in colour, pervasively sericitized with local carbonate and chlorite alteration patches, and contain relics of hornblende and plagioclase, together with calcite-filled vesicles (Figure 4c). These dikes are similar to, and are considered to be, the deeper expression of the syn- to late-mineralization phase I mafic dikes in the mine, as they exhibit comparable mineralogy, textures, composition, alteration and relationships to veins (Figures 3–d, 4a, 5a). Both sets of dikes classify as subalkaline basalt (Figure 5a) and have higher V, Fe and Ti concentrations and lower Ba and Th than other dikes, except postmineralization mafic dikes.

Postmineralization Dikes

Most of the postmineralization dikes intersected in the deep holes are black to light grey, medium grained, relatively

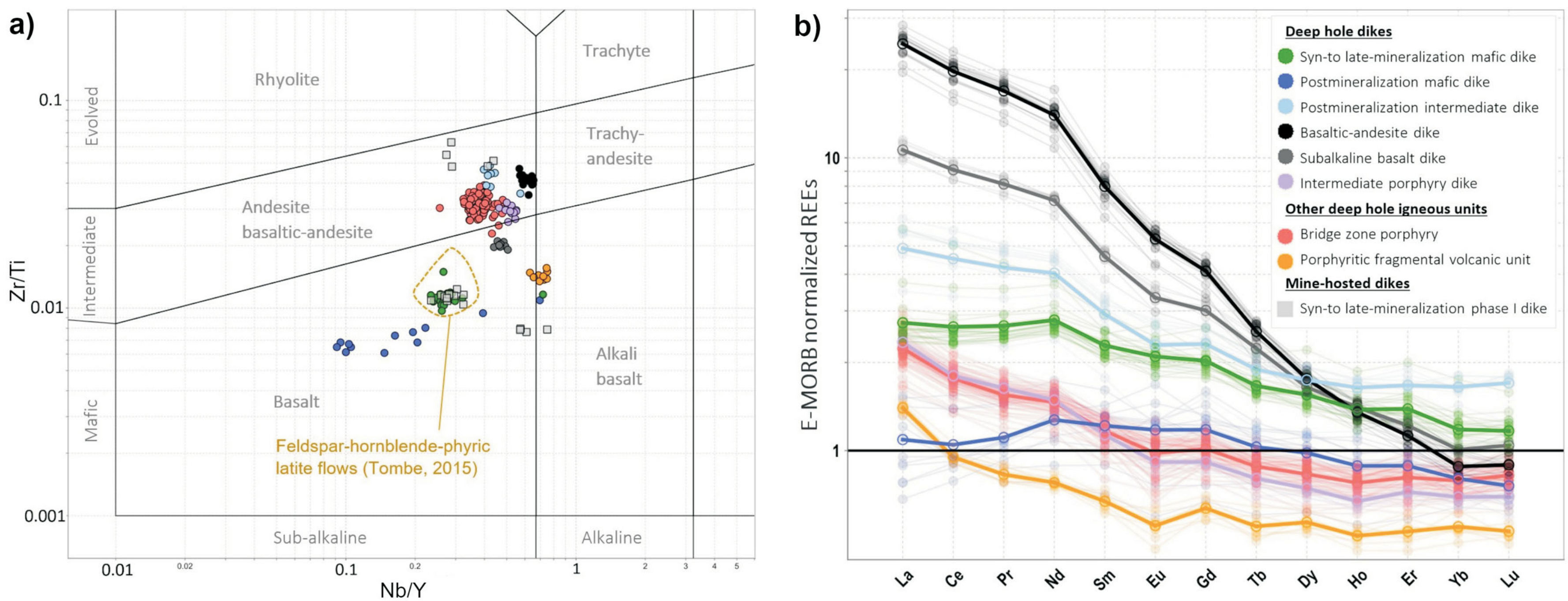

Figure 5. Geochemical characteristics of the dikes in the Brucejack deposit area: **a)** dike compositions on a volcanic-rock discrimination diagram of immobile-element ratios (Zr/Ti–Nb/Y; Pearce, 1996); **b)** dike REE profiles on a spider diagram normalized to enriched mid-ocean–ridge basalt (E-MORB; Sun and McDonough, 1989). Legend applies to both diagrams.

unaltered and undeformed. They can be divided into two geochemically distinct subclasses (corresponding to mafic and intermediate compositions) based on incompatible elements:

- Postmineralization mafic dikes that are typically dark grey to black, fine to medium grained, locally amygdaloidal and have a weakly sericite(-carbonate-chlorite)–altered groundmass, locally containing sericitized plagioclase phenocrysts; geochemically, they are characterized by elevated Cr, Sc, V and Ti contents and classify as subalkalic, tholeiitic basalt (Figure 5a).
- Postmineralization intermediate dikes that are typically grey to dark grey and fine to medium grained, plagioclase-phyric and either unaltered or locally weakly sericitized; they have relatively elevated concentrations of REEs and HFSEs, including Nb, Zr and P, and classify as andesitic basalt (Figure 5a).

Basaltic-Andesite Dikes

Basaltic-andesite dikes are restricted to depths greater than, or equal to, ~2 km below the erosional surface. They are relatively unaltered, dark grey, porphyritic, amygdaloidal and contain occasional granodiorite xenoliths (Figure 4e). These rocks are characterized by high concentrations of Ba, Sr, P, light REEs and most HFSEs, including Zr, Th and Nb (Figure 5b). Based on their immobile-element ratios, samples of this unit have a borderline alkaline affinity (Figure 5a).

Subalkaline Basalt Dikes

Subalkaline basalt dikes intersected in the deep holes are restricted to depths between 1 and 1.6 km below the current erosional level (Figure 2b) and are geochemically distinct. They are relatively unaltered, very dark grey, aphanitic and show minor or no evidence of deformation. Calcite amygdules are common (Figure 4d) as is decimetre-wide layering, suggesting multiple injections of magma. These dikes are more mafic than the basaltic-andesite dikes, as shown by their high concentrations of Cr, Ti and Co. However, they have E-MORB–normalized REE profiles similar to the basaltic-andesite dikes, albeit with lower absolute-element concentrations (Figure 5b). The immobile-element ratios indicate that the dikes are subalkaline to borderline alkaline and basaltic (Figure 5a).

Intermediate Porphyry Dikes and Bridge Zone Porphyry

The intermediate porphyry dikes and the mineralized Bridge zone porphyry have indistinguishable trace-element compositions; both classify as subalkaline intermediate intrusions (Figure 5a). Both the Bridge zone porphyry and the intermediate porphyry dikes are characterized by relatively high concentrations of Th (3.12–5.04 ppm), whereas those of Ti, P and REEs (ΣTREE: 55–86 ppm) are low. They have Zr, Nb and REE concentrations and La/Yb ratios ([La/Yb]N: 3.88–7.65) similar to those of the syn- to late-mineralization mafic dikes.

Porphyritic Fragmental Volcanic Unit

The porphyritic fragmental volcanic unit classifies as an alkali basalt and is characterized by low concentrations of REEs (ΣTREE: 40–45 ppm), with slightly enriched light REEs and almost flat middle and heavy REE profiles (Figure 5b).

Discussion

The REE concentrations of all intermediate- to mafic-dike generations (except deep postmineralization mafic dikes) are characterized by light and middle REE enrichment relative to E-MORB and other igneous units (i.e., the Bridge zone porphyry, the intermediate porphyry dikes and the porphyritic fragmental volcanic unit; Figures 2b, 5b). The postmineralization mafic dikes have profiles very similar to E-MORB, with slightly elevated middle REE concentrations (Figure 5b). All units are readily distinguished one from the other by their REE profiles as well as their La/Yb, Ti/Yb, Th/Yb and Nb/Yb ratios (Figures 5b, 6a, b).

Syn- to late-mineralization phase I mafic dikes exposed in the mine and intersected in drillholes below are closest in affinity to E-MORB in terms of their TiO_2/Yb, Th/Yb and Nb/Yb ratios (Figure 6a, b), which may indicate the incorporation of enriched lithosphere (Pearce, 2008). In addition, the high Nb/Yb (2.38–3.52) and low Ti/Yb (0.50–0.71) ratios suggest a low degree of partial melting (<5%) from a relatively shallow, low-temperature mantle source (2.0–2.5 GPa) that is atypical of subduction-related arc magmas (Pearce, 2008). These ratios, however, could reflect a higher degree of partial melting (10–13%) of a more deeply sourced alkalic magma (Pearce, 2008). As the Brucejack deposit is spatially and temporally linked to other alkaline systems in the Golden Triangle, consideration should be given to the possibility that the phase I-type dikes represent mafic alkalic intrusions related to postsubduction extension. More specifically, the phase I syn- to late-mineralization mafic dikes may provide further evidence of mafic alkalic magmatism related to Pliensbachian postcollisional back-arc extension in Stikinia and the ultimate demise of the Hazelton volcanic arc (Nelson et al., 2022).

Significantly, the phase I dikes have Zr/Ti and Nb/Y ratios that are indistinguishable from those of the broadly coeval (182.6 ±1.1 Ma; McLeish, 2022) mineralized andesitic to latitic potassium-feldspar–phyric crystal-tuff unit (Figure 5a). Indeed, based on their similar ages, these phase I-dike corridors are considered to be the feeder structures for the latite flows (Board et al, 2020), which are interpreted to have been mineralized soon after eruption, given that the

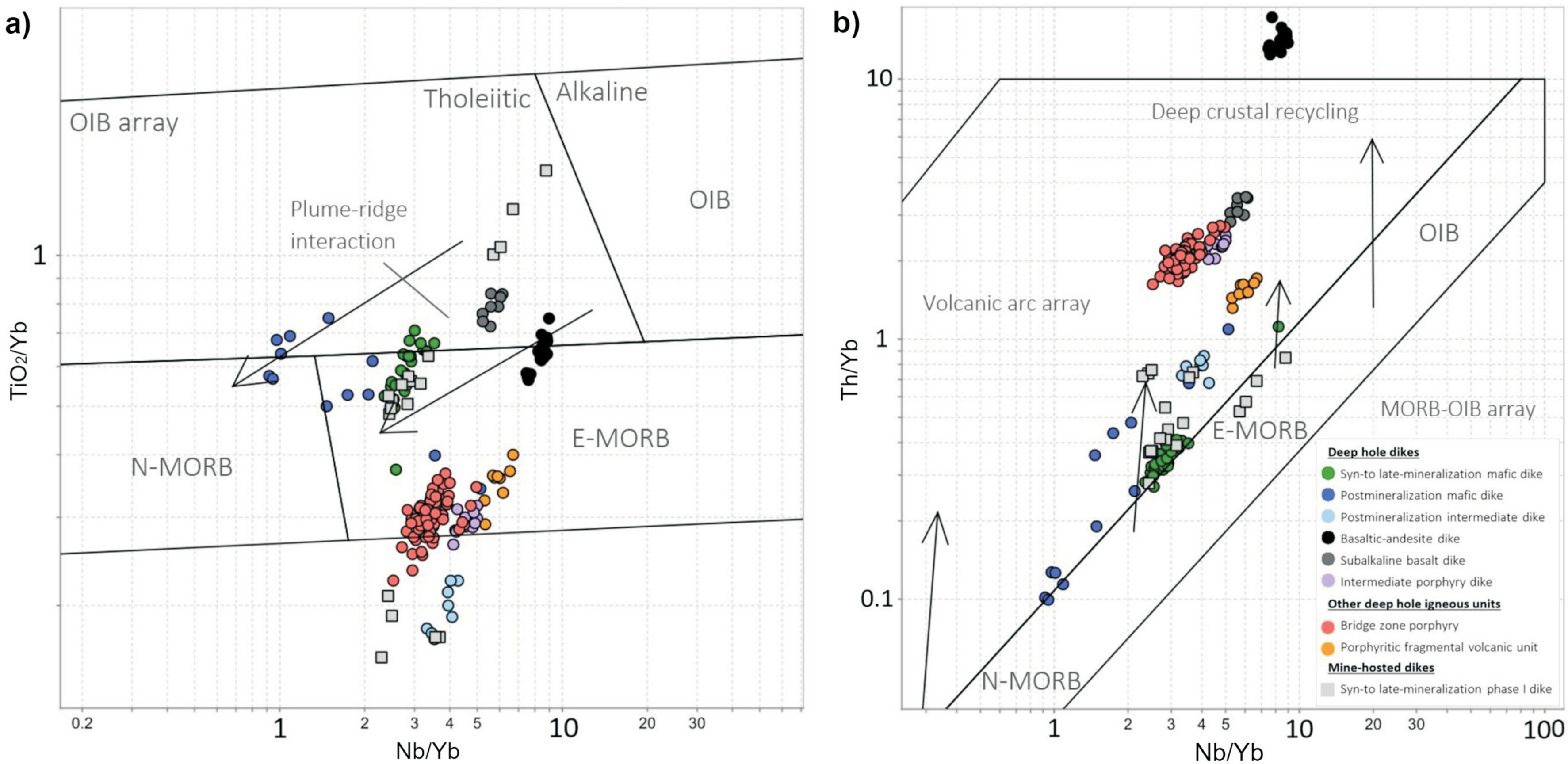

Figure 6. Immobile-element–ratio diagrams of dike compositions in the Brucejack deposit area designed to illustrate the effect of various petrogenetic processes (Pearce, 2008): **a)** TiO_2/Yb versus Nb/Yb; **b)** Th/Yb versus Nb/Yb (legend applies to both diagrams). Abbreviations: E-MORB, enriched mid-ocean–ridge basalt; N-MORB, normal (N-type) mid-ocean–ridge basalt; OIB, oceanic-island basalt.

dikes cut the early stage mineralized veins. Although the source of the syn- to late-mineralization mafic magmas remains uncertain, it seems likely that hydrothermal circulation associated with the gold mineralization may have been driven by an intrusion of this type at depth below the Valley of the Kings zone.

The postmineralization phase II mafic dikes display a primitive island-arc tholeiitic affiliation, as suggested by their E-MORB–like REE profiles (ΣTREE: 42–65 ppm; [La/Yb]N: 1.64–3.69) and their high Fe, Cr and Co contents. The Nb/Yb (0.92 5.13) and Th/Yb (0.10–1.09) ratios are highly variable and trend from N-MORB–like to continental-arc–like basaltic compositions (Figure 6b). This may signify a continental component in the ascending magmas. In contrast, the postmineralization intermediate dikes are relatively rich in REEs (ΣTREE: 142–214 ppm), especially the heavy REEs, whereas REE fractionation is subtle (Figure 5b). Given the relative enrichment in REEs and HSFEs in these dikes, they likely evolved from enriched mantle contaminated by crust (Pearce, 2008). As the age of the postmineralization intrusive event is still undetermined, the relationship between the mafic and intermediate subunits remains unclear.

The basaltic-andesite (BA) and subalkaline basalt dikes (SAB) have similar REE profiles, are relatively enriched in light and middle REEs, and are strongly fractionated. Basaltic rocks with very high (La/Yb)N ratios (BA: 42.8–58.3; SAB: 17.5–20.8) and no apparent depletion in Nb, Ta and Ti are commonly classified as alkaline (Weaver, 1991), although in Figure 5a they classify as subalkaline (the BA is borderline alkaline). Significant contributions by crustal components may have caused the high Th/Yb ratios (BA: 12.5–17.3; SAB: 2.82–3.52) of both dike types (Figure 6b). It is tentatively proposed that these magmas were sourced from a deep mantle after a low degree of partial melting and subsequently assimilated crustal material. From their similar geochemical signatures and close spatial association, it is further proposed that the BA and SAB dikes are genetically related and that the BA magma is probably an evolved product of the SAB magma.

Conclusions and Future Work

Six types of dikes were classified at the Brucejack deposit, based on their immobile-element (i.e., rare-earth elements, high-field-strength elements) concentrations and ratios and on their enriched mid-ocean–ridge basalt–normalized rare-earth element distributions. Discrimination diagrams suggest a geochemical affinity ranging from subalkaline basalt for the syn- to late-mineralization dikes to basaltic-andesite. Systematic differences in rare-earth element profiles (i.e., ΣREE, [La/Yb]N) and the concentrations of other high-field-strength elements suggest an enriched magma source that could possibly have been generated during rifting. The discrimination diagrams also suggest a genetic link between the syn- to late-mineralization mafic dikes intersected in deep drillholes and those occurring within high-grade mineralized corridors in the mine (Figure 5a).

Syn- to late-mineralization mafic dikes are characterized by moderate Ti/Yb and Nb/Yb ratios and may have been emplaced during back-arc rifting. Postmineralization structural events (e.g., the development of the Brucejack fault) are believed to have controlled emplacement of the postmineralization dikes, which experienced variable degrees of fractionation, leading to two subclasses (i.e., mafic and intermediate). Evidence of enrichment in immobile elements and strong rare-earth element fractionation in the basaltic-andesite and subalkaline basalt dikes suggest a deep mantle source and a high degree of crustal interaction.

Uranium-lead age determinations and a trace-element study of zircon and baddeleyite in the dikes will be used to further evaluate the magmatic evolution of the Brucejack area and gain additional insights into possible magmatic relationships with the gold mineralization. To assess the ages of the intrusive phases, zircon (and, if possible, baddeleyite) will be separated from all classes of intermediate to mafic dikes in the Brucejack area and will be evaluated by a cathodoluminescence imaging system coupled to a scanning electron microscope to distinguish primary magmatic zircon from possibly inherited zircon (Miller et al., 2007). Depending on the complexity of crystal growth and the morphology of the target grains, U-Pb age determinations will be conducted by either laser-ablation inductively coupled plasma–mass spectrometry or isotope dilution–thermal ionization mass spectrometry. The trace-element chemistry of the different growth phases of the target crystals will be evaluated from the results of laser-ablation inductively coupled plasma–mass spectrometry analyses. In addition, statistical analyses, including principal-component analysis, will be performed to assess the correlations between gold content and element concentrations attributable to alteration and magmatic processes.

Acknowledgments

Major funding for this project is being provided by the Natural Sciences and Engineering Research Council of Canada (NSERC) and Newcrest Mining Limited (Newcrest). Special acknowledgment is given to O.V. Vasyukova for reviewing this summary paper. The lead author is also grateful to Geoscience BC for its financial support through the Geoscience BC Scholarship program. Technical and logistical support provided by the crew of Newcrest at the Brucejack deposit is gratefully acknowledged. Lastly, O. Bath and J. Madsen are thanked for providing the lithogeochemical data for the mine-hosted dikes and T. Dawson, for expert assistance in producing the maps and cross-section.

References

ALS (2022): Geochemistry, 2022 schedule of services and fees; ALS, 50 p., URL <https://www.alsglobal.com/en/geochemistry/geochemistry-fee-schedules> [November 2022].

Arribas, A., Hedenquist, J.W., Itaya, T., Okada, T., Concepcion, R.A. and Garcia, J.S. (1995): Contemporaneous formation of adjacent porphyry and epithermal Cu-Au deposits over 300 ka in northern Luzon, Philippines; Geology, v. 23, p. 337–340.

Board, W.S., McLeish, D.F., Grieg, C.J., Bath, O.E., Ashburner, J.E., Murphy, T. and Friedman, R.M. (2020): The Brucejack Au-Ag deposit, northwest British Columbia, Canada: multistage porphyry to epithermal alteration, mineralization, and deposit formation in an island-arc setting; chapter 14 *in* Geology of the World's Major Gold Deposits and Provinces, R.H. Sillitoe, R.J. Goldfarb, F. Robert and S.F. Summers (ed.), Society of Economic Geologists, Special Publication, v. 23, p. 289–311, URL <https://doi.org/10.5382/SP.23>.

Gammons, C.H. and Williams-Jones, A.E. (1997): Chemical mobility of gold in the porphyry-epithermal environment; Economic Geology, v. 92, no. 1, p. 45–59.

Hayba, D.O., Bethke, P.M., Heald, P. and Foley, N.K. (1985): Geologic, mineralogic and geochemical characteristics of volcanic-hosted epithermal precious-metal deposits; Reviews in Economic Geology, v. 2, p. 129–168.

Hedenquist, J.W. (1995): The ascent of magmatic fluid: discharge versus mineralization; *in* Magmas, Fluids, and Ore Deposits, J.F.H. Thompson (ed.), Mineralogical Association of Canada, Short Course Series, v. 23, p. 263–289.

Hedenquist, J.W., Arribas A.R. and Gonzalez-Urien, E. (2000): Exploration for epithermal gold deposits; chapter 7 *in* Gold in 2000, S.G. Hagemann and P.E. Brown (ed.), Society of Economic Geologists, Reviews in Economic Geology, v. 13, p. 245–277, URL <https://doi.org/10.5382/Rev.13>.

Heinrich, C. A., Driesner, T., Stefánsson, A. and Seward, T.M. (2004): Magmatic vapor contraction and the transport of gold from the porphyry environment to epithermal ore deposits; Geology, v. 32, no. 9, p. 761–764.

Johnston, S.T. (2008): The Cordilleran ribbon continent of North America; Annual Review of Earth and Planetary Sciences, v. 36, p. 495–530.

McLeish, D.F. (2013): Structure, stratigraphy, and U-Pb zircon-titanite geochronology of the Aley carbonatite complex, northeast British Columbia: evidence for Antler-aged orogenesis in the Foreland Belt of the Canadian Cordillera; M.Sc. thesis, University of Victoria, 142 p.

McLeish, D.F. (2022): The nature and origin of the bonanza-grade Brucejack epithermal Au-Ag deposit, Northwestern British Columbia; Ph.D. thesis, McGill University, 192 p.

McLeish, D.F., Williams-Jones, A.E., Board, W.S. and Clark, J.R. (2018): Nature and origin of the Brucejack high-grade epithermal gold deposit, northwestern British Columbia (NTS 104B): 2017 update; *in* Geoscience BC Summary of Activities 2017: Minerals and Mining, Geoscience BC, Report 2018-01, p. 31–40, URL <https://www.geosciencebc.com/summary-of-activities-2017-minerals-and-mining/> [November 2022].

McLeish, D.F., Williams-Jones, A.E., Vasyukova, O.V., Clark, J.R. and Board, W.S. (2021): Colloidal transport and flocculation are the cause of the hyperenrichment of gold in nature; Proceedings of the National Academy of Sciences, v. 118, no. 20, art. e2100689118, URL <https://doi.org/10.1073/pnas.2100689118>.

Miller, J.S., Matzel, J.E., Miller, C.F., Burgess, S.D. and Miller, R.B. (2007): Zircon growth and recycling during the assembly of large, composite arc plutons; Journal of Volcanology and Geothermal Research, v. 167, no. 1–4, p. 282–299.

Nelson, J.L., van Straaten, B. and Friedman, R. (2022): Latest Triassic–Early Jurassic Stikine-Yukon-Tanana terrane collision and the onset of accretion in the Canadian Cordillera: insights from Hazelton Group detrital zircon provenance and arc–back-arc configuration; Geosphere, v. 18, no. 2, p. 670–696.

Nelson, J., Waldron, J., van Straaten, B., Zagorevski, A. and Rees, C. (2018): Revised stratigraphy of the Hazelton Group in the Iskut River region, northwestern British Columbia; *in* Geological Fieldwork 2017, BC Ministry of Energy, Mines and Low Carbon Innovation, BC Geological Survey Paper 2018-01, p. 15–38, URL <https://cmscontent.nrs.gov.bc.ca/geoscience/PublicationCatalogue/Paper/BCGS_P2018-01-02_Nelson.pdf> [November 2022].

Nixon, G.T., Scheel, J.E., Scoates, J.S., Friedman, R.M., Wall, C.J., Gabites, J. and Jackson-Brown, S. (2020): Syn-accretionary multistage assembly of an Alaskan-type intrusion in the Canadian Cordillera: U-Pb and ^{40}Ar/^{39}Ar geochronology of the Turnagain ultramafic-mafic intrusive complex, Yukon-Tanana terrane; Canadian Journal of Earth Sciences, v. 57, p. 575–600.

Pearce, J.A. (1996): A user's guide to basalt discrimination diagrams; *in* Trace Element Geochemistry of Volcanic Rocks: Applications for Massive Sulphide Exploration, D.A. Wyman (ed.), Geological Association of Canada, Short Course Notes, v. 12, p. 79–113.

Pearce, J.A. (2008): Geochemical fingerprinting of oceanic basalts with applications to ophiolite classification and the search for Archean oceanic crust; Lithos, v. 100, no. 1–4, p. 14–48.

Sillitoe, R.H. and Hedenquist, J.W. (2005): Linkages between volcanotectonic settings, ore-fluid compositions, and epithermal precious metal deposits; chapter 16 *in* Volcanic, Geothermal, and Ore-Forming Fluids: Rulers and Witnesses of Processes Within the Earth, S.F. Simmons and I.J. Graham (ed.), Society of Economic Geologists, Special Publication, v. 10, p. 315–343, URL <https://doi.org/10.5382/SP.10.16>.

Sun, S.-S. and McDonough, W.F. (1989): Chemical and isotopic systematics of oceanic basalts: implications for mantle composition and processes; Geological Society of London, Special Publications, v. 42, no. 1, p.313–345.

Tetra Tech (2020): March 2020 technical report and mineral resources update, Brucejack mine; National Instrument 43-101 Technical Report prepared for Pretium Resources Inc., 383 p.

Tombe, S.P. (2015): Age and origin of the Brucejack epithermal Au-Ag deposit, northwestern British Columbia; M.Sc. thesis, University of Alberta, 116 p.

Tombe, S.P., Richards, J.P., Greig, C.J., Board, W.S., Creaser, R.A., Muehlenbachs, K.A., Larson, P.B., DuFrane, S.A. and Spell, T. (2018): Origin of the high-grade early Jurassic Brucejack epithermal Au-Ag deposits, Sulphurets mining camp, northwestern British Columbia; Ore Geology Reviews, v. 95, p. 480–517.

Tosdal, R.M., Dilles, J.H. and Cooke, D.R. (2009): From source to sinks in auriferous magmatic-hydrothermal porphyry and epithermal deposits; Elements, v. 5, no. 5, p. 289–295.

Weaver, B.L. (1991): The origin of ocean island basalt end-member compositions: trace element and isotopic constraints; Earth and Planetary Science Letters, v. 104, no. 2–4, p. 381–397.

Williams-Jones, A.E. and Heinrich, C.A. (2005): 100th Anniversary special paper: vapor transport of metals and the formation of magmatic-hydrothermal ore deposits; Economic Geology, v. 100, no. 7, p. 1287–1312.

Investigating Unsupervised Machine-Learning Classification of British Columbia Copper-Porphyry Ore and Indicator Minerals Using Micro-X-Ray–Fluorescence Core Scanners

B. Eaton[1], **Department of Earth, Ocean and Atmospheric Sciences, The University of British Columbia, Vancouver, British Columbia, beaton@eoas.ubc.ca**

A. Steiner, Department of Earth, Ocean and Atmospheric Sciences, The University of British Columbia, Vancouver, British Columbia

S. Barker, Department of Earth, Ocean and Atmospheric Sciences, The University of British Columbia, Vancouver, British Columbia

L. Heagy, Department of Earth, Ocean and Atmospheric Sciences, The University of British Columbia, Vancouver, British Columbia

Eaton, B., Steiner, A., Barker, S. and Heagy, L. (2023): Investigating unsupervised machine-learning classification of British Columbia copper-porphyry ore and indicator minerals using micro-X-ray–fluorescence core scanners; *in* Geoscience BC Summary of Activities 2022: Minerals, Geoscience BC, Report 2023-01, p. 37–44.

Introduction

Copper-porphyry deposits are large-tonnage, low-grade, intrusive mineral deposits that range from less than 10 Mt to 10 Gt grading 0.5 to 1.5% Cu (Sillitoe, 2010). Copper-porphyry systems host over three-quarters of the global copper resources and are thus a vital source for meeting the world's current and future copper demand (Sillitoe, 2010). As the world transitions to a decarbonized economy, copper is increasingly required to support global electrification upgrades to industrial systems as well as transportation and low-carbon energy infrastructure. The increasing global population and infrastructure-electrification upgrades will cause the global demand for copper to rise by a predicted 275% to 350% by 2050 (Elshkaki et al., 2016; Ciacci et al., 2020). New mineral-deposit discoveries are critical to meeting this demand; however, the remaining undiscovered deposits are in regions that are mostly or entirely hidden under hundreds of metres of postmineral cover material (Gonzalez-Alvarez et al., 2020). Exploring through postmineral cover adds significant complications and challenges to the discovery of new mineral deposits (Eppinger et al., 2013). Effective, timely and economically feasible exploration technologies must be developed to meet the rise in copper demand and address the challenges associated with exploring under increasing depths of postmineral cover (Gonzalez-Alvarez et al., 2020).

This research will contribute to the development of cost-effective, efficient and quantitative exploration techniques for porphyry-copper exploration under sedimentary cover material in British Columbia (BC) and will be applicable to any exploration program utilizing detrital indicator-mineral (DIM) methods. The research objectives of the project are to improve, quantify and expedite the identification of copper ore and gangue minerals, focusing primarily on Cu-porphyry DIMs, using methods that will be developed on samples from Cu-porphyry exploration programs and producing Cu-porphyry mines in BC. The research objectives will be achieved by developing a quantitative approach to indicator-mineral identification that overcomes the limitations of conventional DIM methods that include the handpicking of mineral grains and prohibitive costs associated with scanning electron microscope (SEM) analysis. The aim of the research is to develop Cu-porphyry DIM-identification methods using benchtop micro-X-ray–fluorescence (µXRF) core scanners. The µXRF DIM-identification methods will be evaluated against SEM analysis of samples from producing BC Cu-porphyry mines and Cu-porphyry exploration programs.

Background Information

Indicator Minerals

Indicator minerals are minerals that contain textural or chemical information indicating the presence of specific mineralization in the bedrock from which the minerals originally came (McClenaghan et al., 2000). In Cu-porphyry exploration, indicator minerals have been widely used as geochemical and detrital vectoring tools (Eppinger et al., 2013; Cooke et al., 2020). Detrital indicator minerals are derived from sediments such as glacial till, stream and lake sediments, or soil samples. Detrital indicator minerals have been used to explore for various mineral resources in-

[1]*The lead author is a 2022 Geoscience BC Scholarship recipient.*

This publication is also available, free of charge, as colour digital files in Adobe Acrobat® PDF format from the Geoscience BC website: http://geosciencebc.com/updates/summary-of-activities/.

cluding diamonds, gold, precious gems, base-metal sulphides and Cu–Ni–platinum-group element sulphides (McClenaghan, 2005; Gent et al., 2011). The use of DIMs has led to the discovery of numerous Canadian deposits and DIM methods can also be used to explore for Cu-porphyries in BC (Plouffe et al., 2016).

Detrital Indicator-Mineral Methods

Methods that rely on DIMs generally involve sampling, phase segregation and handpicking under an optical microscope by a human expert and/or SEM analysis (McClenaghan and Layton-Matthews, 2017). Optical grain counting and handpicking DIMs is labour intensive, inherently human biased and subjective, and results in both costly and slow analysis compared to automated mineralogical methods (Gent et al., 2011; Sylvester, 2012). Automated mineralogy using SEM analysis has been widely applied to DIMs; the method offers improvements in repeatability, quantification and automation (Lougheed et al., 2020). The challenges to applying widespread automated SEM analysis to a DIM exploration program are the high costs associated with the method and the relatively long amount of time required for sample preparation, analysis and data interpretation.

Benchtop µXRF Core Scanners

Analysis of DIMs by high-resolution µXRF core scanners offers a promising alternative to SEM-based methods, or may be complementary to these methods, when applied to DIMs. High-resolution (in the order of tens of microns) µXRF core scanners have been widely used by the paleoclimate scientific community to investigate paleosediment cores for the past two decades (Jansen et al., 1998). The µXRF analytical approaches used in paleoclimate research are increasingly being applied to the geosciences and mineral and petroleum industries (Croudace et al., 2019). Geological applications include sedimentary-core trace-metal analysis (Hennekam et al., 2019), characterization of volcanic debris (Peti et al., 2019) and mineral mapping in Carlin-type gold systems (Barker et al., 2021). The petroleum and mining industries have used benchtop µXRF analysis for tailings characterization (Fawcett and Jamieson, 2011; Galloway et al., 2018), tying of geochemical signatures to mechanical properties of rocks (Hussain et al., 2018) and geochemical characterization of stratigraphy in unconventional reservoirs (Hussain et al., 2022). Use of µXRF core scanners presents an opportunity to rapidly characterize DIMs to aid in the search for Cu-porphyry deposits.

Automated Mineral Identification

Artificial intelligence and machine-learning (ML) applications have undergone widespread innovation in mining and the geological sciences in the past ten years (Jooshaki et al., 2021). Machine learning is an area of study with a set of methods that extracts meaningful patterns and associations from known information that can be generalized and applied to new data to make predictions under uncertainty (Jordan and Mitchell, 2015). The ML methods investigated in this study can broadly be grouped into two categories: supervised and unsupervised methods. Supervised ML methods are a broad family of algorithms that are first trained on labelled data and then applied to predict labels on test or new data, whereas unsupervised ML methods are applied to unlabelled data. Structural and relational properties within the data are extracted by unsupervised methods and these relationships are used to cluster or reduce the dimensionality of the dataset (Jordan and Mitchell, 2015).

Automated mineral identification has been widely implemented in mining and the geosciences since the early 2000s using automated scanning electron microscopy (Gottlieb et al., 2000). Automated mineral-identification methods can also be grouped into two theoretical approaches: supervised classification methods using mineral standard-spectral libraries and unsupervised clustering methods (Schulz et al., 2020; Jooshaki et al., 2021). Automated SEM analysis predominantly identifies minerals by comparing the energy dispersive spectroscopy (EDS) spectra of a phase to known EDS spectra in a mineral standard-spectral library to determine the best match. Alternatively, phases can be identified without a mineral standard-spectral library by resorting instead to unsupervised clustering of similar EDS spectra into distinct separate groupings representing phases present in the sample. Unsupervised clustering allows for phases to be identified without building an extensive database; however, the method still requires user input to relate clusters of similar spectra to the mineral(s) that generated them. Furthermore, there is widespread potential to apply modern supervised and unsupervised methods to EDS spectra and other electron-microbeam analyses used to identify minerals, including µXRF (Jooshaki et al., 2021). For example, supervised neural networks have been applied to generate mineral maps by classifying integrated µXRF and micro-X-ray–diffraction (µXRD) data of fine-grained shale units to model mineral reactivity (Kim et al., 2022).

Methodology

Geochemical µXRF Analysis

An M4 Tornado Plus benchtop µXRF core scanner, manufactured by Bruker and equipped with a rhodium tube and two 260 mm^2 silicon drift EDS detectors with ultra-thin windows, was used for the analysis. Standard analytical parameters of 19 µm X-ray beam width, 100 µm pixel resolution, 10 ms/pixel dwell time, double detector channels, 50 kV acceleration voltage and chamber pressure of 1 mbar were used. The M4 Tornado Plus has a mapping area of 190 by 160 mm.

Benchtop µXRF core scanners nondestructively analyze whole-rock samples producing two-dimensional arrays of XRF spectra (Flude et al., 2017). A two-dimensional array of XRF spectra per pixel was produced representing the geochemical variation across the sample. Chemical maps, also commonly referred to as 'elemental maps', were produced by matching elemental peaks to the XRF spectral peaks identified in the scanned XRF spectra from the bulk composition of the sample. Areas of interest were selected for later quantification using the M4 Tornado Plus software package.

Elemental quantification was completed in the Bruker ESPRIT 2.4 software. The ESPRIT software is more efficient in quantifying elemental concentrations to acquire large chemical maps than the M4 software due to its multicore processing capabilities. Normalized, quantitative elemental abundances were derived for each pixel from the XRF spectra using the 'oxides' quantification method from the Bruker Quantitative Mapping (QMap) tool, which relies on fundamental-parameters standardless quantification to determine elemental concentrations from the XRF spectra (Kanngießer, 2003). Fundamental-parameters standardless-XRF quantification has been determined to be the best quantification method for heterogeneous rock samples due to the high geochemical variation found within geological material (Flude et al., 2017; Barker et al., 2021). Future work will validate the use of this method applied to Cu-porphyry DIMs. Both quantified and normalized elemental-concentration data were collected.

Exploratory Data Analysis

Exploratory data analysis of the quantified chemical maps was completed in Python, a high-level programming language. A dimension-reduction algorithm was used to transform the quantified compositional data from multidimensional elemental space to two-dimensional space. An unsupervised ML clustering method was applied to the transformed two-dimensional data to identify distinct clusters. The mineral names or mineral groups represented by similar compositional clusters were determined by the bulk chemistry of the cluster. Quantified elemental and mineral maps were produced using a data-visualization package.

Samples

A 5 by 16 cm piece of granitic Cu-porphyry core was scanned with a Bruker M4 Tornado Plus core scanner at the Electron Microbeam and X-Ray Diffraction Facility (Vancouver, BC), associated with the Mineral Deposit Research Unit of The University of British Colombia (Figure 1). The sample was mineralized with chalcopyrite and pyrite recognized in hand sample. Gangue minerals present in the sample were quartz, feldspar, amphibole and mica. A mosaicked RGB image of the sample was captured at 100x magnification (Figure 1); the area of the sample shown in the inset on Figure 1 was selected for chemical quantification and normalization.

Preliminary Results

Chemical Maps

Using a visualization package in Python, chemical maps were produced from exported quantified and normalized elemental concentrations determined using the Bruker ESPRIT QMap tool. Preliminary quantified chemical maps of Si, Al, K, Ca, Mg and P are shown in Figure 2, while S, Cu and Fe are presented in Figure 3. The µXRF chemical maps of geological material represent the relative geochemical variations within a sample, which are controlled by the distribution and composition of minerals in the sample (Barker et al., 2021). For example, the Si and Al chemical maps clearly show quartz veins surrounded by an

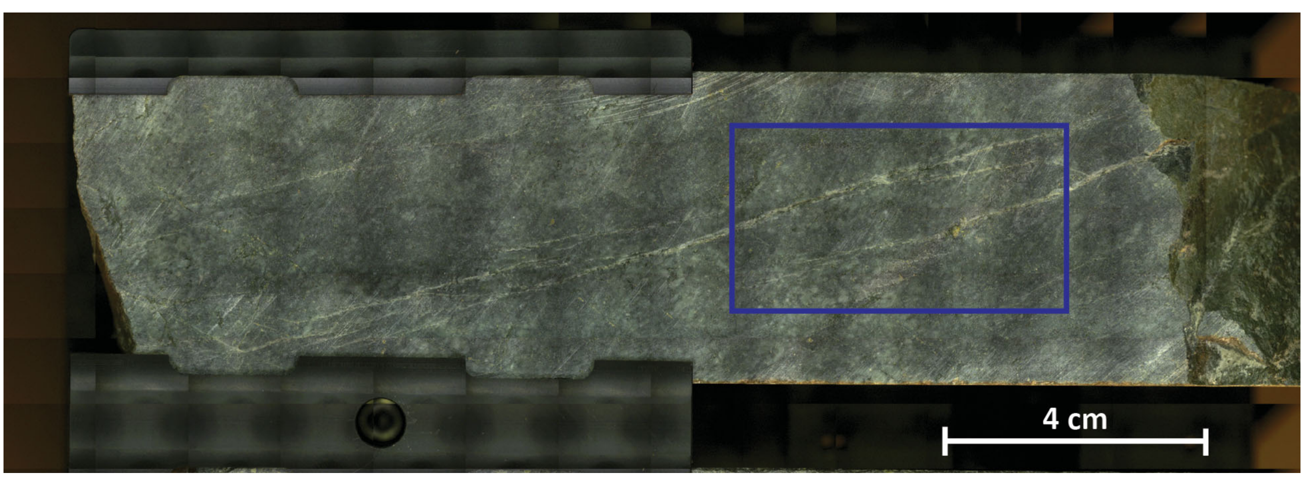

Figure 1. Mosaic of the Cu-porphyry core captured by the camera in the chamber of the Bruker M4 Tornado Plus core scanner (inset shows area that was selected for quantification).

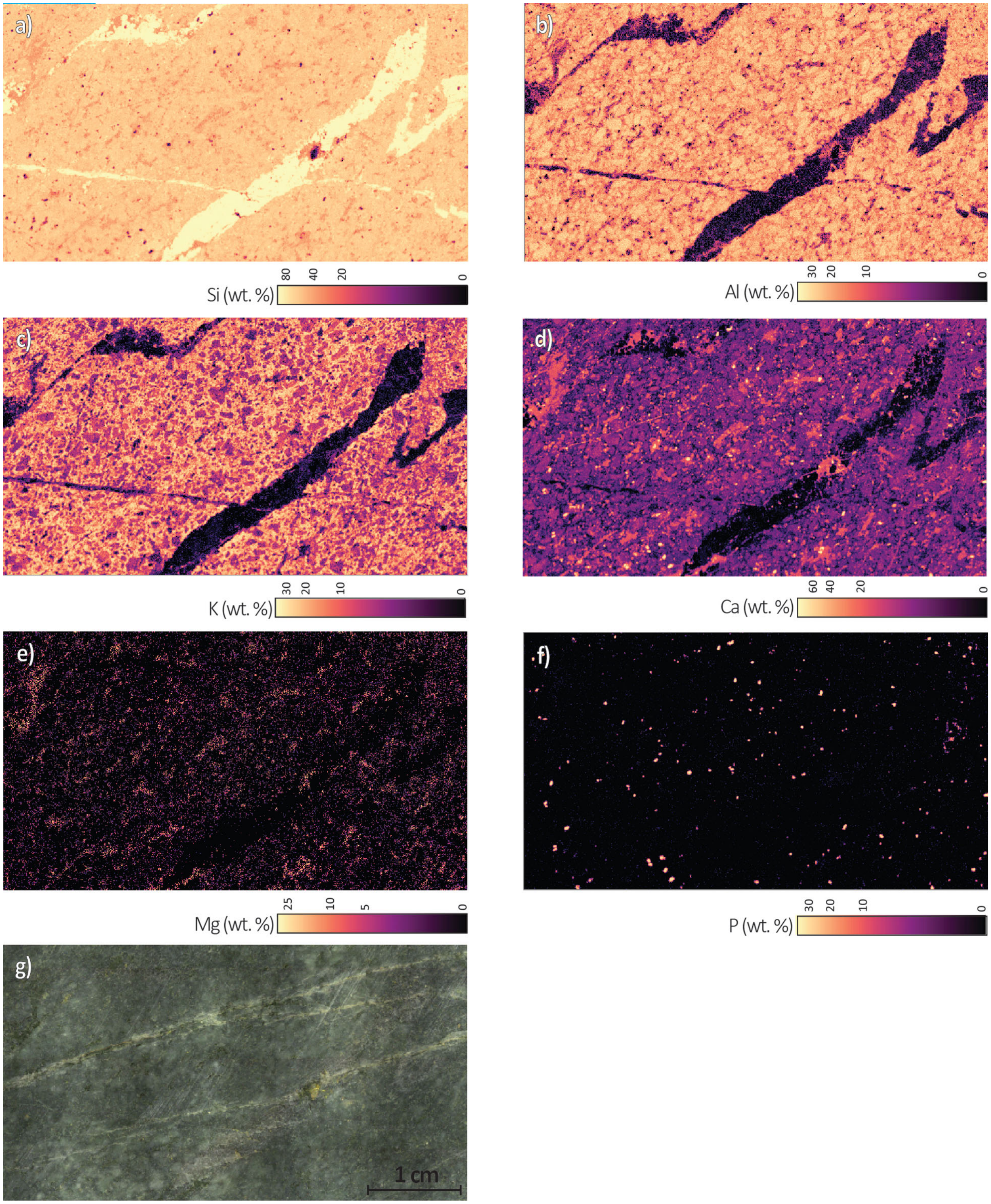

Figure 2. Micro-X-ray–fluorescence images showing quantified concentrations of Si **(a),** Al **(b),** K **(c),** Ca **(d),** Mg **(e)** and P **(f)** in a mineralized Cu-porphyry core sample **(g)** shown in an image captured at 100x magnification by the camera of a Bruker M4 Tornado Plus core scanner. The µXRF chemical maps represent the geochemical variations within a sample, which are controlled by the distribution and composition of minerals in the sample. The Si and Al chemical maps clearly show quartz veins surrounded by an aluminosilicate matrix (Figure 2a, b). The Ca chemical map illustrates several groupings of Ca-bearing minerals in the aluminosilicate matrix (Figure 2d). The highest Ca values overlap with the highest P values (Figure 2f) indicating the presence of apatite {$Ca_5(PO_4)_3(F,Cl,OH)$}; moderate Ca, Mg and Fe values and elongate crystal shapes indicate hornblende {$Ca_2(Mg,Fe,Al)_5(Al,Si)_8O_{22}(OH)_2$} is present; moderate to low Ca values with Al indicate the presence of plagioclase feldspar {$(Na,Ca)Al_2Si_2O_8$}; and very low to no Ca indicates that quartz is present. Additionally, the K elemental map shows the effects of potassic-hydrothermal alteration, associated with the ore zone, where high K values indicate potassic alteration in the aluminosilicate gangue (Figure 2c). Chemical maps were produced using a visualization package in the programming language Python from exported quantified and normalized elemental concentrations determined using the Bruker ESPRIT QMap tool.

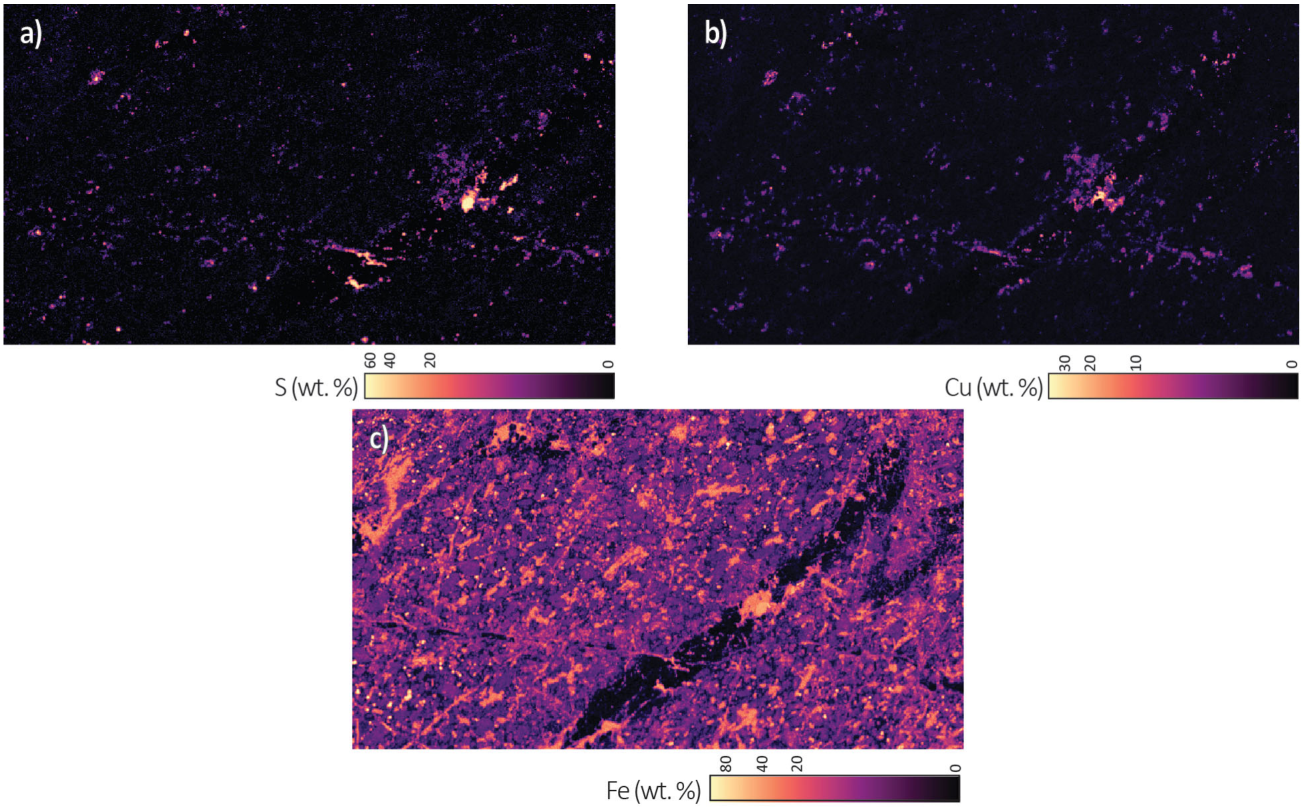

Figure 3. Micro-X-ray–fluorescence images showing quantified concentrations of S **(a)**, Cu **(b)** and Fe **(c)** in a mineralized Cu-porphyry core sample. Copper-ore minerals and sulphide gangue can be readily identified by S, Fe and Cu values on the chemical maps. The high Cu values indicate the presence of chalcopyrite and high Fe and S values, that of pyrite.

aluminosilicate matrix (Figure 2a, b). Similarly, copper-ore minerals and sulphide gangue can be readily identified by S, Cu and Fe values on the chemical maps (Figure 3). The high Cu values indicate the presence of chalcopyrite, and high Fe and S values indicate that of pyrite. In addition to identifying mineralization and vein composition, the chemical maps can be used to visualize the elemental variance across a sample to determine mineralogy and hydrothermal alteration in the quartz-aluminosilicate matrix. For example, the quantified Ca chemical map illustrates several groupings of Ca-bearing minerals (Figure 2d). The highest Ca values overlap with the highest P values (Figure 2f) indicating the presence of apatite {$Ca_5(PO_4)_3(F,Cl,OH)$}; moderate Ca, Mg and Fe values and elongate crystal shapes indicate that hornblende {$Ca_2(Mg,Fe,Al)_5(Al,Si)_8O_{22}(OH)_2$} is present; moderate to low Ca values with Al indicate the presence of plagioclase feldspar {$(Na,Ca)Al_2Si_2O_8$}; and very low to no Ca indicates that quartz is present. In addition to mineralogy, the chemical effects of hydrothermal alteration can be seen on the chemical maps (Figure 2c). High K values in the aluminosilicate matrix illustrate widespread potassic alteration, where K has replaced Ca and Na in the gangue minerals (Figure 2c).

Mineral Maps

The unsupervised clustering algorithm identified six clusters that generally correspond to chalcopyrite, pyrite, hornblende, apatite, quartz and aluminosilicate-quartz matrix (Figure 4). Apatite, chalcopyrite and pyrite were compositionally distinct and easily separated using the clustering algorithm. The clustering algorithm was not as effective when used to separate compositionally similar aluminosilicate mineral groups, such as feldspar and clay.

Discussion

µXRF Chemical Mapping

The benchtop µXRF core scanner and ESPRIT QMap tool used to quantify elemental maps displayed in Python were highly effective in producing informative chemical maps for ore, gangue and indicator minerals. The maps clearly illustrated vein mineralogy and highlighted copper-mineralization distribution across the sample. Quartz veins can be identified by high Si values, whereas copper-ore minerals and pyrite gangue can be readily identified by S, Fe and Cu, and the aluminosilicate matrix can be differentiated by Ca concentration (Figures 2, 3). High P values highlighted apatite grains, a key porphyry-indicator mineral (Bouzari et al., 2016). Hydrothermal alteration is another example of

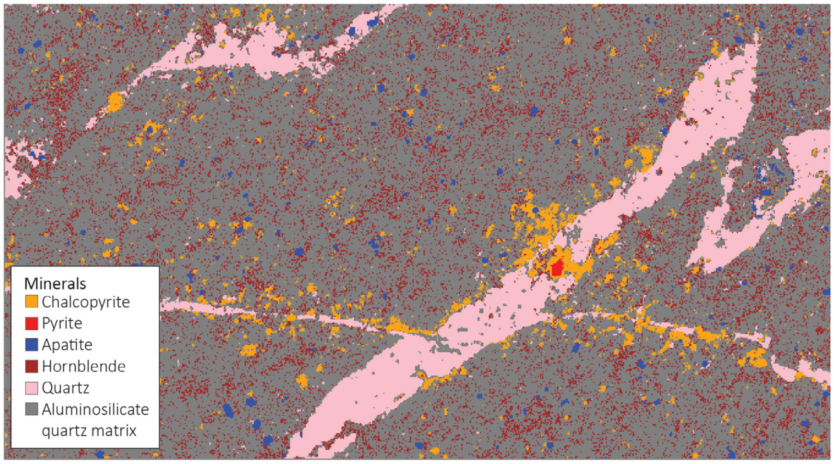

Figure 4. Mineral map of a mineralized Cu-porphyry core sample derived from quantified micro-X-ray–fluorescence chemical maps using unsupervised dimensionality-reduction and clustering methods. The unsupervised clustering algorithm identified six distinct clusters that generally correspond to chalcopyrite, pyrite, apatite, hornblende, quartz and aluminosilicate-quartz matrix. Apatite, chalcopyrite and pyrite were compositionally distinct and easily separated using the clustering algorithm; however, fine pyrite grains may have been underestimated. The clustering algorithm was less effective in separating compositionally similar aluminosilicate mineral groups, such as feldspar and clay. The copper mineralization illustrated on the mineral map is predominantly associated with, or proximal to, quartz veining and the sulphides present are chalcopyrite and pyrite. Apatite, a key Cu-porphyry–indicator mineral, can be readily identified on the mineral map.

µXRF chemical mapping revealing subtle geochemical textures. The µXRF chemical maps of the porphyry core show widespread elevated values of K (Figure 2c) that are interpreted to indicate pervasive potassic alteration with K replacement in aluminosilicates.

µXRF Mineral Identification

In this study, copper mineralization, sulphides, amphibole and apatite were successfully clustered into distinct groupings by the unsupervised clustering method and a user-assigned mineral name from the bulk chemistry of the cluster was given to the cluster. As this work is preliminary, the mineral phases identified require future external validation by scanning electron microscopy and/or X-ray diffraction (XRD). The clustering method applied functions most effectively when determining compositionally distinct minerals such as chalcopyrite, pyrite, apatite and quartz. These groupings were easily separated using the clustering algorithm, although this method failed when used to separate the minerals in the aluminosilicate matrix, such as feldspar, clay and amphibole. Additional work refining and developing the clustering method is required to distinguish between compositionally similar aluminosilicate groups, such as has been achieved using the linear-programming approach adopted by Barker et al (2021). The difficulty in identifying compositionally similar minerals is not unique to µXRF chemical mapping. Compositionally similar minerals, such as aluminosilicates and oxides, pose a challenge to electron-microbeam–derived spectral methods of mineral identification as these minerals are difficult to distinguish one from the other due to the fact their similar spectra reflect similar elemental compositions.

µXRF Technical Challenges

Several technical challenges were identified in this study. Mixed XRF spectra were a potential drawback of the method and posed an additional challenge when it came to identifying minerals using µXRF chemical mapping. The large excitation volume of the electron beam can produce deep multiphase fluorescence and result in horizontal and vertical spectral mixing in nonmonolayered samples (Flude et al., 2017). For example, neighbouring minerals adjacent to, and lying below, the uppermost mineral in a sample may interact with the electron beam and result in mixed spectra. Spectral mixing can result in an apparent range of compositions for a mineral due to the effect of neighbouring minerals diluting the signal from the mineral of interest. Two-phase mixing may be readily quantified, however, three- to four-phase mixing greatly complicates deconvolution of the µXRF spectra when determining quantified mineralogy (Barker et al., 2021). Mixed pixels consisting of spectra from two or more minerals complicated the clustering algorithm's effectiveness in separating mineral groups by composition. This was due to mineral chemical compositions appearing to range from the end-member chemistry of a mineral, derived from unmixed spectra, to a blend of the chemical compositions of two or more minerals, derived from mixed spectra. The apparent range of mineral compositions that blended into one another reduced the effectiveness of the clustering algorithm to distinguish between separate, distinct mineral groups.

µXRF Geoscience and Exploration Applications

Micro-X-ray–fluorescence techniques provide a nondestructive method that can be used for the analysis of major and trace elements; furthermore, these techniques present a wide range of opportunities for applications in the geosciences and mineral exploration (Croudace et al., 2019). Benchtop µXRF core scanners allow for relatively rapid quantitative chemical analysis over a large mapping area, in comparison with other automated mineralogy methods, and can provide key geochemical information at the scale of tens of microns (Flude et al., 2017). For example, µXRF chemical maps can be used to identify mineralogical and compositional variation in veins, provide information on trace precious metals in ores and deleterious elemental distributions in tailings (Fawcett and Jamieson, 2011; Ryan et al., 2018; Barker et al., 2021). Additionally, mineral identification can be derived from µXRF spectra and has widespread potential to aid in DIM exploration programs. Mineral mapping using µXRF results in faster and cheaper analysis requiring less sample-preparation time when compared to automated SEM analyses. However, a consequence of this approach is that the data interpretation becomes more complicated due to the effects of mixed spectra and the difficulty distinguishing between compositionally similar minerals. Machine-learning methods offer opportunities to address the challenges associated with µXRF-data interpretation (Barker et al., 2021; Kim et al., 2022). The preliminary results show that the unsupervised ML methods applied in this study identified key copper ore, gangue and indicator minerals, but were less effective when it came to separating compositionally similar minerals or mixed spectra, thus requiring user input to link clusters to mineral groups. Supervised ML methods can potentially lead to the successful classification of complicated µXRF data as the algorithms can be trained to identify mixed signals and integrate additional datasets, such as those obtained from XRD, optical images or microscopy (Barker et al., 2021; Kim et al., 2022).

Conclusion

The aims of this research are to develop µXRF mineral-identification methods designed to improve, quantify and expedite the identification of Cu-porphyry–related ore, gangue and indicator minerals. The project will contribute to the development of industry-applicable, cost-effective quantitative mineral-identification methods. The preliminary study investigated mineral-identification methods on a piece of mineralized Cu-porphyry core using µXRF chemical mapping and unsupervised ML methods. The unsupervised mineral-identification methods identified copper mineralization, sulphides and porphyry-indicator minerals, including chalcopyrite and apatite. Compositionally similar minerals, such as aluminosilicates, were not readily identified using the clustering method. These preliminary results show the unsupervised ML methods were successful in identifying copper ore and DIMs. Further work is required to validate the µXRF fundamental-parameters standardless quantification of Cu-porphyry minerals and to externally validate the minerals identified by SEM and/or XRD analysis using the clustering algorithm. Future work will apply µXRF chemical mapping and unsupervised ML classification methods to DIMs.

Acknowledgments

The authors thank Geoscience BC, the Society of Economic Geologists and the Mineral Deposits Research Unit of The University of British Columbia for their financial support of this project. The authors would also like to thank J. Saylor for his input and review of the manuscript.

References

Barker, R.D., Barker, S.L.L., Wilson, S.A. and Stock, E.D. (2021): Quantitative mineral mapping of drill core surfaces I: a method for µXRF mineral calculation and mapping of hydrothermally altered, fine-grained sedimentary rocks from a Carlin-type gold deposit; Economic Geology, v. 116, no. 4, p. 803–819, URL <https://doi.org/10.5382/ECONGEO.4803>.

Bouzari, F., Hart, C.J.R., Bissig, T. and Barker, S. (2016): Hydrothermal alteration revealed by apatite luminescence and chemistry; a potential indicator mineral for exploring covered porphyry copper deposits; Economic Geology, v. 111, no. 6, p. 1397–1410, URL <https://doi.org/10.2113/econgeo.111.6.1397>.

Ciacci, L., Fishman, T., Elshkaki, A., Graedel, T.E., Vassura, I. and Passarini, F. (2020): Exploring future copper demand, recycling and associated greenhouse gas emissions in the EU-28; Global Environmental Change, v. 63, art. 102093, URL <https://doi.org/10.1016/J.GLOENVCHA.2020.102093>.

Cooke, D.R., Wilkinson, J.J., Baker, M., Agnew, P., Phillips, J., Chang, Z., Chen, H., Wilkinson, C.C., Inglis, S., Hollings, P., Zhang, L., Gemmell, J.B., White, N.C., Danyushevsky, L. and Martin, H. (2020): Using mineral chemistry to aid exploration: a case study from the Resolution porphyry Cu-Mo deposit, Arizona; Economic Geology, v. 115, no. 4, p. 813–840, URL <https://doi.org/10.5382/econgeo.4735>.

Croudace, I.W., Löwemark, L., Tjallingii, R. and Zolitschka, B. (2019): Current perspectives on the capabilities of high resolution XRF core scanners; Quaternary International, v. 514, p. 5–15, URL <https://doi.org/10.1016/j.quaint.2019.04.002>.

Elshkaki, A., Graedel, T.E., Ciacci, L. and Reck, B.K. (2016): Copper demand, supply, and associated energy use to 2050; Global Environmental Change, v. 39, p. 305–315, URL <https://doi.org/10.1016/J.GLOENVCHA.2016.06.006>.

Eppinger, R.G., Fey, D.L., Giles, S.A., Grunsky, E.C., Kelley, K.D., Minsley, B.J., Munk, L. and Smith, S.M. (2013): Summary of exploration geochemical and mineralogical studies at the Giant Pebble porphyry Cu-Au-Mo deposit, Alaska:

implications for exploration under cover; Economic Geology, v. 108, no. 3, p. 495–527, URL <https://doi.org/10.2113/econgeo.108.3.495>.

Fawcett, S.E. and Jamieson, H.E. (2011): The distinction between ore processing and post-depositional transformation on the speciation of arsenic and antimony in mine waste and sediment; Chemical Geology, v. 283, no. 3, p. 109–118, URL <https://doi.org/10.1016/j.chemgeo.2010.02.019>.

Flude, S., Haschke, M. and Storey, M. (2017): Application of benchtop micro-XRF to geological materials; Mineralogical Magazine, v. 81, no. 4, p. 923–948, URL <https://doi.org/10.1180/minmag.2016.080.150>.

Galloway, J.M., Swindles, G.T., Jamieson, H.E., Palmer, M., Parsons, M.B., Sanei, H., Macumber, A.L., Patterson, R.T. and Falck, H. (2018): Organic matter control on the distribution of arsenic in lake sediments impacted by ∼∼65 years of gold ore processing in subarctic Canada; Science of The Total Environment, v. 622–623, p. 1668–1679, URL <https://doi.org/10.1016/j.scitotenv.2017.10.048>.

Gent, M., Menendez, M., Toraño, J. and Torno, S. (2011): A review of indicator minerals and sample processing methods for geochemical exploration; Journal of Geochemical Exploration, v. 110, no. 2, p. 47–60, URL <https://doi.org/10.1016/j.gexplo.2011.05.005>.

Gonzalez-Alvarez, I., Goncalves, M.A. and Carranza, E.J.M. (2020): Introduction to the Special Issue Challenges for mineral exploration in the 21st century: targeting mineral deposits under cover; Ore Geology Reviews, v. 126, art. 103785, URL <https://doi.org/10.1016/j.oregeorev.2020.103785>.

Gottlieb, P., Wilkie, G., Sutherland, D., Ho-Tun, E., Suthers, S., Perera, K., Jenkins, B., Spencer, S., Butcher, A. and Rayner, J. (2000): Using quantitative electron microscopy for process mineralogy applications; Journal of the Minerals, Metals and Materials Society, v. 52, no. 4, p. 24–25, URL <https://doi.org/10.1007/s11837-000-0126-9>.

Hennekam, R., Sweere, T., Tjallingii, R., de Lange, G. J. and Reichart, G.-J. (2019): Trace metal analysis of sediment cores using a novel X-ray fluorescence core scanning method; Quaternary International, v. 514, p. 55–67, URL <https://doi.org/10.1016/j.quaint.2018.10.018>.

Hussain, M., Amao, A.O., Al-Ramadan, K., Babalola, L.O. and Humphrey, J.D. (2022): Unconventional reservoir characterization using geochemical signatures: examples from Paleozoic formations, Saudi Arabia; Marine and Petroleum Geology, v. 143, art. 105770, URL <https://doi.org/10.1016/j.marpetgeo.2022.105770>.

Hussain, M., Amao, A.J., Jin, G. and Al-Ramadan, K. (2018): Linking geochemical and mechanical properties of rock samples using new non-destructive techniques; Kingdom of Saudi Arabia Annual Technical Symposium and Exhibition, Society of Petroleum Engineers, April 23–26, 2018, Dammam, Saudi Arabia, Paper no. SPE-192347-SPE, URL <https://doi.org/10.2118/192347-MS>.

Jansen, J.H.F., Van der Gaast, S.J., Koster, B. and Vaars, A.J. (1998): CORTEX, a shipboard XRF-scanner for element analyses in split sediment cores; Marine Geology, v. 151, no. 1, p. 143–153, URL <https://doi.org/10.1016/S0025-3227(98)00074-7>.

Jooshaki, M., Nad, A. and Michaux, S. (2021): A systematic review on the application of machine learning in exploiting mineralogical data in mining and mineral industry; Minerals, v. 11, no. 8, p. 816, URL <https://doi.org/10.3390/min11080816>.

Jordan, M.I. and Mitchell, T.M. (2015): Machine learning: trends, perspectives, and prospects; Science, v. 349, no. 6245, p. 255–260, URL <https://doi.org/10.1126/science.aaa8415>.

Kanngieβer, B. (2003): Quantification procedures in micro X-ray fluorescence analysis; Spectrochimica Acta Part B: Atomic Spectroscopy, v. 58, no. 4, p. 609–614, URL <https://doi.org/10.1016/S0584-8547(02)00281-1>.

Kim, J.J., Ling, F.T., Plattenberger, D.A., Clarens, A.F. and Peters, C.A. (2022): Quantification of mineral reactivity using machine learning interpretation of micro-XRF data; Applied Geochemistry, v. 136, art. 105162, URL <https://doi.org/10.1016/j.apgeochem.2021.105162>.

Lougheed, H.D., McClenaghan, M.B., Layton-Matthews, D. and Leybourne, M. (2020): Exploration potential of fine-fraction heavy mineral concentrates from till using automated mineralogy: a case study from the Izok Lake Cu–Zn–Pb–Ag VMS deposit, Nunavut, Canada; Minerals, v. 10, no. 4, p. 1–33, URL <https://doi.org/10.3390/min10040310>.

McClenaghan, M.B. (2005): Indicator mineral methods in mineral exploration; Geochemistry: Exploration, Environment, Analysis, v. 5, no. 3, p. 233–245, URL <https://doi.org/10.1144/1467-7873/03-066>.

McClenaghan, M.B. and Layton-Matthews, D. (2017): Application of indicator mineral methods to bedrock and sediments; Exploration ‘17: Sixth Decennial International Conference on Mineral Exploration, October 22–25, 2017, Toronto, Ontario; Geological Survey of Canada, Open File 8345, 86 p., URL <https://doi.org/10.4095/306305>.

McClenaghan, M.B., Thorleifson, L.H. and Dilabio, R.N.W. (2000): Till geochemical and indicator mineral methods in mineral exploration; Ore Geology Reviews, v. 16, no. 3–4, p. 145–166, URL <https://doi.org/10.1016/S0169-1368(99)00028-1>.

Peti, L., Augustinus, P.C., Gadd, P.S. and Davies, S.J. (2019): Towards characterising rhyolitic tephra layers from New Zealand with rapid, non-destructive μ-XRF core scanning; Quaternary International, v. 514, p. 161–172, URL <https://doi.org/10.1016/j.quaint.2018.06.039>.

Plouffe, A., Ferbey, T., Hashmi, S. and Ward, B.C. (2016): Till geochemistry and mineralogy: vectoring towards Cu porphyry deposits in British Columbia, Canada; Geochemistry: Exploration, Environment, Analysis, v. 16, no. 3–4, p. 213–232, URL <https://doi.org/10.1144/GEOCHEM2015-398>.

Ryan, C.G., Kirkham, R., Moorhead, G.F., Parry, D., Jensen, M., Faulks, A., Hogan, S., Dunn, P.A., Dodanwela, R., Fisher, L.A., Pearce, M., Siddons, D.P., Kuczewski, A., Lundström, U., Trolliet, A. and Gao, N. (2018): Maia Mapper: high definition XRF imaging in the lab; Journal of Instrumentation, v. 13, no. 03, art. C03020, 8 p., URL <https://doi.org/10.1088/1748-0221/13/03/C03020>.

Schulz, B., Sandmann, D. and Gilbricht, S. (2020): SEM-based automated mineralogy and its application in geo- and material sciences; Minerals, v. 10, no. 11, art. 1004, URL <https://doi.org/10.3390/min10111004>.

Sillitoe, R.H. (2010): Porphyry copper systems; Economic Geology, v. 105, no. 1, p. 3–41, URL <https://doi.org/10.2113/gsecongeo.105.1.3>.

Sylvester, P. (2012): Use of the Mineral Liberation Analyzer (MLA) for mineralogical studies of sediments and sedimentary rocks; Mineralogical Association of Canada, Mineralogical Association of Canada Short Course Series, v. 42, p. 1–16.

Characterizing Reactivity of Ultramafic Minerals and Tailings in British Columbia for Carbon Capture and Storage

X. Lu[1], **The University of British Columbia, Vancouver, British Columbia, xlu@eoas.ubc.ca**

X. Wang, Tsinghua University, Beijing, China

G.M. Dipple, The University of British Columbia, Vancouver, British Columbia

X. Lu, X. Wang and G.M. Dipple (2023): Characterizing reactivity of ultramafic minerals and tailings in British Columbia for carbon capture and storage; *in* Geoscience BC Summary of Activities 2022: Minerals, Geoscience BC, Report 2023-01, p. 45–54.

Introduction

Climate change and rising atmospheric carbon dioxide (CO_2) levels have recently become much-debated environmental issues. One of the strategies necessary to mitigate climate change is capturing, utilizing and storing greenhouse gases such as CO_2 (Bickle, 2009). Carbon sequestration via mineral carbonation (also known as carbon mineralization) has emerged as a promising strategy to reduce net greenhouse gas emissions (Seifritz, 1990; Lackner et al., 1995; Lackner, 2003; Sipilä et al., 2008). Industrial waste materials like mine tailings are high in reactive surface area because of the crushing and grinding during mineral processing and, thus, are ideal for carbon mineralization (Uddin et al., 2012). Different tailings materials will have various sequestration capacities. Specifically, waste from mines hosted in ultramafic rocks that contain commodities such as asbestos, diamond, chromite and nickel have the highest predicted carbon sequestration capacity due to the presence of fast-reacting trace minerals such as brucite (Wilson et al., 2009, 2010, 2011; Power et al., 2011; Pronost et al., 2011; Bea et al., 2012; Harrison et al., 2013; Rozalen et al., 2014; Hamilton et al., 2020). Currently, many ultramafic mine sites around the world, such as the Mount Keith nickel mine in Western Australia and the Diavik Diamond Mine in the Northwest Territories, Canada, have documented their tailings naturally reacting with atmospheric CO_2 (Wilson et al., 2011, 2014). The province of British Columbia (BC) also represents massive carbon-capturing potential, as the area contains extensive volumes of ultramafic rock that host some of Canada's largest nickel deposits. The extraction and crushing of such rocks during mining will unlock their reactivity for ex-situ carbon mineralization.

The geochemical process of mineral carbonation in mine tailings involves incorporating CO_2 gas into inert carbonate minerals ($MgCO_3 \cdot xH_2O$) through the aqueous reaction of 1) the dissolution of CO_2 into the water, producing acidity; 2) leaching of cations from the surrounding minerals; and 3) the precipitation of Mg-carbonate minerals, consuming alkalinity, as described in Equations 1 to 3, where (g) refers to gaseous phases, (l) refers to liquid phases, and (aq) refers to aqueous phases.

$$2CO_2(g) + 2H_2O(l) \leftrightarrow 2H_2CO_3(aq) \rightarrow 2HCO_3^-(aq) + 2H^+(aq) \quad (1)$$

$$Mg(OH)_2 + 2H^+ \rightarrow Mg^{2+} + 2H_2O \quad (2)$$

$$Mg^{2+} + 2HCO_3^- + 2H_2O \rightarrow MgCO_3 \cdot 3H_2O + CO_2(g) \quad (3)$$

The current feasibility studies that are used to synthesize the capacity of mine tailings for carbon sequestration at an industrial scale include lab-scale, pilot, and field-scale testing (McGrail et al., 2003, 2006; Matter and Kelemen, 2009; Haug et al., 2011; Beerling et al., 2018; Power et al., 2021). In particular, lab-scale testing is used to study the carbon sequestration potential or the reactivity of minerals and tailings. Reaction rate and time are two dominating factors controlling mineral carbonation reactivity (Knauss and Wolery, 1988; Berg and Banwart, 2000; Pokrovsky and Schott, 2004; Harrison et al., 2013; Power et al., 2013a, b; Thom et al., 2013; Li et al., 2018; Bullock et al., 2021). Previous studies on mineral dissolution kinetics have shown that not all cations are accessible under atmospheric conditions (Snæbjörnsdóttir et al., 2018; Tutolo and Tosca, 2018; Wolff-Boenisch and Galeczka, 2018; Paulo et al., 2021). Hence, this paper uses labile Mg^{2+} (defined as Mg^{2+} that is accessible and can be rapidly leached at ambient pressure and temperature) to quantify carbon sequestration reactivity in ultramafic rocks.

Mineral dissolution in a flow-through reactor (flow-through time-resolved analysis [FT-TRA] module) was used to characterize the loosely bound, fast-reacting labile Mg^{2+} and slow-reacting non-labile Mg^{2+} (De Baere et al., 2015; Lu et al., 2022). Results show that the amount of labile Mg^{2+} is primarily controlled by the reaction rate of the mineral and time in the flow-through reactor. In other words, the amount of accessible labile Mg^{2+} will depend on the characteristics of a carbon sequestration site, particu-

[1]*The lead author is a 2022 Geoscience BC Scholarship recipient.*

This publication is also available, free of charge, as colour digital files in Adobe Acrobat® PDF format from the Geoscience BC website: http://geosciencebc.com/updates/summary-of-activities/.

larly the length of time that the cation feedstock is exposed and can dissolve and react with CO_2 to form carbonate minerals. The lab-scale test also demonstrates that all Mg^{2+} in Mg-hydroxide minerals are labile due to their high reactivity, whereas Mg-silicate minerals contribute less due to their slow dissolution kinetics. Nonetheless, Mg-silicate minerals have the highest abundance in ultramafic rocks and, thus, represent the most significant potential source of labile Mg^{2+} for mineral carbonation.

Although the flow-through dissolution experiment has successfully characterized labile Mg^{2+}, the FT-TRA module can be challenging to set up and operate (De Baere et al., 2015). Alternative experiment protocols that are easier to operate, faster and low-cost are sought for more efficient evaluation. In this study, an air carbonation test is adopted to characterize reactivity by quantifying labile Mg^{2+} carbonation. The air carbonation method treats samples under humidified CO_2 gas in a closed chamber and monitors the increase in total inorganic carbon content. Samples of typical ultramafic minerals and tailings were acquired to test the method. The air carbonation experiment is conducted with an orthogonal design to rank various factors influencing labile Mg^{2+} carbonation (Zurovac and Brown, 2012; Wu, 2013; Zhang and Ma, 2013). The details of the orthogonal experimental design and data analysis are discussed below. Overall, the air carbonation test will be evaluated as a low-cost and labour-efficient option for assessing the mineral carbonation reactivity of minerals and tailings. The results from this study will impart a better understanding of the fundamental mechanisms and chemical processes that control heterogeneity and reactivity, with implications for mineral carbonation in other processed industrial wastes, such as asbestos mine tailings, red mud and steel slag. More importantly, this research serves as a foundation to develop characterization protocols to assist CO_2 capture and storage using mine tailings in BC, and may take BC to the forefront globally in the development of carbon capture, utilization and storage.

Materials and Methods

Sample Material

Three mineral samples (brucite, serpentine and forsterite) were used to prepare samples for the air carbonation test: high-purity pulverized brucite ore was sourced from the Brucite mine (Gabbs District, Nevada, United States); serpentine samples were obtained from the Swift Creek landslide in the northwestern part of the State of Washington, United States; and forsterite grains from the Twin Sisters dunite, also in Washington, were supplied by Ward's Science (item# 470025-722).

The samples were dry-milled and dry-screened to the following particle size ranges: <53 µm, 53–106 µm, and >106 µm. All samples were characterized for their mineralogical composition (using quantitative X-ray diffraction), thermal stability and fraction of volatile components (using thermogravimetric analysis [TGA]), specific surface area (using the multi-point Brunauer-Emmett-Teller [BET] method with N_2 gas absorption), and particle size distribution (using a Malvern Panalytical Mastersizer 2000 laser diffraction particle-size analyzer). Brucite abundance in the mineral samples is taken from values measured using TGA, since quantitative X-ray diffraction (qXRD) analyses often result in a high relative error for minerals at low abundance (Raudsepp et al., 1999; Washbourne et al., 2012; Tosca and Masterson, 2014; Arce et al., 2017; Turvey et al., 2018a, b, 2022). The relevant sample characterization results are summarized in Table 1.

Orthogonal Experimental Design

Orthogonal experimental design (OED) is a method of scientific testing that studies multiple factors simultaneously, and their impact level, to determine the optimal combination of factors (Zurovac and Brown, 2012; Wu, 2013). Orthogonality refers to the property of a design that ensures all the specific parameters may be estimated independently of one another. Orthogonal experimental design is often used for this purpose, because the design can effectively reduce the number of experiments needed. Variance analysis and regression analysis are commonly used to analyze the results from OED tests, and can lead to many valuable conclusions (Zhang and Ma, 2013). Thus, OED is used in this study to allow testing of multiple variables that can affect mineral carbonation reactivity of minerals and tailings.

The orthogonal table is the foundation of the orthogonal experimental design, which is formed according to the following definition:

$L_n(m)^k$,

where L is the table, n is the number of rows (which corresponds to the number of test cases), m is the number of col-

Table 1. Summary of relevant quantitative X-ray diffraction (qXRD) mineral abundances, thermogravimetric analyses (TGA), brucite abundance, and Brunauer-Emmett-Teller (BET) surface area values for the three mineral samples tested.

Sample name	Brucite	Serpentine (lizardite)	Forsterite
Serpentine[1]		91.9	
Brucite[2]	90.0		
Diopside[1]			
Pyroaurite[2]	0.2		
Forsterite[1]			94.9
Magnesite[1]	0.5		
Phlogopite[1]		3.6	
BET surface area[3]	4.2	18.5	0.2

[1]wt. % abundance determined by qXRD
[2]wt. % abundance determined by TGA
[3]BET (m^2/g)

umns (which corresponds to the number of factors), and k is the factor level number, meaning each factor has k levels. Earlier studies investigated the controls of mineral carbonation in column experiments, and identified that water content and grain size have effects on the progress of the mineral carbonation reaction (Harrison et al., 2015, 2016). Since both brucite and Mg-silicate minerals (e.g., serpentine, olivine) were identified as important sources of reactivity, their mineralogical content may also have an impact on the carbonation process (Lu et al., 2022). Four factors that could impact labile Mg^{2+} carbonation reaction were identified for this study: 1) water content, 2) grain size, 3) brucite content, and 4) silicate mineralogy (serpentine and olivine [forsterite] content). Each of these four factors were tested at three levels (Wu, 2013). Hence, for a test of four factors and three levels, the number of independent test cases was nine, and the orthogonal table formed is defined by the expression $L_9(4^3)$, as shown in Table 2.

The three levels of water content selected for testing were 7.5 wt. % (of the sample mass), 12 wt. % and 15 wt. %. The three levels of grain size tested were >106 µm, 53–106 µm, and <53 µm. The three levels of brucite content tested were 4 wt. % (of the sample mass), 7 wt. % and 10 wt. %. The presence of forsterite and serpentine in the samples was tested by samples with forsterite only, samples with half forsterite and half serpentine, and samples with serpentine only. In this way, the combination of each line in Table 2 constitutes a test case.

Air Carbonation Tests

The set-up of the air carbonation test included a 60 L polycarbonate reaction chamber with inlet and outlet ports for gas flow, and two 4 L interconnected conical flasks (Figure 1). Compressed 10% CO_2 gas was continuously injected into the reaction chamber, using Saint-Gobain Tygon™ R-3603 tubing, at approximately 200 millilitres per minute (ml/min). Carbon dioxide gas was humidified by flowing through the two interconnected 4 L conical flasks containing distilled water. Pulp samples of the minerals were moulded into the shape of disks with dimensions of 17.9 mm radius and 1.8 mm thickness, using a premade Perspex® glass mount and rod piston. Nine test cases representing separate combinations of the four factors were then carried out. In addition, ten subsamples of the nine test cases were made for sampling purposes, and these were taken out of the air carbonation set-up after 4, 20 and 44 days of the experiment. The temperature and humidity in the reaction chamber were stable throughout the experiment, at around 22 ±1ºC and 95 ±0.2% relative humidity. Before and after the air carbonation experiments, samples were homogenized using a corundum mortar pestle and analyzed for total inorganic carbon (TIC). The content of TIC (reported as %C [grams of carbon/grams of the sample]) in the disk samples was determined using a UIC Inc. CM5130 acidification module, and the instrument was calibrated before each analysis. The carbon content in the raw sample was subtracted from the carbon content measured post–carbonation reaction, to obtain the net carbon content gained from carbonation.

Results and Discussion

Hydromagnesite [$Mg_5(CO_3)_4(OH)_2 \cdot 4H_2O$] with the stoichiometry of C/Mg = 0.8 is assumed to form from labile Mg^{2+} carbonation (Wilson et al., 2009; McCutcheon et al., 2019). Data representing TIC (g of carbon/g of the sample) is converted to grams of Mg^{2+} carbonated/grams of the sample for data analysis. The results from 4, 20 and 44 days in the experimental set-up are summarized in Table 3 and shown in Figure 2. In Figure 2, the four factors tested (A, water content; B, grain size; C, brucite content; D, silicate mineralogy) and their three levels (e.g., A1, A2, A3) are plotted on the x-axis, and the amount of Mg^{2+} carbonated is plotted on the y-axis. Data plotted in red, green and black indicate the amount of Mg^{2+} carbonated after 4 days, 20 days and 44 days, respectively, of reaction. Due to the orthogonal nature of the experimental design, the various

Table 2. The orthogonal table defined by the expression $L_9(4^3)$. The table has nine rows, representing nine test cases (i.e., nine different combinations), and the following four factors: A, water content; B, grain size; C, brucite content; D, silicate mineralogy (serpentine and olivine [forsterite] content). Each factor has three levels of variability. For factor A these levels are 7.5, 12 and 15 wt. % water; for B they are >106, 53–106 and <53 µm grain size; for C they are 4, 7 and 10 wt. % brucite; and for D the three levels are samples of forsterite only, samples of half forsterite and half serpentine, and samples of serpentine only.

Test case no.	A Water content (wt. %)	B Grain size (µm)	C Brucite content (wt. %)	D Silicate mineralogy
1	7.5	>106	4	Forsterite
2	7.5	53–106	7	Serpentine
3	7.5	<53	10	Forsterite + serpentine
4	12.0	>106	7	Forsterite + serpentine
5	12.0	53–106	10	Forsterite
6	12.0	<53	4	Serpentine
7	15.0	>106	10	Serpentine
8	15.0	53–106	4	Forsterite + serpentine
9	15.0	<53	7	Forsterite

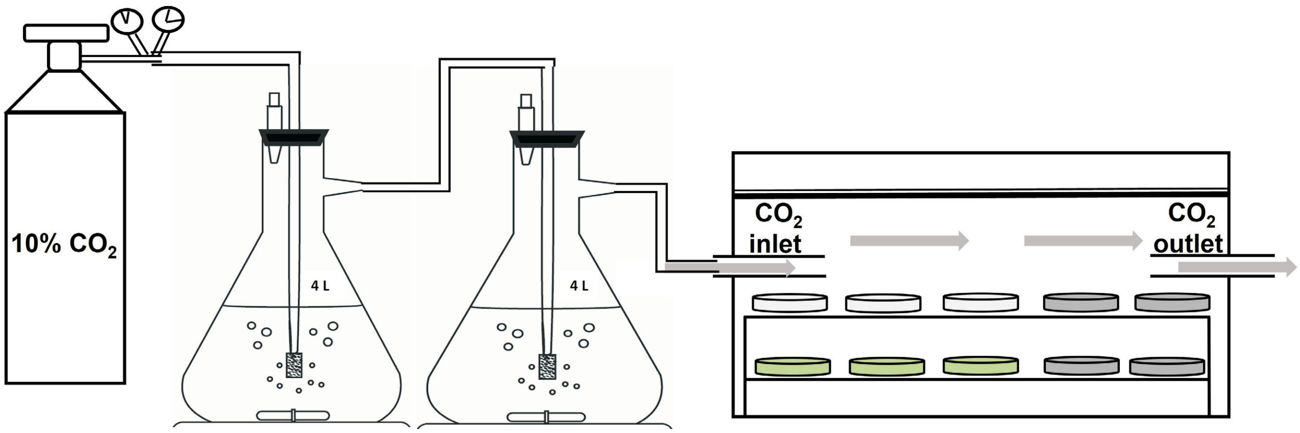

Figure 1. Schematic diagram of the air carbonation experimental set-up. As shown, 10% carbon dioxide (CO_2) gas is continuously injected into two 4 L interconnected conical flasks and then into the reaction chamber for the purpose of humidifying the gas. The colour of the disks represents samples with different mineralogy: green represents serpentine-dominated samples; grey represents forsterite-dominated samples; and white represents samples containing an equal amount of forsterite and serpentine.

levels of each factor are collocation balanced, meaning that all factors are equally tested. Since there are three levels tested, each factor is repeated three times, and the average of the results was determined for variance calculation and to reduce the test error (Table 3, Figure 3).

Variance analysis was used to analyze the impact of various factors on the net carbon gain, and to determine the optimal level of each factor. To find the variance of each factor, the average of each level within each factor is calculated, as shown in Figure 3. Next, the average is subtracted from each level and the differences are squared. The variance of each factor is determined by calculating the average of the squared differences from each level. Equation 4 shows the calculation of variance, where $\bar{x}$ is the mean of the levels, and n is the number of levels. The calculated variances for each factor are presented in Table 3.

$$Variance = \frac{\Sigma(x-\bar{x})^2}{n} \quad (4)$$

In the following sections, the effect of water content, brucite content, silicate mineralogy (serpentine and olivine [forsterite] content), and grain size on labile Mg^{2+} carbonation are discussed.

Table 3. Variance analysis of the orthogonal experiment. Grams of Mg^{2+} carbonated per gram of sample measured from day 4, day 20 and day 44 of the experiment are organized by the four factors tested: A, water content; B, grain size; C, brucite content; D, silicate mineralogy (serpentine and olivine [forsterite] content). Three levels were tested for each factor. For factor A these were 7.5, 12 and 15 wt. %; for B, >106, 53–106 and <53 µm; for C, 4, 7 and 10 wt. %; and for D, samples of forsterite only, samples of half forsterite and half serpentine, and samples of serpentine only.

	A		B		C		D	
	Water content (wt. %)	g Mg^{2+} / g sample	Grain size (µm)	g Mg^{2+} / g sample	Brucite content (wt. %)	g Mg^{2+} / g sample	Silicate mineralogy	g Mg^{2+} / g sample
44 days								
1	7.5	1.08	>106	1.17	4	0.67	Forsterite	0.91
2	12	1.02	53–106	1.05	7	1.07	Forsterite +serpentine	1.13
3	15	1.17	<53	1.06	10	1.54	Serpentine	1.24
Variance		0.01		0.01		0.19		0.03
20 days								
1	7.5	0.56	>106	0.76	4	0.39	Forsterite	0.59
2	12	0.67	53–106	0.67	7	0.65	Forsterite +serpentine	0.67
3	15	0.82	<53	0.62	10	1.01	Serpentine	0.79
Variance		0.02		0.01		0.10		0.01
4 days								
1	7.5	0.18	>106	0.39	4	0.17	Forsterite	0.28
2	12	0.3	53–106	0.33	7	0.26	Forsterite +serpentine	0.23
3	15	0.45	<53	0.21	10	0.51	Serpentine	0.42
Variance		0.02		0.01		0.03		0.01

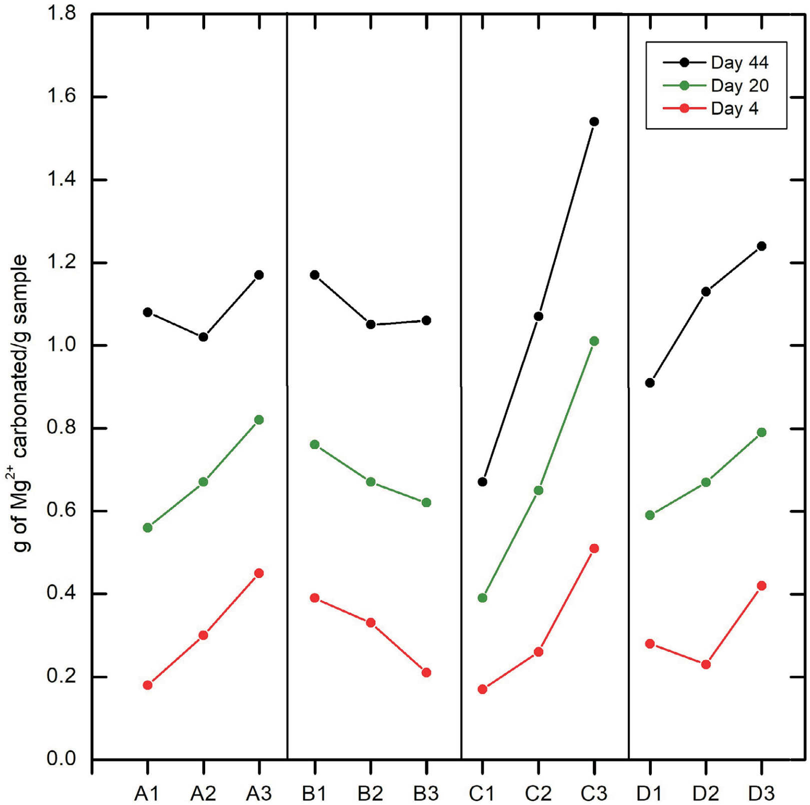

Figure 2. Plot of grams of Mg^{2+} carbonated per gram of sample versus the factors and levels tested. The x-axis shows the four factors tested (A, water content; B, grain size; C, brucite content; D, silicate mineralogy). For factor A, the three levels used were 7.5 (A1), 12 (A2) and 15 wt. % (A3); for B, >106 (B1), 53–106 (B2) and <53 µm (B3); for C, 4 (C1), 7 (C2) and 10 wt. % (C3); and for D, samples of forsterite only (D1), samples of half forsterite and half serpentine (D2), and samples of serpentine only (D3). The values of the plotted data points are also presented in Table 3. Data plotted in red, green and black represent the progression of Mg^{2+} carbonated after 4, 20 and 44 days, respectively, in the air carbonation set-up.

Effect of Water Content and Brucite Content

Three levels of moisture (water) content (7.5, 12 and 15 wt. %) and brucite content (4, 7 and 10 wt. %) were tested. As shown in Figure 2 and Table 3, the amount of Mg^{2+} carbonated is consistently higher in samples with 15 wt. % water and 10 wt. % brucite, followed by samples with 12 wt. % water, 7 wt. % brucite, and then 7.5 wt. % water, 4 wt. % brucite. The data also show a significant increase in the amount of Mg^{2+} carbonated from day 4 to day 44, which demonstrates the progress in reaction with time. Samples with the highest moisture and brucite content had the highest carbonated Mg^{2+}, demonstrating that the mineral carbonation reactivity is greater for high brucite content and moist tailings. The variances calculated in Table 3 also show that water content has lower effects on carbonation reaction during the later stages, because the reaction may become limited by the surface passivation effect and the supply of CO_2 and leachable Mg^{2+}. These findings agree with previous studies using metre-scale column experiments and reactive transport modelling (Harrison et al., 2015, 2017). However, the air carbonation test is much easier to set up and manage.

Effect of Silicate Mineralogy and Grain Size

Samples with different serpentine and forsterite content behaved differently in the air carbonation experiment and yielded interesting results. As shown in Figure 2, the sample with only forsterite consistently reacted less than samples with serpentine. Overall, samples with only serpentine carbonated the highest amount of labile Mg^{2+}. This finding and observation agree with what was observed in the previous flow-through study (Lu et al., 2022), which is that serpentine has more labile Mg^{2+} than olivine because of the larger surface area and the longer, faster transient dissolution stage. Thus, after 44 days, samples with the highest content of serpentine carbonated the most Mg^{2+}. Moreover, the grain-size test results demonstrated that samples with the largest grain size, i.e., the largest pore space, have the highest reactivity. This agrees with the reactivity expectation of tailings based on their grain size reduction during pro-

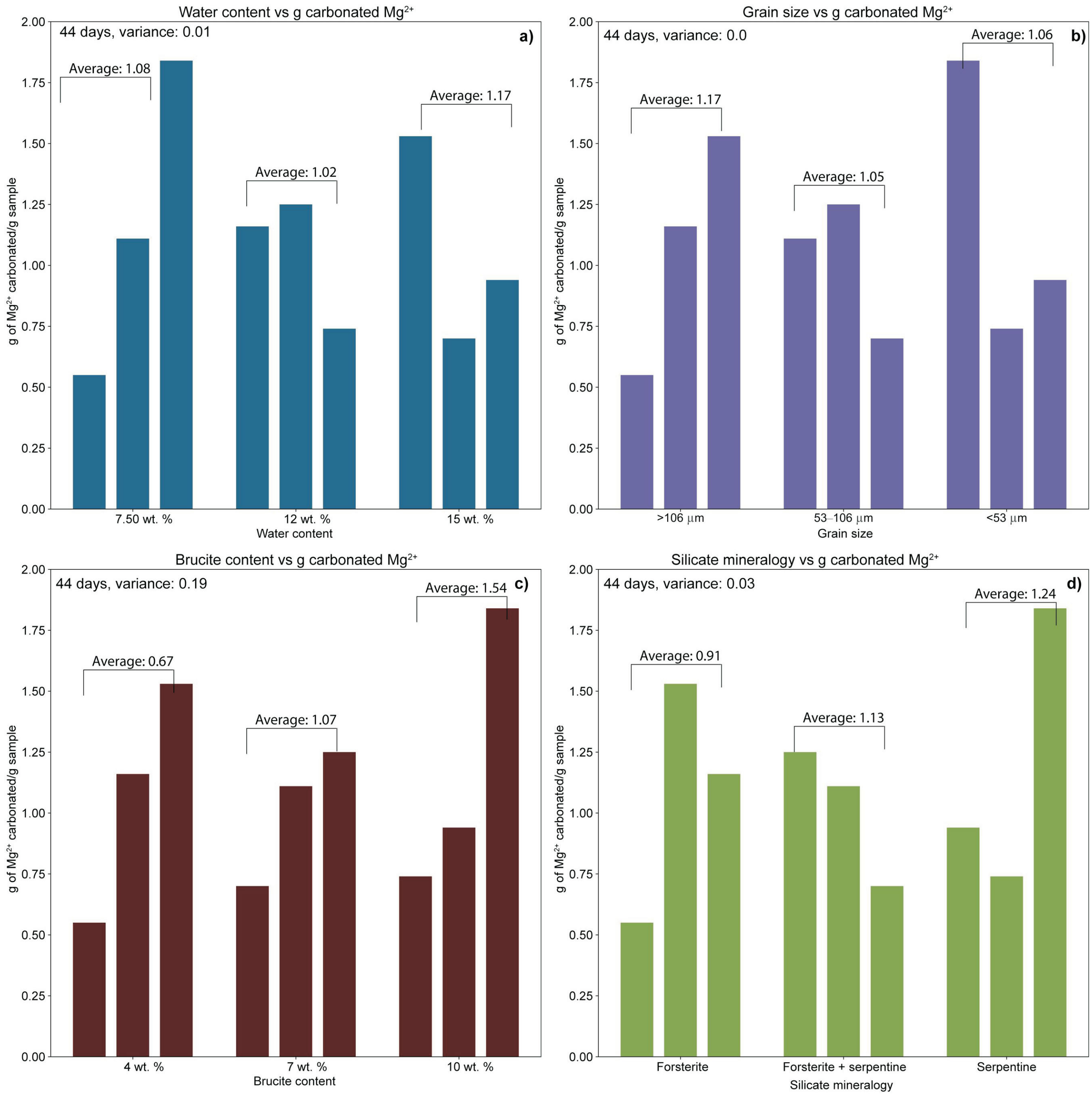

Figure 3. Bar charts showing results of the orthogonal experimental design tests (after 44 days): **a)** grams of Mg^{2+} carbonated per gram of sample versus water content (at 7.5, 12 and 15 wt. %); **b)** grams of Mg^{2+} carbonated per gram of sample versus grain size (>106, 53–106 and <53 µm); **c)** grams of Mg^{2+} carbonated per gram of sample versus brucite content (at 4, 7 and 10 wt. %); **d)** grams of Mg^{2+} carbonated per gram of sample versus mineralogy of samples (only forsterite, half forsterite and half serpentine, and only serpentine). In each subplot, the bars are grouped by level; the average carbonated Mg^{2+} of each level and the variance of each factor are also noted.

cessing. It has been well-established that mine tailings constitute gangue from crushed and ground ore, with clay- and silt- to sand-sized particles and a grain size ranging from 10 to 1000 µm (Lapakko et al., 2006; Salmon and Malmström, 2006; Power et al., 2021). Such grain size variation is highly advantageous for the rate of mineral carbonation because the smaller grain size generates large amounts of freshly exposed surfaces while the larger grain size provides sufficient space for gas, fluid and rock interaction (Pronost et al., 2011; Vogeli et al., 2011; Bodénan et al., 2014; Li and Hitch, 2017; Li et al., 2018). In the present study, the samples were compacted to simulate mine tailings in a tailings pond. The mixture has high density, which could have deleterious effects on CO_2 diffusion and cation transportation. Larger grain size benefits the larger pore size and higher porosity, resulting in faster carbonation rates and higher CO_2-capturing ability. Therefore, samples with >106 µm grain size showed the greatest extent of carbonation throughout the experimental duration in the present study. Grain size distribution significantly affects the CO_2-capturing ability of tailings, which makes it important.

Results from the Orthogonal Experimental Design

According to the variance analysis of OED, ranking the variance from high to low will rank factors that are the most influential to the least influential (Larson, 2008; Zhang and Ma, 2013). As shown by the results on day 44 in Table 3, brucite content is the most influential factor for labile Mg^{2+} carbonation during the air carbonation test, followed by the content of silicate minerals (i.e., serpentine and forsterite), water content and grain size. It should be noted that this order does change depending on the duration of the test. The variance of brucite content showed a consistent increase with the progression of the experiment from day 4 to day 44 (0.03 at 4 days; 0.10 at 20 days; and 0.19 at 44 days). In contrast, the effect of grain size showed a continuous decrease, leading to minimal variance values. Overall, the results from the air carbonation experiment with OED design provide valuable information, suggesting that mineralogy is the primary factor that controls the labile Mg^{2+} carbonation capacity of tailings. Water content is the second most important component, as it controls the dissolution of minerals and CO_2 gas. Grain size is also significant, as it affects the reactive mineral surface area, porosity and CO_2 mobility.

Conclusion

An improved understanding of mineral reactivity in the short and long term is critical for accurately assessing carbon sequestration capacity. Technical difficulties and financial concerns were encountered using traditional experimental methods (e.g., flow-through time-resolved analysis) and motivated the design of new experimental protocols to assess reactivity.This study proposes the use of air carbonation tests with an orthogonal experimental design to characterize the carbon sequestration reactivity of ultramafic minerals and tailings. The orthogonal design allows testing of multiple contributing factors without having to carry out numerous experiments. In addition, the air carbonation tests modelled coupled mineral dissolution–carbonation reaction in porous media and assessed labile Mg^{2+} by detecting inorganic carbon content gain in the sample. Nevertheless, the orthogonal experimental design data analysis demonstrated here is preliminary. Future work will involve in-depth data analysis and statistical calculations. Important conclusions that are drawn from this study are that 1) mineralogy, especially brucite content, is the most important controlling factor during labile Mg^{2+} carbonation; 2) water content and grain size are relatively less important, but samples with higher moisture content and larger grain size will have more reactivity; 3) controls from silicate minerals may prevail in the later reaction stages because stoichiometric dissolution will slow the reaction kinetics. Overall, the experimental results provide insights into controls at the pore scale. The adoption of orthogonal experimental design has implications for future experimental design when studying multiple factors and their impact level. These findings will contribute to discovering more advanced strategies to quantify reactivity and characterize the capacity of ultramafic minerals and tailings for carbon capture and storage.

Acknowledgments

The authors thank Geoscience BC and the Natural Sciences and Engineering Research Council of Canada's (NSERC) Discovery Grant, awarded to G.M. Dipple, for financial support of this study. Additional support (the International Tuition Award, the Special UBC Graduate Scholarship, the W.H. Mathews Scholarship, the Colin D. Spence Memorial Scholarship in Geology, and the Thomas and Marguerite MacKay Memorial Scholarship) was provided by The University of British Columbia, Department of Earth, Ocean and Atmospheric Sciences. Special thanks for R. Beckie from the Department of Earth, Ocean and Atmospheric Sciences of The University of British Columbia for reviewing this manuscript and providing valuable insights.

References

Arce, G.L.A.F., Soares Neto, T.G., Ávila, I., Luna, C.M.R. and Carvalho, J.A. (2017): Leaching optimization of mining wastes with lizardite and brucite contents for use in indirect mineral carbonation through the pH swing method; Journal of Cleaner Production, v. 141, p. 1324–1336, URL <https://doi.org/10.1016/j.jclepro.2016.09.204>.

Bea, S.A., Wilson, S.A., Mayer, K.U., Dipple, G.M., Power, I.M. and Gamazo, P. (2012): Reactive transport modeling of natural carbon sequestration in ultramafic mine tailings; Vadose Zone Journal, v. 11, art. vzj2011.0053, URL <https://doi.org/10.2136/vzj2011.0053>.

Beerling, D.J., Leake, J.R., Long, S.P., Scholes, J.D., Ton, J., Nelson, P.N., Bird, M., Kantzas, E., Taylor, L.L., Sarkar, B., Kelland, M., DeLucia, E., Kantola, I., Müller, C., Rau, G. and Hansen, J. (2018): Farming with crops and rocks to address global climate, food and soil security; Nature Plants, v. 4, p. 138–147, URL <https://doi.org/10.1038/s41477-018-0108-y>.

Berg, A. and Banwart, S.A. (2000): Carbon dioxide mediated dissolution of Ca-feldspar: implications for silicate weathering; Chemical Geology, v. 163, no. 1–4, p. 25–42, URL <https://doi.org/10.1016/S0009-2541(99)00132-1>.

Bickle, M.J. (2009): Geological carbon storage; Nature Geoscience, v. 2, p. 815–818, URL <https://doi.org/10.1038/ngeo687>.

Bodénan, F., Bourgeois, F., Petiot, C., Augé, T., Bonfils, B., Julcour-Lebigue, C., Guyot, F., Boukary, A., Tremosa, J., Lassin, A., Gaucher, E.C. and Chiquet, P. (2014): Ex situ mineral carbonation for CO_2 mitigation: evaluation of mining waste resources, aqueous carbonation processability and life cycle assessment (Carmex project); Minerals Engineering, v. 59, p. 52–63, URL <https://doi.org/10.1016/j.mineng.2014.01.011>.

Bullock, L.A., James, R.H., Matter, J., Renforth, P. and Teagle, D.A.H. (2021): Global carbon dioxide removal potential of waste materials from metal and diamond mining; Frontiers in Climate, v. 3, art. 694175, URL <https://doi.org/10.3389/fclim.2021.694175>.

De Baere, B., François, R. and Mayer, K.U. (2015): Measuring mineral dissolution kinetics using on-line flow-through time resolved analysis (FT-TRA): an exploratory study with forsterite; Chemical Geology, v. 413, p. 107–118, URL <https://doi.org/10.1016/j.chemgeo.2015.08.024>.

Hamilton, J.L., Wilson, S.A., Morgan, B., Harrison, A.L., Turvey, C.C., Paterson, D.J., Dipple, G.M. and Southam, G. (2020): Accelerating mineral carbonation in ultramafic mine tailings via direct CO_2 reaction and heap leaching with potential for base metal enrichment and recovery; Economic Geology, v. 115, p. 303–323, URL <https://doi.org/10.5382/ECONGEO.4710>.

Harrison, A.L., Dipple, G.M., Power, I.M. and Mayer, K.U. (2015): Influence of surface passivation and water content on mineral reactions in unsaturated porous media: implications for brucite carbonation and CO_2 sequestration; Geochimica et Cosmochimica Acta, v. 148, p. 477–495, URL <https://doi.org/10.1016/j.gca.2014.10.020>.

Harrison, A.L., Dipple, G.M., Power, I.M. and Mayer, K.U. (2016): The impact of evolving mineral-water-gas interfacial areas on mineral-fluid reaction rates in unsaturated porous media; Chemical Geology, v. 421, p. 65–80, URL <https://doi.org/10.1016/j.chemgeo.2015.12.005>.

Harrison, A.L., Dipple, G.M., Song, W., Power, I.M., Mayer, K.U., Beinlich, A. and Sinton, D. (2017): Changes in mineral reactivity driven by pore fluid mobility in partially wetted porous media; Chemical Geology, v. 463, p. 1–11, URL <https://doi.org/10.1016/j.chemgeo.2017.05.003>.

Harrison, A.L., Power, I.M. and Dipple, G.M. (2013): Accelerated carbonation of brucite in mine tailings for carbon sequestration; Environmental Science & Technology, v. 47, p. 126–134, URL <https://doi.org/10.1021/es3012854>.

Haug, T.A., Munz, I.A. and Kleiv, R.A. (2011): Importance of dissolution and precipitation kinetics for mineral carbonation; Energy Procedia, v. 4, p. 5029–5036, URL <https://doi.org/10.1016/j.egypro.2011.02.475>.

Knauss, K.G. and Wolery, T.J. (1988): The dissolution kinetics of quartz as a function of pH and time at 70°C; Geochimica et Cosmochimica Acta, v. 52, no. 1, p. 43–53, URL <https://doi.org/10.1016/0016-7037(88)90055-5>.

Lackner, K.S. (2003): A guide to CO_2 sequestration; Science, v. 300, no. 5626, p. 1677–1678, URL <https://doi.org/10.1126/science.1079033>.

Lackner, K.S., Wendt, C.H., Butt, D.P., Joyce, E.L. and Sharp, D.H. (1995): Carbon dioxide disposal in carbonate minerals; Energy, v. 20, p. 1153–1170, URL <https://doi.org/10.1016/0360-5442(95)00071-N>.

Lapakko, K.A., Engstrom, J.N. and Antonson, D.A. (2006): Effects of particle size on drainage quality from three lithologies; *in* 7th International Conference on Acid Rock Drainage (ICARD), March 26–30, 2006, St. Louis, Missouri, R.I. Barnhisel (ed.), American Society of Mining Reclamation, v. 2, p. 1026–1050, poster paper, URL <https://doi.org/10.21000/jasmr06021026>.

Larson, M.G. (2008): Analysis of variance; Circulation, v. 117, p. 115–121, URL <https://doi.org/10.1161/CIRCULATIONAHA.107.654335>.

Li, J. and Hitch, M. (2017): Ultra-fine grinding and mechanical activation of mine waste rock using a planetary mill for mineral carbonation; International Journal of Mineral Processing, v. 158, p. 18–26, URL <https://doi.org/10.1016/j.minpro.2016.11.016>.

Li, J., Hitch, M., Power, I.M. and Pan, Y. (2018): Integrated mineral carbonation of ultramafic mine deposits—a review; Minerals, v. 8, no. 4, art. 147, URL <https://doi.org/10.3390/min8040147>.

Lu, X., Carroll, K.J., Turvey, C.C. and Dipple, G.M. (2022): Rate and capacity of cation release from ultramafic mine tailings for carbon capture and storage; Applied Geochemistry, v. 140, art. 105285, URL <https://doi.org/10.1016/j.apgeochem.2022.105285>.

Matter, J.M. and Kelemen, P.B. (2009): Permanent storage of carbon dioxide in geological reservoirs by mineral carbonation; Nature Geoscience, v. 2, p. 837–841, URL <https://doi.org/10.1038/ngeo683>.

McCutcheon, J., Power, I.M., Shuster, J., Harrison, A.L., Dipple, G.M. and Southam, G. (2019): Carbon sequestration in biogenic magnesite and other magnesium carbonate minerals; Environmental Science & Technology, v. 53, p. 3225–3227, URL <https://doi.org/10.1021/acs.est8b07055>.

McGrail, B.P., Ho, A., Reidel, S. and Schaef, H. (2003): Use and features of basalt formations for geologic sequestration; *in* Greenhouse Gas Control Technology - 6th International Conference, Proceedings of the 6th International Conference on Greenhouse Gas Control Technologies, Volume 2, October 1–4, 2002, Kyoto, Japan, p. 1637–1640, URL <https://doi.org/10.1016/b978-008044276-1/50264-6>.

McGrail, B.P., Schaef, T.H., Ho, A.M., Chien, Y.J., Dooley, J.J. and Davidson, C.L. (2006): Potential for carbon dioxide sequestration in flood basalts; Journal of Geophysical Research, Solid Earth, v. 111, p. 1–13, URL <https://doi.org/10.1029/2005JB004169>.

Paulo, C., Power, I.M., Stubbs, A.R., Wang, B., Zeyen, N. and Wilson, S.A. (2021): Evaluating feedstocks for carbon dioxide removal by enhanced rock weathering and CO_2 mineralization; Applied Geochemistry, v. 129, art. 104955, URL <https://doi.org/10.1016/j.apgeochem.2021.104955>.

Pokrovsky, O.S. and Schott, J. (2004): Experimental study of brucite dissolution and precipitation in aqueous solutions: surface speciation and chemical affinity control; Geochimica et Cosmochimica Acta, v. 68, p. 31–45, URL <https://doi.org/10.1016/S0016-7037(03)00238-2>.

Power, I.M., Harrison, A.L., Dipple, G.M., Wilson, S.A., Kelemen, P.B., Hitch, M. and Southam, G. (2013a): Carbon mineralization: from natural analogues to engineered systems; Reviews in Mineralogy and Geochemistry, v. 77, p. 305–360, URL <https://doi.org/10.2138/rmg.2013.77.9>.

Power, I.M., Paulo, C., Long, H., Lockhart, J.A., Stubbs, A.R., French, D. and Caldwell, R. (2021): Carbonation, cementation, and stabilization of ultramafic mine tailings; Environmental Science & Technology, v. 55, p. 10056–10066, URL <https://doi.org/10.1021/acs.est.1c01570>.

Power, I.M., Wilson, S.A. and Dipple, G.M. (2013b): Serpentinite carbonation for CO_2 sequestration; Elements, v. 9, p. 115–121, URL <https://doi.org/10.2113/gselements.9.2.115>.

Power, I.M., Wilson, S.A., Small, D.P., Dipple, G.M., Wan, W. and Southam, G. (2011): Microbially mediated mineral carbonation: roles of phototrophy and heterotrophy; Environmental Science & Technology, v. 45, p. 9061–9068, URL <https://doi.org/10.1021/es201648g>.

Pronost, J., Beaudoin, G., Tremblay, J., Larachi, F., Duchesne, J., Hébert, R. and Constantin, M. (2011): Carbon sequestration kinetic and storage capacity of ultramafic mining waste; Environmental Science & Technology, v. 45, p. 9413–9420, URL <https://doi.org/10.1021/es203063a>.

Raudsepp, M., Pani, E. and Dipple, G.M. (1999): Measuring mineral abundance in skarn. I. The Rietveld method using X-ray powder-diffraction data; Canadian Mineralogist, v. 37, no. 1, p. 1–15.

Rozalen, M., Ramos, M.E., Fiore, S., Gervilla, F. and Huertas, F.J. (2014): Minerals in the human body effect of oxalate and pH on chrysotile dissolution at 25 °C: an experimental study; American Mineralogist, v. 99, p. 589–600, URL <https://doi.org/10.2138/am.2014.4636>.

Salmon, S.U. and Malmström, M.E. (2006): Quantification of mineral dissolution rates and applicability of rate laws: laboratory studies of mill tailings; Applied Geochemistry, v. 21, no. 2, p. 269–288, URL <https://doi.org/10.1016/j.apgeochem.2005.09.014>.

Seifritz, W. (1990): CO_2 disposal by means of silicates; Nature, v. 345, art. 486, URL <https://doi.org/10.1038/345486b0>.

Sipilä, J., Teir, S. and Zevenhoven, R. (2008): Carbon dioxide sequestration by mineral carbonation: literature review update 2005–2007; Åbo Akademi University, Faculty of Technology, Heat Engineering Laboratory, Report 2008-1, Turku, Finland, 52 p., URL <https://doi.org/10.1080/00908310600628263>.

Snæbjörnsdóttir, S., Gislason, S.R., Galeczka, I.M. and Oelkers, E.H. (2018): Reaction path modelling of in-situ mineralisation of CO_2 at the CarbFix site at Hellisheidi, SW-Iceland; Geochimica et Cosmochimica Acta, v. 220, p. 348–366, URL <https://doi.org/10.1016/j.gca.2017.09.053>.

Thom, J.G.M., Dipple, G.M., Power, I.M. and Harrison, A.L. (2013): Chrysotile dissolution rates: implications for carbon sequestration; Applied Geochemistry, v. 35, p. 244–254, URL <https://doi.org/10.1016/j.apgeochem.2013.04.016>.

Tosca, N.J. and Masterson, A.L. (2014): Chemical controls on incipient Mg-silicate crystallization at 25°C: implications for early and late diagenesis; Clay Minerals, v. 49, p. 165–194, URL <https://doi.org/10.1180/claymin.2014.049.2.03>.

Turvey, C.C., Hamilton, J.L. and Wilson, S.A. (2018a): Comparison of Rietveld-compatible structureless fitting analysis methods for accurate quantification of carbon dioxide fixation in ultramafic mine tailings; American Mineralogist, v. 103, p. 1649–1662, URL <https://doi.org/10.2138/am-2018-6515>.

Turvey, C.C., Wilson, S.A., Hamilton, J.L., Tait, A.W., McCutcheon, J., Beinlich, A., Fallon, S.J., Dipple, G.M. and Southam, G. (2018b): Hydrotalcites and hydrated Mg-carbonates as carbon sinks in serpentinite mineral wastes from the Woodsreef chrysotile mine, New South Wales, Australia: controls on carbonate mineralogy and efficiency of CO_2 air capture in mine tailings; International Journal of Greenhouse Gas Control, v. 79, p. 38–60, URL <https://doi.org/10.1016/j.ijggc.2018.09.015>.

Turvey, C.C., Wynands, E.R. and Dipple, G.M. (2022): A new method for rapid brucite quantification using thermogravimetric analysis; SSRN Electronic Journal, v. 718, art. 179366, URL <https://doi.org/10.2139/ssrn.4187016>.

Tutolo, B.M. and Tosca, N.J. (2018): Experimental examination of the Mg-silicate-carbonate system at ambient temperature: implications for alkaline chemical sedimentation and lacustrine carbonate formation; Geochimica et Cosmochimica Acta, v. 225, p. 80–101, URL <https://doi.org/10.1016/j.gca.2018.01.019>.

Uddin, S., Rao, S.R., Mirnezami, M. and Finch, J.A. (2012): Processing an ultramafic ore using fiber disintegration by acid attack; International Journal of Mineral Processing, v. 102–103, p. 38–44, URL <https://doi.org/10.1016/j.minpro.2011.09.015>.

Vogeli, J., Reid, D.L., Becker, M., Broadhurst, J. and Franzidis, J.P. (2011): Investigation of the potential for mineral carbonation of PGM tailings in South Africa; Minerals Engineering, v. 24, no. 12, p. 1348–1356, URL <https://doi.org/10.1016/j.mineng.2011.07.005>.

Washbourne, C.L., Renforth, P. and Manning, D.A.C. (2012): Investigating carbonate formation in urban soils as a method for capture and storage of atmospheric carbon; Science of the Total Environment, v. 431, p. 166–175, URL <https://doi.org/10.1016/j.scitotenv.2012.05.037>.

Wilson, S.A., Barker, S.L.L., Dipple, G.M. and Atudorei, V. (2010): Isotopic disequilibrium during uptake of atmospheric CO_2 into mine process waters: implications for CO_2 sequestration; Environmental Science & Technology, v. 44, p. 9522–9529, URL <https://doi.org/10.1021/es1021125>.

Wilson, S.A., Dipple, G.M., Power, I.M., Barker, S.L.L., Fallon, S.J. and Southam, G. (2011): Subarctic weathering of mineral wastes provides a sink for atmospheric CO_2; Environmental Science & Technology, v. 45, p. 7727–7736, URL <https://doi.org/10.1021/es202112y>.

Wilson, S.A., Dipple, G.M., Power, I.M., Thom, J.M., Anderson, R.G., Raudsepp, M., Gabites, J.E. and Southam, G. (2009): Carbon dioxide fixation within mine wastes of ultramafic-hosted ore deposits: examples from the Clinton Creek and Cassiar chrysotile deposits, Canada; Economic Geology, v. 104, p. 95–112, URL <https://doi.org/10.2113/gsecongeo.104.1.95>.

Wilson, S.A., Harrison, A.L., Dipple, G.M., Power, I.M., Barker, S.L.L., Ulrich Mayer, K., Fallon, S.J., Raudsepp, M. and Southam, G. (2014): Offsetting of CO_2 emissions by air capture in mine tailings at the Mount Keith nickel mine, Western Australia: rates, controls and prospects for carbon neutral mining; International Journal of Greenhouse Gas Control, v. 25, p. 121–140, URL <https://doi.org/10.1016/j.ijggc.2014.04.002>.

Wolff-Boenisch, D. and Galeczka, I.M. (2018): Flow-through reactor experiments on basalt-(sea)water-CO_2 reactions at 90 °C and neutral pH. What happens to the basalt pore space under post-injection conditions?; International Journal of Greenhouse Gas Control, v. 68, p. 176–190, URL <https://doi.org/10.1016/j.ijggc.2017.11.013>.

Wu, H. (2013): Application of orthogonal experimental design for the automatic software testing; Applied Mechanics and Material, v. 347–350, p. 812–818, URL <https://doi.org/10.4028/www.scientific.net/AMM.347-350.812>.

Zhang, X.F. and Ma, B. (2013): Orthogonal experiment design and analysis of compound activator; Applied Mechanics and Material, v. 438–439, p. 404–407, URL <https://doi.org/10.4028/www.scientific.net/AMM.438-439.404>.

Zurovac, J. and Brown, R. (2012): Orthogonal design: a powerful method for comparative effectiveness research with multiple interventions; Center on Healthcare Effectiveness, Issue Brief, April 2012, Mathematica Policy Research, Inc., Princeton, New Jersey, 4 p.

Microbial Biosensors in Through-Cover Mineral Exploration

B.P. Iulianella Phillips[1], Department of Earth, Ocean and Atmospheric Sciences, The University of British Columbia, Vancouver, British Columbia, bphillips@eoas.ubc.ca

R.L. Simister, Department of Microbiology and Immunology, The University of British Columbia, Vancouver, British Columbia

C.J.R. Hart, (formerly) Department of Earth, Ocean and Atmospheric Sciences, The University of British Columbia, Vancouver, British Columbia

S.A. Crowe, Departments of Earth, Ocean and Atmospheric Sciences, and Microbiology and Immunology, The University of British Columbia, Vancouver, British Columbia

Iulianella Phillips, B.P., Simister, R.L., Hart, C.J.R. and Crowe, S.A. (2023): Microbial biosensors in through-cover mineral exploration; *in* Geoscience BC Summary of Activities 2022: Minerals, Geoscience BC, Report 2023-01, p. 55–62.

Introduction

Mineral exploration in Canada—and other areas across the globe—is becoming increasingly difficult with the likelihood of future mineral-resource discoveries being buried beneath appreciable glacial overburden and/or bedrock. The development of innovative exploration approaches to detect mineralization through overburden is vital for continued success in the discovery of new resources (Winterburn et al., 2017). One such technique, microbial-community fingerprinting, shows great potential when exploring for mineral targets that are hidden by thick (>2 m), complex and transported surficial materials. With continued development, it may transform how exploration is carried out for buried natural resources (Iulianella Phillips, 2020; Simister et al., 2020).

Micro-organisms kinetically enhance geochemical reactions, including the dissolution and formation of diverse minerals, and harness energy from these reactions to support their metabolism and growth in nearly every low-temperature geological setting (Newman and Banfield, 2002; Falkowski et al., 2008). They are acutely sensitive, often responding rapidly to the dynamics of chemical and physical properties in their surrounding environments. Subtle changes in mineral bioavailability, for example, can be reflected in dramatic shifts in the composition and activity of microbial communities (Reith and Rogers, 2008; Wakelin et al., 2012; Leslie et al., 2014; Fierer, 2017). Analyses of microbial-community composition and structure thus have a strong potential to resolve chemical and physical differences between environments that are not readily discernible through conventional geochemical and geophysical surveys.

The advent of high-throughput sequencing platforms over the last decade has transformed the capacity to interrogate complex microbial communities across a wide range of environmental matrices (Binladen et al., 2007; Zhou et al., 2015). The application of these technologies enables high-throughput profiling of the taxonomic compositions and metabolic potential of soil-microbial communities across defined survey areas. Given that every individual soil sample contains thousands of microbial taxa, each containing hundreds to thousands of genes sensing and interacting with the surrounding soil environment (Fierer, 2017), the statistical power of this approach to identify anomalies is unprecedented.

Previous Research

Two British Columbia (BC) porphyry-copper deposits, the Highland Valley Highmont South Cu-Mo deposit (HVC) of Teck Resources Ltd. and the Consolidated Woodjam Copper Corp. Deerhorn Cu-Au deposit, were used to evaluate microbiological techniques for sulphide exploration in BC (Figure 1). B-horizon soil samples were analyzed for inorganic geochemistry (aqua-regia digestion with inductively coupled plasma–mass spectrometry [ICP-MS] finish) and microbial-DNA sequencing (16S rRNA marker gene; Iulianella Phillips, 2020; Simister et al., 2020). In both cases, mineralization is covered by transported glacial overburden (2–10 m at HVC and 25–60 m at Deerhorn), with compositional variation in surface materials (e.g., till blanket, organic deposits, glaciolacustrine sediments; Iulianella Phillips, 2020).

The authors have shown that microbial-community fingerprinting can detect anomalies in bacterial populations in the surface environment that correlate with the surface projection of sulphide mineralization (Iulianella Phillips, 2020; Simister et al., 2020). Deposit-scale investigations of HVC and Deerhorn revealed suites of micro-organisms that have

[1] *The lead author is a 2022 Geoscience BC Scholarship recipient.*

This publication is also available, free of charge, as colour digital files in Adobe Acrobat® PDF format from the Geoscience BC website: http://geosciencebc.com/updates/summary-of-activities/.

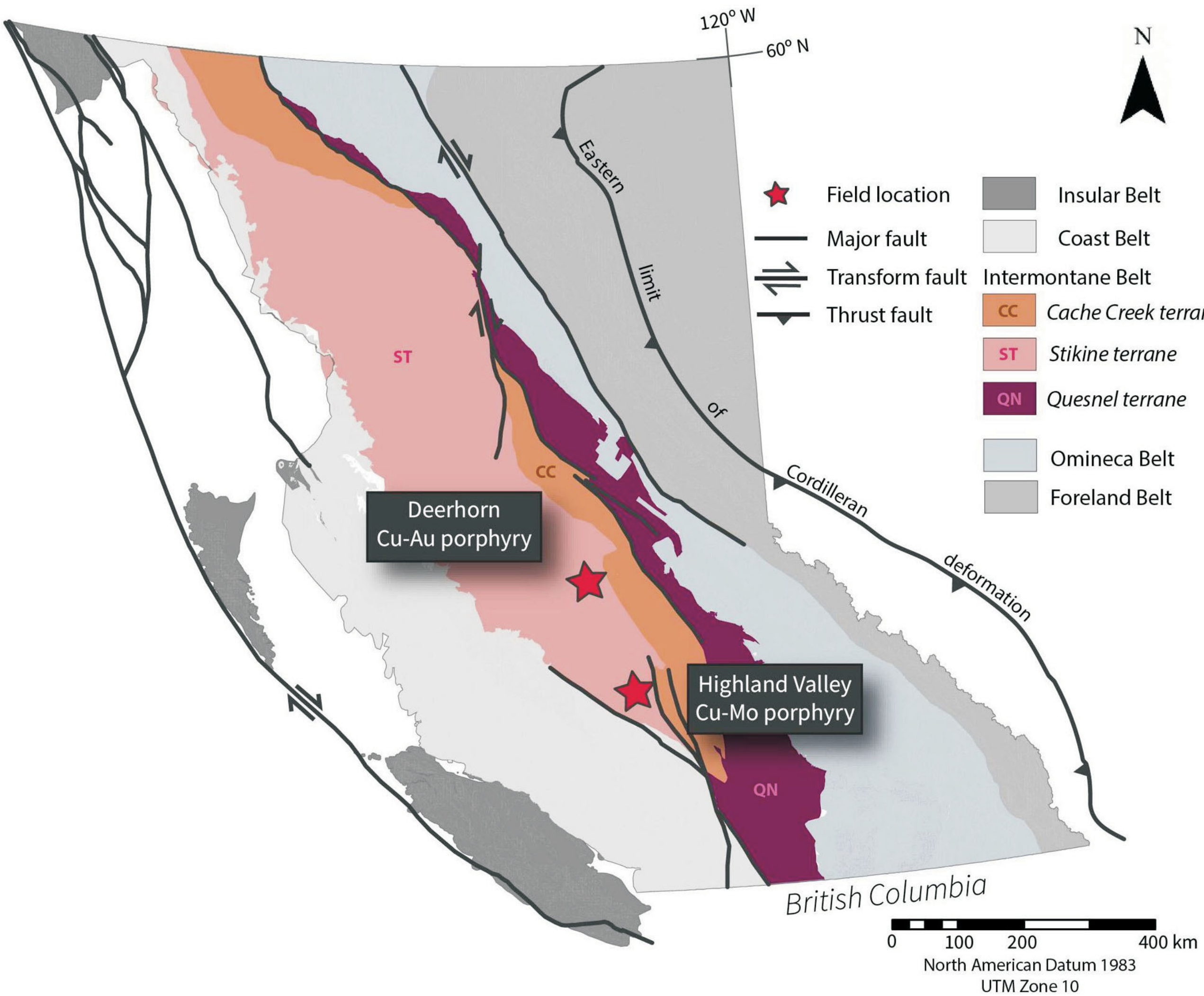

Figure 1. Locations of porphyry-Cu research sites (Highland Valley Highmont South Cu-Mo deposit and Deerhorn Cu-Au deposit) and the Mount Washington high-sulphidation Au-Ag-Cu epithermal prospect. Thick black lines indicate major faults. Terranes and geological belts are characterized based on bedrock mapping carried out by the British Columbia Geological Survey (BCGS; Cui et al., 2017).

statistically significant (p <0.05) shifts in relative abundance occurring directly above the surface projection of mineralization (0.1% Cu equivalent and 0.2% Au equivalent at HVC and Deerhorn, respectively; Figures 2 and 3). Specifically, microbial anomalies at Deerhorn discriminate mineralization at the surface where no detectable geochemical signal has been generated (Figure 3). These results signify the efficacy of using modern DNA sequencing to elucidate buried mineralization and provide the support for further investigations into the use of microbial communities to sense chemical and physical changes in their environment, with respect to ore mineralization.

New Research

Several new avenues of research are currently being explored to reduce knowledge and technology barriers in the application of DNA sequencing for the exploration of concealed mineral deposits. Field-based approaches include new orientation studies across glacial till–covered Pb-Zn sulphide mineralization and saturation-gradient soil sampling in a bog-wetland setting. Experimental approaches focus on assessing bacterial responses to changes in mineralogy and temperature. These objectives support the progressive development of microbial-community fingerprinting into a tool that may be employed by the mineral-exploration and mining industry.

Pine Point Mississippi Valley–Type Deposit

In September 2022, a geochemical and geobiological soil survey was completed across mineralized collapse structures at the Pine Point Mississippi Valley–type (MVT) Pb-Zn deposit in the Northwest Territories (NWT). The Pine Point district is located on the southern shore of Great Slave Lake (Figure 4), on the eastern edge of the Western Cana-

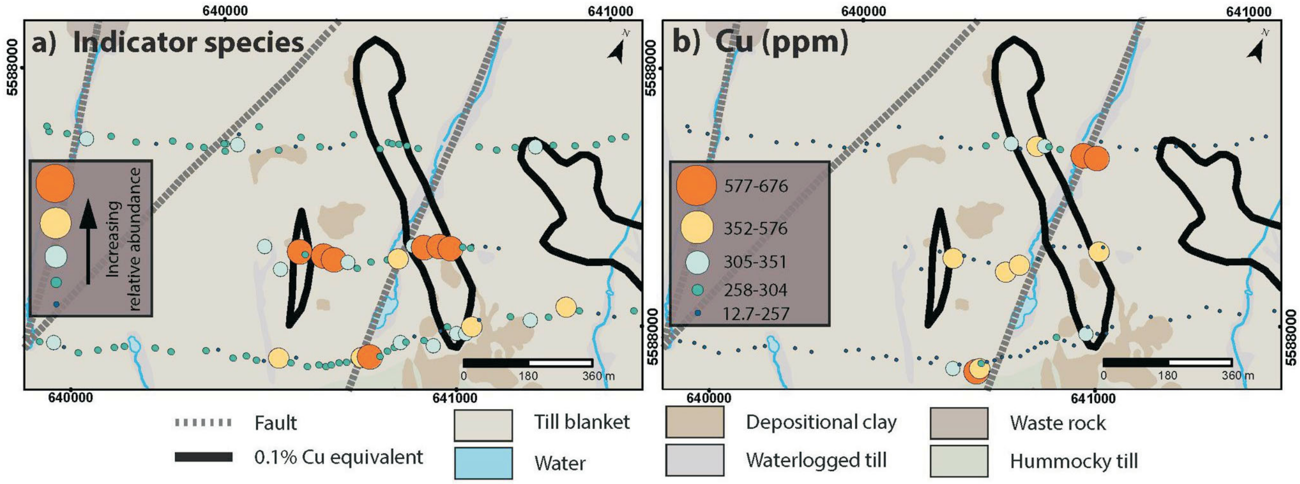

Figure 2. Example of an indicator micro-organism **(a)** and the Cu-anomaly map of the same area **(b)** from the Highland Valley Highmont South Cu-Mo deposit. Geochemical data derived from aqua-regia digestion of B-horizon soils with ICP-MS finish. Microbiological data derived from 16S rRNA gene DNA sequencing. Co-ordinates in UTM Zone 10, NAD 83.

dian Sedimentary Basin (WCSB). Sulphide mineralization (galena+sphalerite±marcasite±pyrite) is hosted predominantly in Middle Devonian carbonate units within or proximal to the dolomitized Presqu'ile barrier-reef complex (Hannigan, 2007). Mineralization is largely structurally controlled along the McDonald–Great Slave Lake fault system (Hannigan, 2007), exhibiting either prismatic or tabular geometries (Krebs and Macqueen, 1984; Cumming et al., 1990). Generally, the area is covered with Quaternary sediments that are dominated by organic deposits, lacustrine and glaciolacustrine sediments, glacial-till blanket, and lesser alluvial and eolian deposits (Oviatt et al., 2013). The sampled field area is characterized by prismatic mineralization and covered by glaciolacustrine beach sediments, with overburden at its thickest where it infills the collapse structures (~40 m).

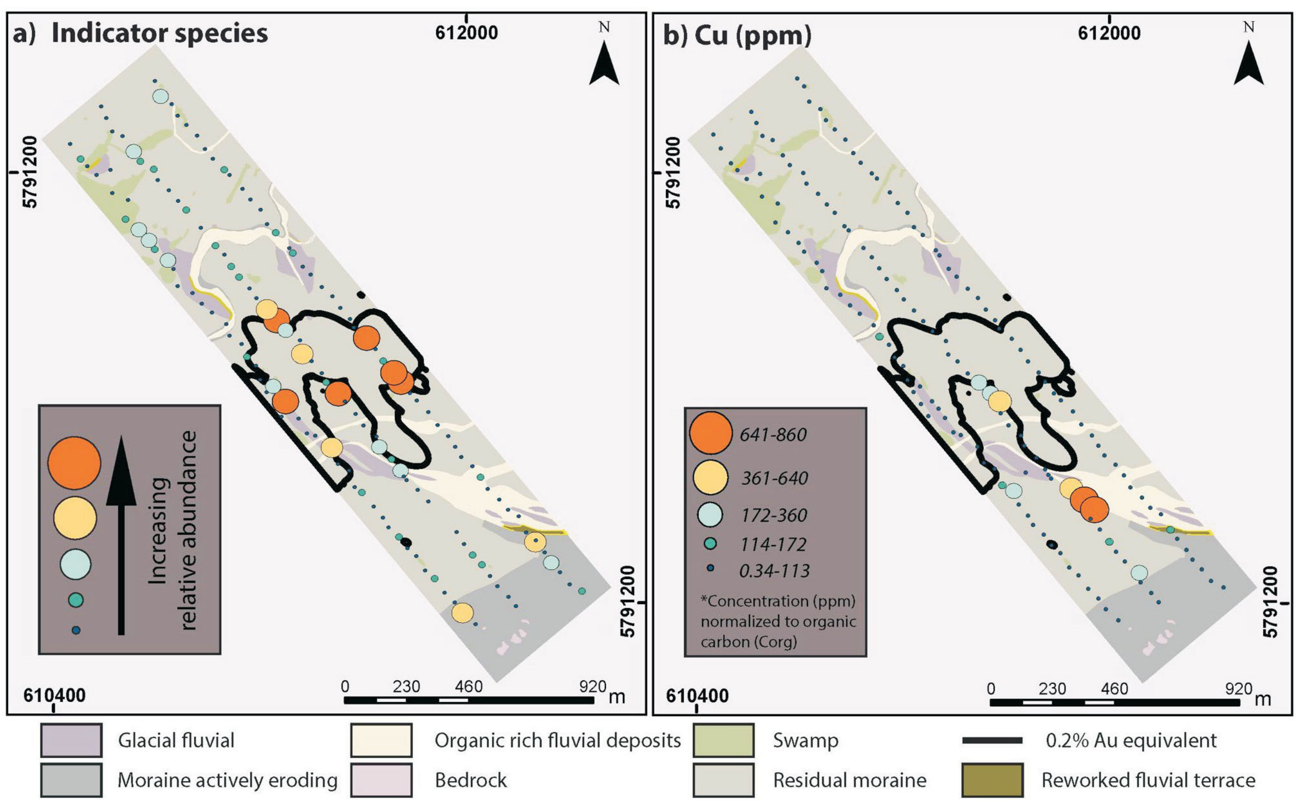

Figure 3. Example of an indicator micro-organism **(a)** and the Cu-anomaly map (normalized to organic carbon) of the same area **(b)** from the Deerhorn Cu-Au deposit. Geochemical data derived from aqua-regia digestion of B-horizon soils with ICP-MS finish. Microbiological data derived from 16S rRNA gene DNA sequencing. Co-ordinates in UTM Zone 10, NAD 83.

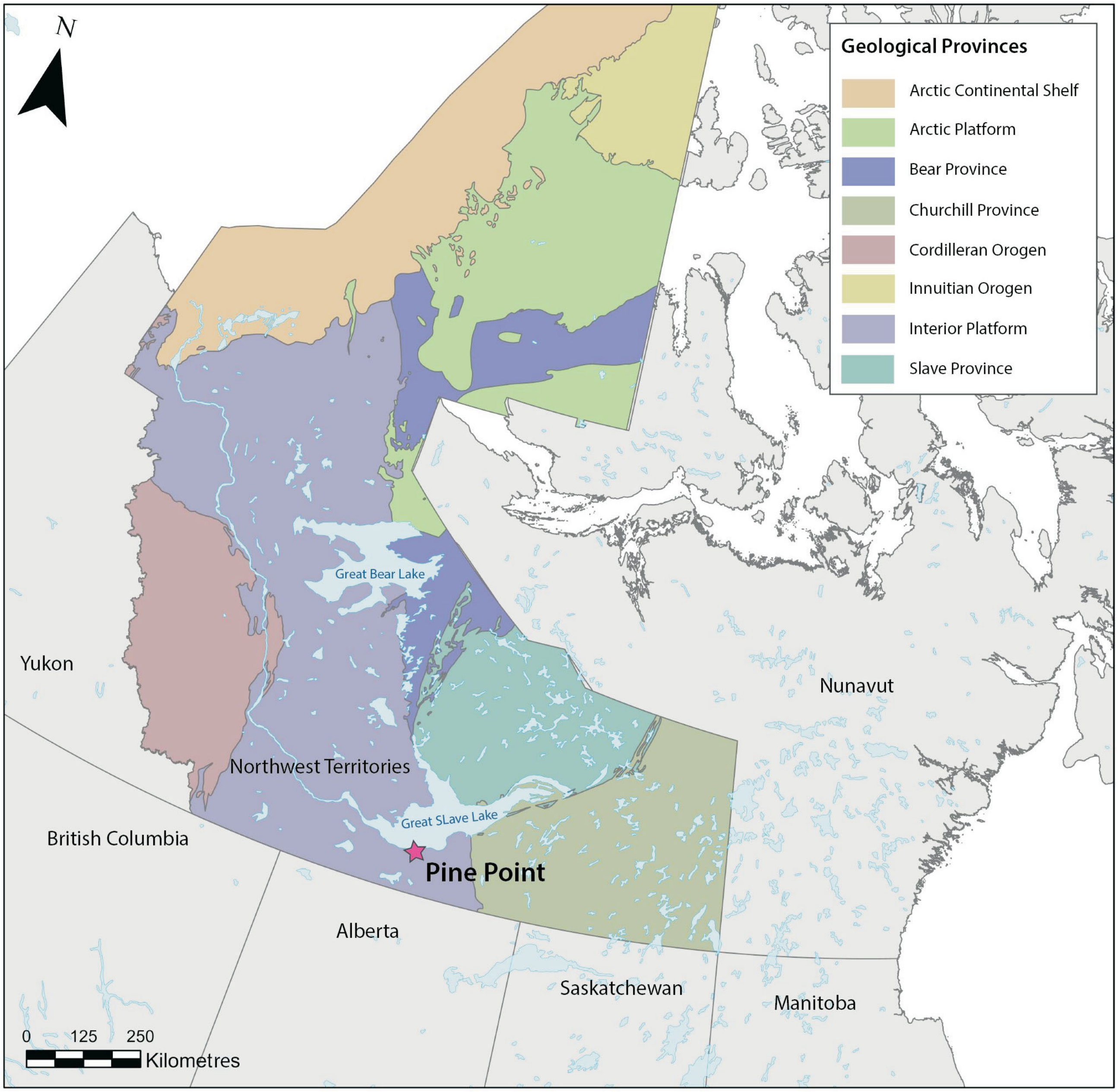

Figure 4. Location of the Pine Point Pb-Zn district, Northwest Territories. Geological provinces are compiled from publicly available data provided by the Northwest Territories Geological Survey (Wheeler et al., 1997).

Thirty-eight soil samples were collected on two survey lines that crossed the surface projection of the mineralized collapse structures, with sampling gradationally spaced outward from mineralization into background cover soils. Soils for microbial-community analysis were sampled with sterilized equipment and without field screening to preserve the microbial community as much as possible. Descriptions were documented for in situ physicochemical variables at each sample site for every observed soil horizon in the profile. The B-horizon soils were targeted for geochemical and microbial soil samples, although multiple horizons were taken where possible. Soils for microbiological analyses were preserved each day in the field for cell-count analysis, RNA profiling, and intracellular and extracellular DNA profiling. Although this work is not focused in BC, the application of soil microbial-community fingerprinting in the Pine Point district has direct implications when exploring for metalliferous sulphide deposits in covered terrain across BC, northern latitudes in North America, and globally.

Microbial Community Response to Soil Moisture

Soil Preservation

Water content is a fundamental control on the composition and activity of microbial communities in soils, globally (Fierer, 2017). Soils in climates with higher moisture also typically contain higher levels of microbial biomass (Serna-Chavez et al., 2013). Soil-moisture contents, furthermore, likely have an important effect on the preservation of soil-microbial communities during prolonged transport and storage. Whereas it is common practice that microbial communities in soils are immediately frozen to preserve the integrity of DNA and the fidelity of community profiles by arresting further growth or decay (Delavaux et al., 2020), soil surveys in mineral-exploration programs are often in remote areas with limited resources for freezing and typically have lengthy transport times to the laboratory. Successful surveys therefore require knowledge of how temporary and extended sample-storage regimes, like cooling and drying, influence soil-microbial communities, specifically with respect to the potential for community change during storage. Here, it is important to know how community-turnover rates respond to storage temperature and moisture contents.

The University of British Columbia (UBC) Totem Plant Science Field Station provides an excellent on-campus soil environment to conduct, and collect materials, for soil-related experiments. The lead author has sampled bulk soil from the UBC Totem Plant Science Field Station and subjected it to a range of temperature and moisture conditions to examine subsequent effects on the microbial community composition, diversity and structure, as well as microbial population turnover rates. These perturbations include freezing samples at –20°C, leaving samples at room temperature, and allowing the samples to dry out (Figure 5). Currently, 9 months of timepoints have been sampled, while preparation for DNA sequencing of the soil-microbial communities is ongoing (initial microbial-community composition of this soil is described in Iulianella Phillips et al. [2022]). These experiments will inform the development of a minimal and robust sample-storage protocol and serve as a test of the relationships between warming and drying of soils and microbial-community turnover.

Bog Wetlands

Bog wetlands represent an important carbon sink globally, with northern peatlands estimated as storing 415 ±150 Pg (petagrams) of carbon (Beaulne et al., 2021)—approximately 30% of total carbon stores on Earth (Parish et al., 2008). The impact of soil moisture on microbial-community composition and activity is particularly relevant as micro-organisms likely play an important role in controlling carbon release versus storage in response to changing climate (Kitson and Bell, 2020; Carrell et al., 2022). Water-saturated surface materials, such as bogs, also present a substantial challenge to the mineral-exploration industry as there are few methodologies that are effective when exploring in these settings. In microbial fingerprinting, substantial community anomalies are expected to develop in response to water saturation and discriminating between these

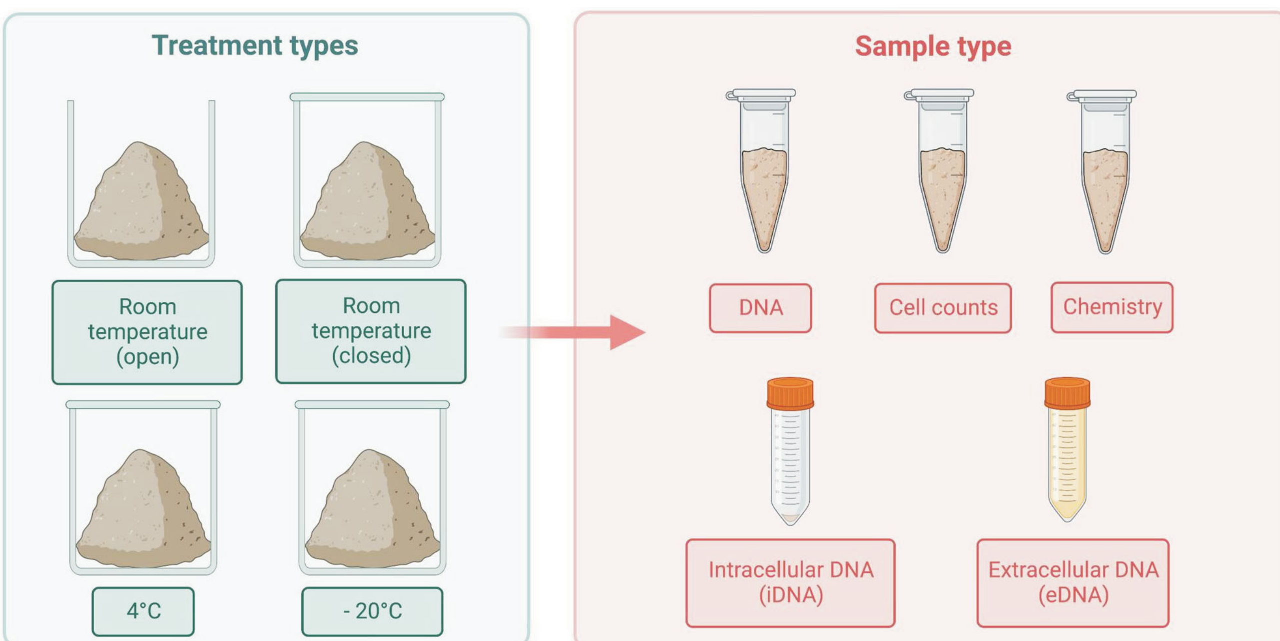

Figure 5. Schematic representation of the soil-preservation experiment, including the treatment types and the different sample products. For each timepoint and treatment type, soil is sampled for DNA, bacterial-cell counts, chemistry, intracellular DNA (DNA found within intact cells) and extracellular DNA (DNA derived from outside the cell in environmental samples).

and bona fide anomalies related to mineral resources will be key to successful surveys. Therefore, bog wetlands provide a unique opportunity to study the effects of soil moisture on microbial communities, both in the context of microbial carbon cycling and in the development of ore-mineral anomalies.

The lead author has sampled organic soils within bog wetlands in northern Canada across a soil-moisture gradient to determine differences in soil-microbial–community composition, structure and activity related to water content. Sampling focused around both the active and permafrost layers of a palsa, as well as the adjacent organic-rich materials from a bog and a fen (Figure 6). Differences in composition and structure will be determined through DNA sequencing, whereas activity will be determined through isotope-labelling experiments.

Mineral Sensing

Micro-organisms are acutely sensitive to chemical and physical differences in their environments. For example, subtle variability in trace Fe concentrations in seawater is reflected in striking differences in phytoplankton distribution and activity in the oceans (O'Reilly et al., 1998; Fuhrman, 2009). They also typically have strong affinities for surfaces (Grinberg et al., 2019), often creating biofilms (Donlan et al., 2002; Dang et al., 2016), and are able to selectively colonize specific solid substrates to meet a broad diversity of physiological needs (Tuson et al., 2013; Finley et al., 2022). However, despite a large body of evidence showing that micro-organisms preferentially associate with surfaces, the molecular mechanisms through which they sense these surfaces, and select those that confer a specific advantage, remain almost entirely unknown. To test for microbial capacity to sense mineral surfaces, the gene expression of *E. coli*, a well-studied model micro-organism, will be evaluated when exposed to rock- and ore-forming minerals. Specifically, microbial responses to olivine, K-feldspar, plagioclase-group minerals, quartz and pyrite will be assessed. These analyses will enable the identification of genes that are differentially activated in response to mineral exposure. The identities of upregulated genes will provide insight into the metabolic machinery behind microbial mineral sensing. Such novel insight into biological sensing of surfaces will inform conceptual models of microbe-mineral interactions in soils, as well as open up new opportunities for the development of mineral biosensors for a broad range of applications.

Conclusions

Outcomes from these deposit-scale orientation studies have highlighted the potential for geomicrobiological tools and techniques for successful application to through-cover mineral exploration in British Columbia and beyond. Current research directions focus specifically on reducing fundamental unknowns about the behaviour and variation of

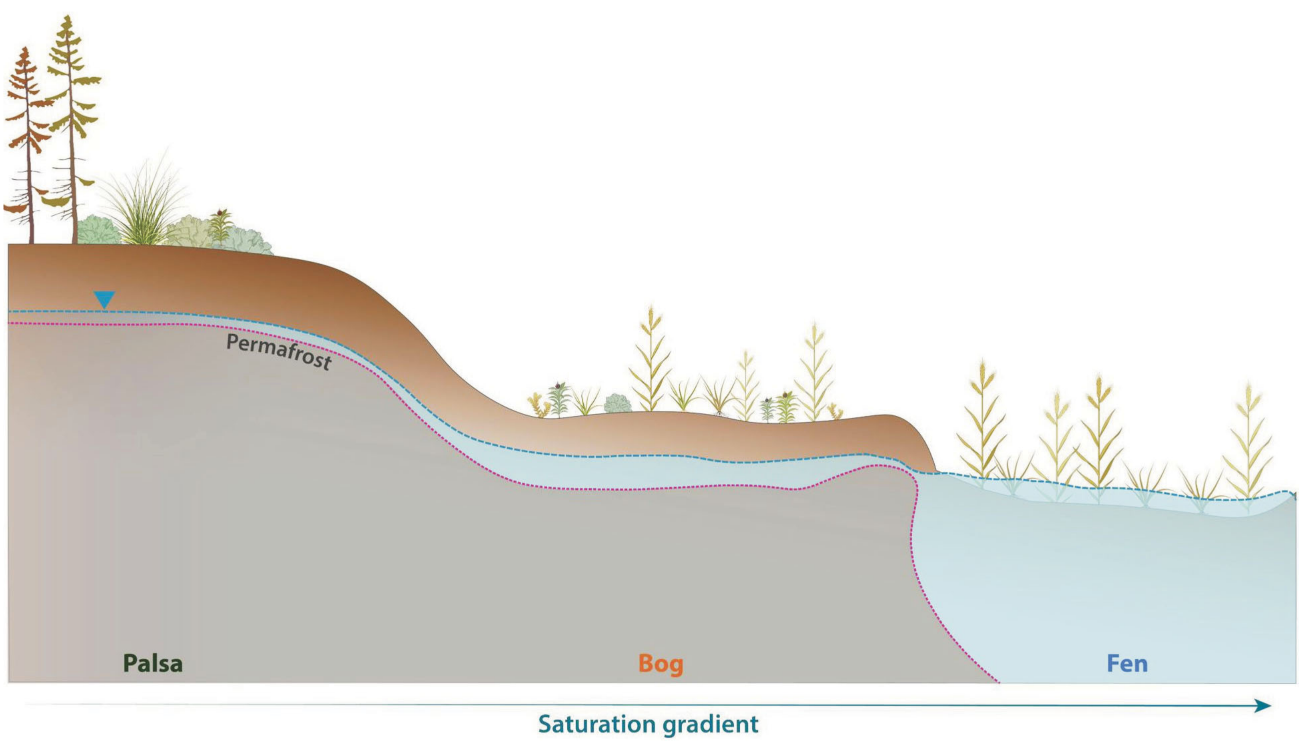

Figure 6. Schematic diagram of a saturation gradient from a dry palsa with an active and a permafrost layer to saturated soil conditions in bogs and fens. Depth of soil saturation is denoted by the dashed blue line and depth of the permafrost layer is indicated by the dashed pink line.

microbial communities in response to chemical and physical changes in the environment. This focus includes assessing DNA sequencing and microbial-community fingerprinting in a carbonate-hosted Pb-Zn–sulphide mineralization district covered by glacial sediments; assessing the impact of transport and storage on the persistence of microbial-community anomalies in soils; exploring the relationships between micro-organism function and variation in land type and water content; and evaluating gene expression of *E. coli* in response to different mineral exposures. Each of these activities serves on a different level to support the use of microbiology-based mineral exploration in different mineral systems, in various terrains and climates, and to develop practical and informed transport and storage protocols for use by industry.

Acknowledgments

This research is derived from the Exploration Geochemistry Initiative at the Mineral Deposit Research Unit run by the late Dr. Peter Winterburn, and the Crowe Lab at The University of British Columbia. The author thanks the funding partners for the initial stages of this research, Natural Sciences and Engineering Research Council of Canada, Bureau Veritas and Geoscience BC, as well as the Northwest Territories Geological Survey for their ongoing support and Osisko Metals for camp accommodations, field access and metadata at Pine Point. Field sampling for this work would not have been possible without the efforts of R. Chouinard (Highland Valley), S. Rich (Deerhorn), and B. Canam and B. Elliott (Pine Point). Credit is also given to M. Friend for improving earlier versions of this manuscript.

References

Beaulne, J., Garneau, M., Magnan, G. and Boucher, É. (2021): Peat deposits store more carbon than trees in forested peatlands of the Boreal Biome; Scientific Reports, v. 11, art. 2567, 11 p., URL <https://www.nature.com/articles/s41598-021-82004-x> [November 2022].

Binladen, J., Gilbert, M.T.P., Bollback, J.P., Panitz, F., Bendixen, C., Nielsen, R. and Willerslev, E. (2007): The use of coded PCR primers enables high-throughput sequencing of multiple homolog amplification products by 454 parallel sequencing; PLoS ONE, v. 2, no. 2, p. 1–9, URL <https://journals.plos.org/plosone/article?id=10.1371/journal.pone.0000197> [October 2022].

Carrell, A.A., Lawrence, T.J., Cabugao, K.G.M., Carper, D.L., Pelletier, D.A., Lee, J.H., Jawdy, S.S., Grimwood, J., Schmutz, J., Hanson, P.J., Shaw, A.J. and Weston, D.J. (2022): Habitat-adapted microbial communities mediate Sphagnum peatmoss resilience to warming; New Phytologist, v. 234, no. 6, p. 2111–2125, URL <https://nph.onlinelibrary.wiley.com/doi/full/10.1111/nph.18072> [November 2022].

Cui, Y., Miller, D., Schiarizza, P. and Diakow, L. (2017): British Columbia digital geology; British Columbia Ministry of Energy, Mines, and Low Carbon Innovation, BC Geological Survey, Open File 2017-8, 9 p., URL <https://www2.gov.bc.ca/gov/content/industry/mineral-exploration-mining/british-columbia-geological-survey/geology/bcdigitalgeology> [October 2022].

Cumming, G.L., Kyle, J.R., and Sangster, D.F. (1990): Pine Point: a case history of lead isotopic homogeneity in a Mississippi Valley-type district; Economic Geology, v. 85, p. 133–144, URL <https://publications.gc.ca/collections/collection_2020/rncan-nrcan/m41-11/M41-11-107-2019-eng.pdf> [October 2022].

Dang, H. and Lovell, C.R. (2016): Microbial surface colonization and biofilm development in marine environments; Microbiology and Molecular Biology Reviews, v. 80, no. 1, p. 91–138, URL <https://journals.asm.org/doi/10.1128/MMBR.00037-15> [November 2022].

Delavaux, C.S., Dever, J.D., Karppinin, E.M. and Bainard, L.D. (2020): Keeping it cool: soil sample cold pack storage and DNA shipment up to 1 month does not impact metabarcoding results; Ecology and Evolution, v. 10, p. 4652–4664, URL <https://onlinelibrary.wiley.com/doi/full/10.1002/ece3.6219> [October 2022].

Donlan, R.M. (2002): Biofilms: microbial life on surfaces; Emerging Infectious Diseases, v. 8, no. 9, p. 881–890, URL <https://pubmed.ncbi.nlm.nih.gov/12194761/> [October 2022].

Falkowski, P.G., Fenchel, T. and Delong, E.F. (2008): The microbial engines that drive Earth's biogeochemical cycles; Science, v. 320, p. 1034–1040, URL <https://www.science.org/doi/10.1126/science.1153213> [October 2022].

Fierer, N. (2017): Embracing the unknown: disentangling the complexities of the soil microbiome; Nature Reviews Microbiology, v. 15, no. 10, p. 579–590, URL <https://www.nature.com/articles/nrmicro.2017.87> [October 2022].

Finley, B.K., Mau, R.L., Hayer, M., Stone, B.W., Morrissey, E.M., Koch, B.J., Rasmussen, C., Dijkstra, P., Schwartz, E. and Hungate, B.A. (2022): Soil minerals affect taxon-specific bacterial growth; The ISME Journal, v. 16, p. 1318–1326, URL <https://www.nature.com/articles/s41396-021-01162-y> [November 2022].

Fuhrman, J.A. (2009): Microbial community structure and its functional implications; Nature, v. 459, no. 7244, p. 193–199, URL <https://www.nature.com/articles/nature08058> [October 2022].

Grinberg M., Orevi, T. and Kashtan, N. (2019): Bacterial surface colonization, preferential attachment and fitness under periodic stress; PLoS Computational Biology, v. 15, no. 3, e1006815, URL <https://journals.plos.org/ploscompbiol/article?id=10.1371/journal.pcbi.1006815> [November 2022].

Hannigan, P. (2007): Metallogeny of the Pine Point Mississippi Valley-Type zinc-lead district, southern Northwest Territories; *in* Mineral Deposits of Canada: A Synthesis of Major Deposit-Types, District Metallogeny, W.D. Goodfellow (ed.), Geological Association of Canada, Mineral Deposits Division, Special Publication 5, p. 609–632, URL <https://geoscan.nrcan.gc.ca/starweb/geoscan/servlet.starweb?path=geoscan/fulle.web&search1=R=224197> [October 2022].

Iulianella Phillips, B.P. (2020): Microorganisms as sensors for concealed mineral deposits: application and development of microbiological mineral exploration in the Northwest Territories and British Columbia, Canada; M.Sc. thesis, The University of British Columbia, 211 p., URL <https://open.library.ubc.ca/soa/cIRcle/collections/ubctheses/24/items/1.0390297> [October 2022].

Iulianella Phillips, B.P., Simister, R.L., Luck, P.M., Hart, C.J.R., and Crowe, S.A. (2022): Microbial sensing of sulphide ore mineralization; *in* Geoscience BC Summary of Activities 2021: Minerals, Geoscience BC, Report 2022-01, p. 45–52, URL <https://cdn.geosciencebc.com/pdf/SummaryofActivities2021/Minerals/Sch_Phillips_MineralsSOA2021.pdf> [October 2022].

Kitson, E. and Bell, N.G.A. (2020): The response of microbial communities to peatland drainage and rewetting: a review; Frontiers of Microbiology, v. 29, URL <https://www.frontiersin.org/articles/10.3389/fmicb.2020.582812/full> [November 2022].

Krebs, W. and Macqueen, R. (1984): Sequence of diagenetic and mineralization events, Pine Point lead-zinc property, Northwest Territories, Canada; Bulletin of Canadian Petroleum Geology, v. 32, no. 4, p. 434–464, <https://pubs.geoscienceworld.org/cspg/bcpg/article-abstract/32/4/434/57366/SEQUENCE-OF-DIAGENETIC-AND-MINERALIZATION-EVENTS> [November 2022].

Leslie, K., Oates, C.J., Kyser, T.K. and Fowle, D.A. (2014): Biogeochemical controls on metal mobility: modeling a Cu-Zn VMS deposit in column flow-through studies; Geochemistry: Exploration, Environment, Analysis, v. 14, p. 59–70, URL <https://geea.lyellcollection.org/content/14/1/59/tab-figures-data> [November 2022].

Newman, D.K. and Banfield, J.F. (2002): Geomicrobiology: how molecular-scale interactions underpin biogeochemical systems; Science, v. 296, no. 5570, p. 1071–1077, URL <https://www.science.org/doi/abs/10.1126/science.1010716?keytype2=tf_ipsecsha&ijkey=3b7fbf439b72ef152968ec5b99e05a350dd73007> [November 2022].

O'Reilly, J.E., Maritorena, S., Mitchell, B.G., Siegel, D.A., Carder, K.L., Garver, S.A., Kahru, M. and McClain, C. (1998): Ocean color chlorophyll algorithms for SeaWiFS; Journal of Geophysical Research, v. 103, no. C11, p. 24937–24953, URL <https://core.ac.uk/download/pdf/154474926.pdf> [November 2022].

Oviatt, N.M., McClenaghan, M.B., Paulen, R.C., and Gleeson, S.A. (2013): Till geochemical signatures of the Pine Point Mississippi Valley–type district, Northwest Territories; Geological Survey of Canada Open File 7320, 18 p., URL <https://geoscan.nrcan.gc.ca/starweb/geoscan/servlet.starweb?path=geoscan/downloade.web&search1=R=292247> [October 2022].

Parish, F., Sirin, A., Charman, D., Joosten, H., Minayeva, T., Silvius, M. and Stringer, L., editors (2008): Assessment on Peatlands, Biodiversity and Climate Change: Main Report; Global Environment Centre, Kuala Lumpur and Wetlands International, Wageningen, URL <http://www.imcg.net/media/download_gallery/books/assessment_peatland.pdf> [October 2022].

Reith, F. and Rogers, S.L. (2008): Assessment of bacterial communities in auriferous and non-auriferous soils using genetic and functional fingerprinting; Geomicrobiology Journal, v. 25, no. 34, p. 203–215, URL <https://www.tandfonline.com/doi/abs/10.1080/01490450802081846> [October 2022].

Serna-Chavez, H.M., Fierer, N. and Van Bodegom, P.M. (2013): Global drivers and patterns of microbial abundance in soil; Global Ecology and Biogeography, v. 22, no. 10, p. 1162–1172, URL <https://onlinelibrary.wiley.com/doi/10.1111/geb.12070> [October 2022].

Simister, R.L., Iulianella Phillips, B.P., Winterburn, P.A. and Crowe, S.A. (2020): Microbial-community fingerprints as indicators for buried mineralization, Geoscience BC Report 2020-03 and MDRU Publication 446, 31 p., URL <http://www.geosciencebc.com/i/project_data/GBC%20Report2020-03/GBC%20Report%202020-03%20Microbial-Community%20Fingerprints%20as%20Indicators%20for%20Buried%20Mineralization%20in%20British%20Columbia_revised_BIP.pdf> [October 2022].

Tuson, H.H. and Weibel, D.B. (2013): Bacteria-surface interactions; Soft Matter, v. 9, no. 18, p. 4368–4380, URL <https://www.ncbi.nlm.nih.gov/pmc/articles/PMC3733390/> [November 2022].

Wakelin, S., Anand, R.R., Macfarlane, C., Reith, F., Noble, R. and Rogers, S. (2012): Assessing microbiological surface expression over an overburden-covered VMS deposit; Journal of Geochemical Exploration, v. 112, p. 262–271, URL <https://www.sciencedirect.com/science/article/abs/pii/S0375674211001853?via%3Dihub> [October 2022].

Wheeler, J.O., Hoffman, P.F., Card, K.D., Davidson, A., Sanford, B.V., Okulitch, A.V. and Roest, W.R., compilers (1997): NWT portion of Geological Map of Canada; Geological Survey of Canada, Map D1860A, URL <https://datahub-ntgs.opendata.arcgis.com/maps/nwt-geology-gscmapd1860a/about> [October 2022].

Winterburn, P., Noble, R. and Lawie, D. (2017): Advances in exploration geochemistry, 2007 to 2017 and beyond; Geochemistry: Exploration, Environment, Analysis, v. 20, p. 157–166, URL <https://www.mdru.ubc.ca/wp-content/uploads/2019/01/WinterburnExplore17.34.pdf> [October 2022].

Zhou, J., He, Z., Yang, Y., Deng, Y., Tringe, S. and Alvarez-Cohen, L. (2015): High-throughput metagenomic technologies for complex microbial community analysis: open and closed formats; mBio, v. 6, no. 1, p. 106–113, URL <https://pubmed.ncbi.nlm.nih.gov/25626903/> [October 2022].

Review of Fibre-Optic Applications in the Geosciences in British Columbia

S. Hendi[1], Department of Earth, Ocean and Atmospheric Sciences, The University of British Columbia, Vancouver, British Columbia, shendi@eoas.ubc.ca

E. Eberhardt, Department of Earth, Ocean and Atmospheric Sciences, The University of British Columbia, Vancouver, British Columbia

M. Gorjian, Department of Earth, Ocean and Atmospheric Sciences, The University of British Columbia, Vancouver, British Columbia

Hendi, S., Eberhardt, E. and Gorjian, M. (2023): Review of fibre-optic applications in the geosciences in British Columbia; *in* Geoscience BC Summary of Activities 2022: Minerals, Geoscience BC, Report 2023-01, p. 63–70.

Introduction

The importance of technology in monitoring on the scale of millimetres to tens of kilometres the spatial variability of deformation due to heterogeneity and complex geometry of excavations in the short term and long term is demonstrated by the constant monitoring of the geometry of underground openings in mines, as well as the monitoring and measurement of strain and temperature in boreholes in geothermal and hydrocarbon projects. In recent years, fibre optics has become a more significant and noticeably promising technology for geoscience applications, including in underground rock engineering, geothermal energy, geophysics, and oil and gas. Compared to most conventional monitoring equipment, fibre-optic sensors are robust and geometrically flexible, possess long-term stability, are cost-effective, extend coverage with improved resolution, offer data at a higher sample rate and, above all, can be monitored remotely, which reduces the number of workers required to work underground and enhances the safety of any underground operation.

Discrete and distributed sensors are the two main categories of fibre-optic sensors. The comparison of these two types of fibre-optic sensors is shown in Table 1. By changing the spacing of a diffraction grating in the fibre or in a cavity between two ends of micrometre-scale fibre, discrete sensors respond to strain and temperature.

Distributed fibre-optic sensing is a type of technology that allows for continuous, real-time measurements to be made along the entire length of a fibre-optic cable by detecting changes in temperature, strain and other parameters, using the physical properties of light travelling along the fibre. In distributed sensing, the fibre-optic cable itself is the strain and temperature sensor. Distributed-sensing mechanisms can interrogate Rayleigh, Raman or Brillouin scattering phenomena. Distributed acoustic-sensing (DAS) and distributed temperature-sensing (DTS) systems, among others, enable short-term and long-term monitoring of an object to describe its dynamic behaviour.

In the sections that follow, the theory behind fibre-optic sensors and their applications in the geosciences is demonstrated.

Before this work, no attempt had been made to summarize the application of fibre optics in geoscience projects. This study aims to investigate the potential application of fibre optics to geoscience by reviewing previous applications.

Fibre Bragg Grating-Based Discrete Sensor

Theory

Fibre Bragg gratings (FBGs; FBGS Technologies, GmbH, 2022) are discrete sensors created by exposing a single-mode optical-fibre core laterally to a spatially variable pattern of intense laser light. A periodic spatial variation in light intensity induces a permanent increase in the refractive index of the fibre's core, resulting in a fixed index modulation based on the exposure pattern. This type of fixed index modulation is known as a 'grating'. A small amount of light is reflected at each periodic refraction change. When the grating period is nearly half the wavelength of the input light, all the reflected light signals combine coherently into one major reflection at a specific wavelength. This is known as the 'Bragg condition' and the wavelength at which this reflection takes place is known as the 'Bragg wavelength'. The wavelengths of light signals that are not phase-matched to the Bragg wavelength are generally transparent (Figure 1).

Applications

Sensors of the FBG type have been widely employed as a robust and very effective technology for monitoring structural health. The FBG sensor has several advantages over

[1]*The lead author is a 2022 Geoscience BC Scholarship recipient.*

This publication is also available, free of charge, as colour digital files in Adobe Acrobat® PDF format from the Geoscience BC website: http://geosciencebc.com/updates/summary-of-activities/.

Table 1. Comparison between discrete and distributed fibre-optic sensors.

Sensor type	Discrete sensor	Distributed sensor	
	Fibre Bragg grating	Distributed temperature sensing	Distributed acoustic sensing
Operating principle	Wavelength-modulated (periodic modulation of the refractive index over a short length)	Scattering-based (Raman)	Scattering-based (Rayleigh)
Measurement parameter	Strain Temperature Acceleration Pressure	Temperature	Strain
Measurement type	Single-point or multipoint sensing	Continuous	Continuous
Intensity of backscatter light	High	Low	Low
Spatial resolution	Controlled by the physical spacing of the sensor (increase in the spatial resolution = more expensive sensor)	Depends on the sensitivity of the interrogator unit	Depends on the sensitivity of the interrogator unit
Price	High	Low	Low
Advantages	Can measure multiple parameters simultaneously over short distances	Can provide the profile of temperature change along the whole length of the fibre-optic system	Can provide the profile of temperature change along the whole length of the fibre-optic system
Disadvantages	Strain influences temperature results and vice versa Price of the FBG fibre depends on the number of sensors inside (increase in number of sensors = increase in price of sensors)	Compared to FBG, the measurement requires a longer time and averaging	Compared to FBG, the measurement requires a longer time and averaging

conventional sensors like extensometers, strain gauges and dial gauges, such as its small physical dimensions, light weight, immunity to electromagnetic interference, ease of installation, long-term stability and ability to use multiple wavelengths (Morey et al., 1990; Ferdinand et al., 1997; Cappa et al., 2006; Yin et al., 2008). The geotechnical and mining industries have shown a growing interest in FBG-based sensing systems in recent years and numerous papers have been published on the subject in various fields of study. The monitoring of various geotechnical and structural parameters of crucial importance to mining projects, such as internal temperature variations, pressure changes, deformation changes, vertical settlements and lateral deflections, is typically the focus of researchers (Wang and Gage, 2017; Minardo et al., 2018; Vlachopoulos et al., 2018; Yugay et al., 2020).

In addition to being useful to the mining and geotechnical industries, FBG sensors have been employed in the oil and gas industry, mainly to monitor well integrity during production (Zhong et al., 2007; Johny et al., 2016; Qiao et al., 2017; Zhang et al., 2018; Rong and Qiao, 2019).

These FBG sensors deliver reliable and precise monitoring results that give engineers a reasonable performance assessment, based upon which they may take prompt and efficient action to address possible problems. Several FBG ap-

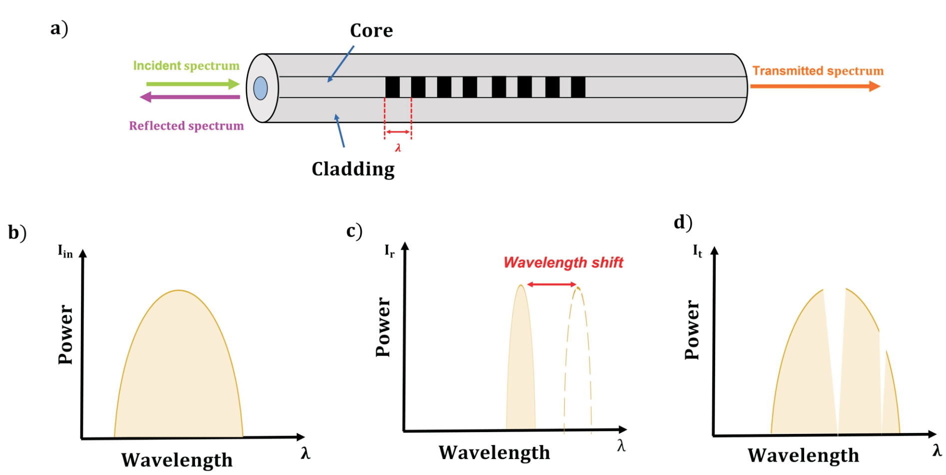

Figure 1. Operating principle of the fibre Bragg grating (FBG) sensor: **a)** the FBG sensor; **b)** incident spectrum; **c)** strained FBG causes wavelength shift and reflected spectrum; **d)** transmitted spectrum (modified from Pendão and Silva, 2022).

plications require additional attention and improvements as they are still in the initial stages of development, such as:

- the use of FBG sensors to directly evaluate the deformability of a rock mass in the field as opposed to the use of indirect classification techniques or extrapolation of laboratory data (Gage et al., 2014);
- the use of FBG sensors in determining the mechanical behaviour of rocks (Tang et al., 2018; Guo et al., 2019);
- the rapid expansion of FBG use and other fibre-optic sensors, particularly in the mining industry, to allow for fully remote real-time monitoring (Zhao et al., 2016; Wang et al., 2021; Hu et al., 2022) and the replacement of mechanical or electrical reference stations, thus making mining operations safer and reducing human casualties (at this time, the use of FBG is limited to preliminary studies); and
- the common use of FGB-based discrete sensors in laboratories to measure strain and characterize rock-mass properties (Gage et al., 2010, 2011, 2013).

Distributed Temperature-Sensing (DTS) System

Theory

The underlying principle of DTS for long-haul measurements is mostly based on Raman scattering (an inelastic scattering phenomenon) combined with optical time-domain reflectometry (OTDR). A short pulse is transmitted into the fibre and the forward-propagating light generates Raman backscattered light at two distinct wavelengths from all points along the fibre, due to the interaction between the light and molecular vibrations in the fibre. The wavelengths of the Raman backscattered light are different from that of the forward-propagating light and are referred to as 'Stokes' and 'anti-Stokes' wavelengths. The amplitude of the Stokes and anti-Stokes light is monitored and the spatial localization of the backscattered light can be determined as long as the propagation speed (velocity) inside the fibre and the time over which the motion occurred are known (Figure 2). The amplitude of the Stokes light is very weakly dependent on temperature, whereas the amplitude of the anti-Stokes light is strongly dependent on temperature. The temperature profile within the optical fibre is determined by calculating the ratio of the amplitudes of the Stokes and the anti-Stokes detected light.

Another type of scattering that is sensitive to changes in temperature and strain is Brillouin scattering. The interaction between the light and acoustic phonons moving through the fibre causes Brillouin scattering. Brillouin scattering is less commonly used as a DTS system in the industry since it is substantially the weakest of the scattering effects and requires more stacking to enhance the signal.

Applications

Distributed temperature sensing has proven to be a noticeably promising method for providing spatiotemporal temperature data in the geosciences. This approach has been widely employed in geothermal energy projects as a cost-effective and environmentally sustainable method to monitor real-time temperature variations over short and long periods. Monitoring fracture development during stimulation

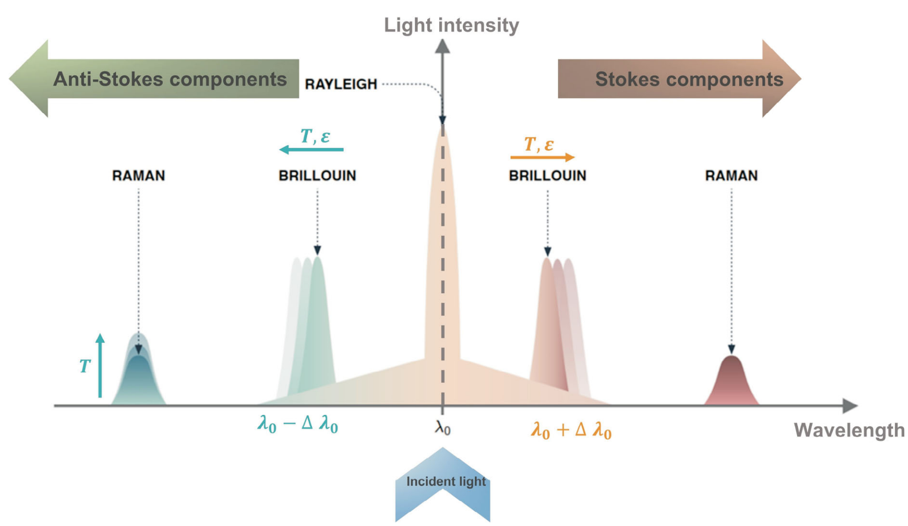

Figure 2. Spectra of scattered light in optical fibre. Rayleigh scattering occurs when the kinetic energy of the incident photons is conserved and, thus, the frequency of the scattered photons equals that of the incident light. Unlike Rayleigh scattering, in Raman and Brillouin scattering the incident-signal spectrum shifts relative to the initial signal, and backscatter spectra occur at both the higher (anti-Stokes) and lower (Stokes) frequency shifts. The intensity of the Raman upshifted-frequency component (anti-Stokes light) is strongly temperature dependent, whereas the intensity of the Raman downshifted-frequency component (Stokes light) is only slightly temperature dependent. Brillouin scattering occurs at a predictable amplitude but with variable frequency (modified from Pendão and Silva, 2022).

and fracturing, monitoring chemical injection during or after a fracturing job, providing permanent monitoring of injector and producer wells to allow identification of the precise zones and fractures that produce fluids as well as monitoring well integrity are just a few of the areas in which it has been applied (Sakaguchi and Matsushima, 2000; Coleman et al., 2015; Read et al., 2015; Sellwood et al., 2015; Freifeld et al., 2016; Patterson et al., 2017).

This technology has also shown success in a range of other applications, including as an early-warning system for coal-mine fire detection, as well as for petroleum pipeline-leak detection and concrete dam-crack monitoring. This system has also recently gained popularity for tasks such as monitoring reservoirs, earth dams, water channels, embankments, tunnels and levee seepage (Ravet et al., 2017, 2019; Nicholas and De Joode, 2022).

Furthermore, its applications extend beyond field measurements. The system outperforms conventional strain gauges in measuring axial and circumferential strains in rock samples. In addition to providing results tolerably consistent with those gathered by strain gauges, results obtained with DTS also indicate the exact location on a rock sample where a fracture first appeared. As a result, a single DTS-system measurement is comparable with that obtained from combined uniaxial and acoustic-emission tests (Xu et al., 2020).

Distributed Acoustic-Sensing System

Theory

In distributed acoustic sensing (DAS), the phase of the backscattered laser (recorded by the interrogator unit) is used to generate continuous seismic array-type recordings at aperture settings that vary from millimetres up to tens of kilometres. As this pulse of light travels down the optical path, interactions within the fibre, which result in light reflections known as 'Rayleigh backscatter', are determined by tiny strain events within the fibre, which in turn are caused by localized acoustic energy. The backscattered light is recombined with a reference phase split from the outgoing pulse to measure the change in phase relative to the previous pulse (Figure 2). This photonic technique is also referred to as 'phase-sensitive optical time-domain/frequency-domain reflectometry' (φ-OTDR/OFDR). The DAS system records the strain of ground motion at virtual locations based on the time of flight of laser pulses termed 'channel'. The strain recorded at a channel is the change in length over a reference length, referred to as the 'gauge length'. As a result, DAS recordings are inherently array measurements. The linear distance between any two virtual Rayleigh scattering points in the fibre core used to make one DAS measurement is in the order of 100 μm based on current telecommunication-grade optical fibre standards (Hartog, 2017).

Compared to Raman and Brillouin scattering, Rayleigh backscattering is considered a direct sensing mechanism and is used to measure environment-dependent propagating effects, due to being intrinsically independent of any external physical fields that may affect the surrounding environment.

Applications

The early 2010s saw the emergence of DAS applications in seismology and geophysics. The primary application of DAS in the energy industry has been to downhole vertical seismic profiling (VSP) and flow detection. It has now become a prominent substitute for VSP sensors (Daley et al., 2013; Li et al., 2015; Hartog, 2017; Martin et al., 2017). Performance of DAS sensors in VSP has been compared to that of conventional sensors through comprehensive investigations and DAS has demonstrated significant advantages over them (Mateeva et al., 2012; Daley et al., 2013; Correa et al., 2017; Lindsey et al., 2017; Wang and Gage, 2017; Jousset et al., 2018; Ajo-Franklin et al., 2019; Becker and Coleman, 2019; Lindsey et al., 2019). Table 2 provides a summary of this comparison.

Additionally, companies are showing increasing interest in the system for petroleum engineering projects such as microseismicity monitoring during hydraulic fracturing, fluid-flow monitoring through production and pipeline monitoring (Daley et al., 2013; Webster et al., 2013; Bakku, 2015; Karrenbach et al., 2017; Ni et al., 2018). Beyond

Table 2. Comparison between different types of geophysical sensors.

Geophysical sensors	Geophone	Hydrophone	Sonic tool	Distributed acoustic
Measurement type	Single point	Single point	Single point	Continuous
Measurement duration	Short-term	Short-term	Short-term	Short-/long-term
Surface measurements	No	No	No	Yes
Signal-to-noise ratio	Yes	Yes	Yes	Yes
Static loading	No	No	No	Yes
Dynamic loading	Yes	Yes	Yes	Yes
Cost	High	High	High	Low
Restrictions	Can't be used in harsh environments	Being a single-point measurement, has caused restrictions on the channel spacing	Only works in fluid-filled well	Being a single-point measurement, has caused restrictions on the channel spacing

these applications, DAS is also being relied upon for critical-infrastructure monitoring, border surveillance and transportation monitoring (Quinn, 2021; White et al., 2021).

Since 2015, academic and government researchers have shown increased interest in DAS to assess the feasibility of applying it to the study of earth systems. As a result, the number of publications on DAS has increased; however, in several areas, the research being conducted is restricted to the laboratory scale (Xue et al., 2014; Xu et al., 2015; Damiano et al., 2017; Lei and Hashimoto, 2019; Zhang et al., 2020). At present, DAS has not been employed in the mining industry, but DAS arrays could theoretically piggyback, with appropriate ground-motion coupling, on other fibre-optic monitoring systems to characterize rock-property variations or to detect and locate rock bursts induced by mining activity.

Summary

Discrete and distributed fibre-optic sensors have attracted remarkable attention in geoscience projects, due to their advantages over pre-existing measurement techniques and sensors. Their lower cost, immunity to electromagnetic interference and long-term stability compared to conventional sensors may enable the permanent installation of these types of sensors as part of a project to perform lifetime measurements in an early-warning system.

Not only could distributed fibre-optic sensors provide the profile of parameter variation over a greater distance than discrete fibre-optic sensors, but they also present the advantage of providing continuous measurements. In addition, distributed sensors are more cost-effective and have a higher spatial resolution. Because of these advantages, extensive research is ongoing as to how they might lend themselves to applications in several geoscience fields.

The use of fibre optics in geoscience projects in British Columbia and elsewhere will lead to significant improvements in measurements and cost savings and, most importantly, to a decrease in human casualties. In particular, deep-mining projects, which are extremely arduous to carry out because of their difficulty of access, may benefit greatly from further research into the use of fibre optics in geoscience projects. Lack of proper measurements in deep-depth projects results in less than optimal design performance and costly mistakes that, on some projects, result in lost value in the range of tens of millions of dollars.

Future Research Directions

The findings of this study will be used to demonstrate the potential applications of fibre optics in geoscience projects to develop novel methods of stress measurement. In addition, the study will be used as a guide for choosing a reliable sensing system for a deep-depth project, including block caving, designed to collect strain and stress measurements (S. Hendi, work in progress).

Acknowledgments

The authors thank the Centre for Innovation in Mineral Resource Engineering and Geoscience BC for their financial support. The authors would also like to thank to M. Rahjoo for his input and constructive comments on aspects of this work.

References

Ajo-Franklin, J.B., Dou, S., Lindsey, N.J., Monga, I., Tracy, C., Robertson, M., Rodriguez Tribaldos, V., Ulrich, C., Freifeld, B., Daley, T. and Li, X. (2019): Distributed acoustic sensing using dark fiber for near-surface characterization and broadband seismic event detection; Scientific Reports, v. 9, no. 1, p. 1–14.

Bakku, S.K. (2015): Fracture characterization from seismic measurements in a borehole; Ph.D. thesis, Massachusetts Institute of Technology, 227 p.

Becker, M.W. and Coleman, T.I. (2019): Distributed acoustic sensing of strain at Earth tide frequencies; Sensors, v. 19, 9 p., URL <https://doi.org/10.3390/s19091975>.

Cappa, F., Guglielmi, Y., Gaffet, S., Lançon, H. and Lamarque, I. (2006): Use of in situ fiber optic sensors to characterize highly heterogeneous elastic displacement fields in fractured rocks; International Journal of Rock Mechanics and Mining Sciences, v. 43, no. 4, p. 647–654.

Coleman, T.I., Parker, B.L., Maldaner, C.H. and Mondanos, M.J. (2015): Groundwater flow characterization in a fractured bedrock aquifer using active DTS tests in sealed boreholes; Journal of Hydrology, v. 528, p. 449–462, URL <https://doi.org/10.1016/j.jhydrol.2015.06.061>.

Correa, J., Van Zaanen, L., Tertyshnikov, K., Dean, T., Pevzner, R. and Bona, A. (2017): DAS versus geophones: a quantitative comparison of a VSP survey at a dedicated field laboratory; European Association of Geoscientists and Engineers, Fourth EAGE Borehole Geophysics Workshop, November 19–22, 2017, Abu Dhabi, United Arab Emirates, v. 2017, p. 1–5, URL <https://doi.org/10.3997/2214-4609.201702477>.

Daley, T.M., Freifeld, B.M., Ajo-Franklin, J., Dou, S., Pevzner, R., Shulakova, V., Kashikar, S., Miller, D.E., Goetz, J., Henninges, J. and Lueth, S. (2013): Field testing of fiber-optic distributed acoustic sensing (DAS) for subsurface seismic monitoring; The Leading Edge, v. 32, no. 6, p. 699–706.

Damiano, E., Avolio, B., Minardo, A., Olivares, L., Picarelli, L. and Zeni, L. (2017): A laboratory study on the use of optical fibers for early detection of pre-failure slope movements in shallow granular soil deposits; Geotechnical Testing Journal, v. 40, no. 4, p. 529–541.

FBGS Technologies, GmbH (2022): FBG principle; FBGS Technologies, URL <https://fbgs.com/technology/fbg-principle/> [November 2022].

Ferdinand, P., Magne, S., Dewynter-Marty, V., Martinez, C., Rougeault, S. and Bugaud, M. (1997): Applications of Bragg grating sensors in Europe; 12th International Conference on Optical Fiber Sensors, Optica Publishing Group, October 28–31, 1997, Williamsburg, Virginia, OSA Technical Digest Series, v. 16, Paper OTuB1, URL <https://doi.org/10.1364/OFS.1997.OTuB1>.

Freifeld, B.M., Oldenburg, C.M., Jordan, P., Pan, L., Perfect, S., Morris, J., White, J., Bauer, S., Blankenship, D., Roberts, B., Bromhal, G., Glasser, D., Wyatt, D. and Rose, K. (2016): Well Integrity for Natural Gas Storage in Depleted Reservoirs and Aquifers; report prepared by Lawrence Berkeley National Laboratory (LBNL) for the U.S. Department of Energy, Office of Fossil Energy, Technical Report Series, no. LBNL-1006165, 89 p., URL <https://www.netl.doe.gov/research/on-site-research/publications/featured-technical-reports> [November 2022].

Gage, J.R., Fratta, D., Turner, A.L., MacLaughlin, M.M. and Wang, H.F. (2013): Validation and implementation of a new method for monitoring in situ strain and temperature in rock masses using fiber-optically instrumented rock strain and temperature strips; International Journal of Rock Mechanics and Mining Sciences, v. 61, p. 244–255.

Gage, J.R., Noni, N., Turner, A., MacLaughlin, M. and Wang, H.F. (2010): Fiber optic strain and temperature monitoring in crystalline rock at the Sanford Underground Science and Engineering Laboratory (SUSEL), Lead, South Dakota; American Rock Mechanics Association, 44th U.S. Rock Mechanics Symposium and 5th U.S.-Canada Rock Mechanics Symposium, June 27–30, 2010, Salt Lake City, Utah, Paper ARMA-10-367.

Gage, J.R., Wang, H.F., Fratta, D. and Turner, A.L. (2014): In situ measurements of rock mass deformability using fiber Bragg grating strain gauges; International Journal of Rock Mechanics and Mining Sciences, v. 71, p. 350–361.

Gage, J.R., Wang, H.F., MacLaughlin, M., Turner, A. and Pratta, D. (2011): A new method for measuring in situ strain in intact rock masses: fiber optically instrumented rock strain and temperature strips (FROSTS); American Rock Mechanics Association, 45th U.S. Rock Mechanics/Geomechanics Symposium, June 26–29, 2011, San Francisco, California, Paper ARMA-11-387.

Guo, X., Wang, B., Ma, Z. and Wang, Z. (2019): Testing mechanical properties of rock bolt under different supports using fiber Bragg grating technology; Sensors, v. 19, 19 p., URL <https://doi.org/10.3390/s19194098>.

Hartog, A.H. (2017): An Introduction to Distributed Optical Fibre Sensors; CRC Press, Boca Raton, Florida, 472 p., URL <https://doi.org/10.1201/9781315119014>.

Hu, K., Yao, Z., Wu, Y., Xu, Y., Wang, X. and Wang, C. (2022): Application of FBG sensor to safety monitoring of mine shaft lining structure; Sensors, v. 22, no. 13, art. 4838, URL <https://doi.org/10.3390/s22134838>.

Johny, J., Prabhu, R., Fung, W.K. and Watson, J. (2016): Investigation of positioning of FBG sensors for smart monitoring of oil and gas subsea structures; Institute of Electrical and Electronics Engineers, OCEANS 2016 Conference, April 13–16, 2016, Shanghai, China, 4 p., URL <https://doi.org/10.1109/OCEANSAP.2016.7485662>.

Jousset, P., Reinsch, T., Ryberg, T., Blanck, H., Clarke, A., Aghayev, R., Hersir, G.P., Henninges, J., Weber, M. and Krawczyk, C.M. (2018): Dynamic strain determination using fibre-optic cables allows imaging of seismological and structural features; Nature Communications, v. 9, no. 1, p. 1–11.

Karrenbach, M., Kahn, D., Cole, S., Ridge, A., Boone, K., Rich, J., Silver, K. and Langton, D. (2017): Hydraulic-fracturing-induced strain and microseismic using in situ distributed fiber-optic sensing; The Leading Edge, v. 36, no. 10, p. 837–844.

Lei, X., Xue, Z. and Hashimoto, T. (2019): Fiber optic sensing for geomechanical monitoring: (2)-distributed strain measurements at a pumping test and geomechanical modeling of deformation of reservoir rocks; Applied Sciences, v. 9, no. 3, art. 417, URL <https://doi.org/10.3390/app9030417>.

Li, Y., Wu, H., Wong, W., Hewett, B., Liu, Z., Mateeva, A. and Lopez, J. (2015): Velocity analysis and update with 3D DAS-VSP to improve borehole/surface seismic images; Society of Exploration Geophysicists, 85th Annual Meeting, October 18–23, 2015, New Orleans, Louisiana, Technical Program Expanded Abstracts, p. 5285–5289, URL <https://doi.org/10.1190/segam2015-5864923.1>.

Lindsey, N., Dawe, C. and Ajo-Franklin, J. (2019): Photonic seismology in Monterey Bay: dark fiber DAS illuminates offshore faults and coastal ocean dynamics; EarthArXiv, preprint, URL <https://doi.org/10.31223/osf.io/7bf92>.

Lindsey, N.J., Martin, E.R., Dreger, D.S., Freifeld, B., Cole, S., James, S.R., Biondi, B.L. and Ajo-Franklin, J.B. (2017): Fiber-optic network observations of earthquake wavefields; Geophysical Research Letters, v. 44, no. 23, p. 11,792–11,799.

Martin, E.R., Biondi, B.L., Karrenbach, M. and Cole, S. (2017): Continuous subsurface monitoring by passive seismic with distributed acoustic sensors-the “Stanford Array” experiment; European Association of Geoscientists and Engineers, First EAGE Workshop on Practical Reservoir Monitoring, March 6–9, 2017, Amsterdam, Netherlands, cp-505-00018, URL <https://doi.org/10.3997/2214-4609.201700017>.

Mateeva, A., Mestayer, J., Cox, B., Kiyashchenko, D., Wills, P., Lopez, J., Grandi, S., Hornman, K., Lumens, P., Franzen, A., Hill, D. and Roy, J. (2012): Advances in distributed acoustic sensing (DAS) for VSP; Society of Exploration Geophysicists, 82nd Annual Meeting, November 4–9, 2012, Las Vegas, Nevada, Technical Program Expanded Abstracts, p. 1–5, URL <https://doi.org/10.1190/segam2012-0739.1>.

Minardo, A., Catalano, E., Coscetta, A., Zeni, G., Zhang, L., Di Maio, C., Vassallo, R., Coviello, R., Macchia, G., Picarelli, L. and Zeni, L. (2018): Distributed fiber optic sensors for the monitoring of a tunnel crossing a landslide; Remote Sensing, v. 10, no. 8, art. 1291, URL <https://doi.org/10.3390/rs10081291>.

Morey, W.W., Meltz, G. and Glenn, W.H. (1990): Fiber optic Bragg grating sensors; *in* Fiber optic and laser sensors VII, R.P. DePaula and E. Udd (ed.); Society of Photographic Instrumentation Engineers, v. 1169, p. 98–107, URL <https://doi.org/10.1117/12.963022>.

Ni, J., Wang, C., Shang, Y., Zhang, X. and Zhao, Y. (2018): Distributed fiber-optic acoustic sensing for petroleum geology exploration; Journal of Physics, Conference Series, v. 1065, no. 25, 4 p., art. 252029, URL <https://doi.org/10.1088/1742-6596/1065/25/252029>.

Nicholas, E. and De Joode, A. (2022): Considering data coupling distributed temperature sensing with real time transient modeling for pipeline leak detection; Pipeline Simulation Interest Group, 52nd Annual Conference, May 10–13, 2022, San Diego, California, paper no. PSIG-2210.

Patterson, J.R., Cardiff, M., Coleman, T., Wang, H., Feigl, K.L., Akerley, J. and Spielman, P. (2017): Geothermal reservoir characterization using distributed temperature sensing at

Brady Geothermal Field, Nevada; The Leading Edge, v. 36, no. 12, p. 1024a1–1024a7.

Pendão, C. and Silva, I. (2022): Optical fiber sensors and sensing networks: overview of the main principles and applications; Sensors, v. 22, no. 19, art. 7554, URL <https://doi.org/10.3390/s22197554>.

Qiao, X., Shao, Z., Bao, W. and Rong, Q. (2017): Fiber Bragg grating sensors for the oil industry; Sensors, v. 17, no.3, art. 429, URL <https://doi.org/10.3390/s17030429>.

Quinn, M.C. (2021): Geotechnical effects on fiber optic distributed acoustic sensing performance; Ph.D. thesis, University of Rhode Island, 162 p., URL <https://doi.org/10.23860/Quinn-Meghan-2021>.

Ravet, F., Chin, S., Briffod, F. and Rochat, E. (2019): Simple method for DTS/DSS data interpretation: an application to pipeline geotechnical monitoring; American Society of Mechanical Engineers, International Pipeline Geotechnical Conference, June 25–27, 2019, Buenos Aires, Argentina, paper no. IPG2019-5332, 13 p., URL <https://doi.org/10.1115/IPG2019-5332>.

Ravet, F., Niklès, M. and Rochat, E. (2017): A decade of pipeline geotechnical monitoring using distributed fiber optic monitoring technology; American Society of Mechanical Engineers, International Pipeline Geotechnical Conference, July 25-26, 2017, Lima, Peru, paper no. IPG2017-2503, 13 p., URL <https://doi.org/10.1115/IPG2017-2503>.

Read, T., Bense, V.F., Bour, O., Le Borgne, T., Lavenant, N., Hochreutener, R. and Selker, J.S. (2015): Thermal-plume fibre optic tracking (T-POT) test for flow velocity measurement in groundwater boreholes; Geoscientific Instrumentation, Methods and Data Systems, v. 5, no. 5, p. 161–175, URL <https://doi.org/10.5194/gid-5-161-2015>.

Rong, Q. and Qiao, X. (2019): FBG for oil and gas exploration; Journal of Lightwave Technology, v. 37, no. 11, p. 2502–2515.

Sakaguchi, K. and Matsushima, N. (2000): Temperature logging by the distributed temperature sensing technique during injection tests; International Geothermal Association, Proceedings of the World Geothermal Congress, May 28–June 10, 2000, Kyushu-Tohoku, Japan, p. 1657–1661.

Sellwood, S.M., Hart, D.J. and Bahr, J.M. (2015): An in-well heat-tracer-test method for evaluating borehole flow conditions; Hydrogeology Journal, v. 23, no. 8, p. 1817–1830.

Tang, B., Cheng, H., Tang, Y., Yao, Z., Rong, C., Xue, W. and Lin, J. (2018): Application of a FBG-based instrumented rock bolt in a TBM-excavated coal mine roadway; Journal of Sensors, v. 2018, p. 1–10, URL <https://doi.org/10.1155/2018/8191837>.

Vlachopoulos, N., Cruz, D. and Forbes, B. (2018): Utilizing a novel fiber optic technology to capture the axial responses of fully grouted rock bolts; Journal of Rock Mechanics and Geotechnical Engineering, v. 10, no. 2, p. 222–235.

Wang, H. and Gage, J. (2017): Fiber-Optic Monitoring in Underground Rock Engineering; Rock Mechanics and Engineering, X.T. Feng (ed.), v. 4, CRC Press, London, England, p. 529–560, URL <https://doi.org/10.1201/b20406>.

Wang, Z., Li, W., Wang, Q., Hu, Y. and Du, J. (2021): Monitoring the dynamic response of the overlying rock–soil composite structure to underground mining using BOTDR and FBG sensing technologies; Rock Mechanics and Rock Engineering, v. 54, no. 9, p. 5095–5116.

Webster, P., Wall, J., Perkins, C. and Molenaar, M. (2013): Microseismic detection using distributed acoustic sensing; Society of Exploration Geophysicists, 83rd Annual Meeting, September 22–27, 2013, Houston, Texas, Technical Program Expanded Abstracts, p. 2459–2463, URL <https://doi.org/10.1190/segam2013-0182.1>.

White, D., Daley, T.M., Paulsson, B. and Harbert, W. (2021): Borehole seismic methods for geologic CO_2 storage monitoring; The Leading Edge, v. 40, no. 6, p. 434–441.

Xu, S., Wang, S., Zhang, P., Yang, D. and Sun, B. (2020): Study on strain characterization and failure location of rock fracture process using distributed optical fiber under uniaxial compression; Sensors, v. 20, no. 14, art. 3853, URL <https://doi.org/10.3390/s20143853>.

Xu, S., Zhang, P., Zhang, D., Wu, R. and Guo, L. (2015): Simulation study of fiber optic monitoring technology of surrounding rock deformation under deep mining conditions; Journal of Civil Structural Health Monitoring, v. 5, no. 5, p. 563–571.

Xue, Z., Park, H., Kiyama, T., Hashimoto, T., Nishizawa, O. and Kogure, T. (2014): Effects of hydrostatic pressure on strain measurement with distributed optical fiber sensing system; Energy Procedia, v. 63, p. 4003–4009.

Yin, J., Zhu, H., Fung, K.W., Jin, W., Mak, L.M. and Kuo, K. (2008): Innovative optical fiber sensors for monitoring displacement of geotechnical structures; Hong Kong Institution of Engineers, Geotechnical Division 28th Annual Seminar, January 1, 2008, Hong Kong, p. 100–108.

Yugay, V., Mekhtiyev, A., Madi, P., Neshina, Y., Alkina, A., Gazizov, F., Afanaseva, O. and Ilyashenko, S. (2022): Fiber-optic system for monitoring pressure changes on mine support elements; Sensors, v. 22, no. 5, art. 1735, URL <https://doi.org/10.3390/s22051735>.

Zhang, S., Liu, H., Cheng, J. and DeJong, M.J. (2020): A mechanical model to interpret distributed fiber optic strain measurement at displacement discontinuities; Structural Health Monitoring, URL <https://doi.org/10.1177/1475921720964183>.

Zhang, X., Liu, X., Zhang, F., Sun, Z., Min, L., Li, S., Jiang, S., Li, M., Wang, C. and Ni, J. (2018): Reliable high-sensitivity FBG geophone for low-frequency seismic acquisition; Measurement, v. 129, p. 62–67.

Zhao, Y., Zhang, N. and Si, G. (2016): A fiber Bragg grating-based monitoring system for roof safety control in underground coal mining; Sensors, v. 16, no. 10, art. 1759, URL <https://doi.org/10.3390/s16101759>.

Zhong, Z.Y., Zhi, X.L. and Yi, W.J. (2007): Oil well real-time monitoring with downhole permanent FBG sensor network; Institute of Electrical and Electronics Engineers, International Conference on Control and Automation, May 30–June 1, 2007, Guangzhou, China, p. 2591–2594.

Summary of a Numerical Investigation of the Red Chris Operations in Northern British Columbia (NTS 104H/12W) Using the Finite-Discrete Element Method

T. Shapka-Fels[1], Norman B. Keevil Institute of Mining Engineering, The University of British Columbia, Vancouver, British Columbia, tfels@student.ubc.ca

Shapka-Fels, T. (2023): Summary of a numerical investigation of the Red Chris operations in northern British Columbia (NTS 104H/12W) using the Finite-Discrete Element Method; *in* Geoscience BC Summary of Activities 2022: Minerals, Geoscience BC, Report 2023-01, p. 71–78.

Introduction

The transition of open pit to cave mining results in dynamic multidisciplinary challenges during design, operation and closure. The objective of the research summarized in this paper is to investigate the role of numerical analysis applied to the transition problem, and to develop models to understand the geomechanical interaction between open pit and cave mining based on different geological and mine-design variables. Models with special consideration of the planned caving operation at the Red Chris operations (Red Chris) in northern British Columbia (BC) were created using publicly available data.

This paper summarizes the development and highlights results of selected Finite-Discrete Element Method (FDEM) models of the Red Chris operations, as part of research published by Shapka-Fels (2022). The numerical models were developed using the hybrid continuum-discontinuum method, with the software package Elfen (v. 5.2.6) created by Rockfield (2020). FDEM allows for simulation of intact-rock strength parameters; existing fracture networks and geological structures; fracture development due to changes in stress; and kinematic failure mechanisms.

These models represent further study into the numerical modelling challenges in large-scale rock engineering problems, as discussed by Shapka-Fels and Elmo (2022). This study of the Red Chris operations was not sponsored by Newcrest Mining Limited or Imperial Metals Corporation. The study presented herein only utilizes what is publicly available to provide insight into FDEM modelling conceptualization and parameters, and is not intended to replicate conditions at the Red Chris operations or to make technical or financial decisions.

[1]*The lead author is a 2022 Geoscience BC Scholarship recipient.*

This publication is also available, free of charge, as colour digital files in Adobe Acrobat® PDF format from the Geoscience BC website: http://geosciencebc.com/updates/summary-of-activities/.

Red Chris Operations

The Red Chris operations, located in northwestern BC (Figure 1), comprise a currently operating open-pit mine and a planned block-cave underground operation. This copper-gold asset is managed by a joint venture between subsidiaries owned by Newcrest Mining Limited and Imperial Metals Corporation. Combined open-pit and block-cave mine operations were considered at Red Chris prior to commencing mine construction in 2012 (Gillstrom et al., 2012). Updated technical studies forecast the open pit to be completed in 2026, with early cave production planned for the same year (Stewart et al., 2021).

Model Assumptions and Scenarios

Published information from the 2021 *Red Chris Block Cave Pre-Feasibility Study (PFS)*, as outlined in the latest NI 43-101 technical report (Stewart et al., 2021), was used for the conceptualization of numerical models in this study and is herein referred to as the '2021 PFS'. Certain assumptions for modelling inputs were used to supplement published information. These include base assumptions and variations for model scenarios in terms of material parameters, major structures and preconditioning. The base-case model scenario and three comparative scenarios were selected for discussion in this paper (Table 1).

Material Parameters

The material parameters used for the Red Chris FDEM models were based on the material parameters for a mine within a similar deposit type.

The material properties for the South Boundary fault zone were approximated, assuming the fault zone is a weak heterogeneous mixture of gouge, breccia and gravel-size clasts. The clayey and granular material is simulated as a weak but brittle material, which will not fail in the FDEM model as it may in reality. This is an important limitation with this method of numerical analysis.

Upscaled material parameters were tested as an attempt to increase the computing speed of the FDEM models. The base FDEM model geometry was re-meshed to a size of 4 m

Figure 1. Location of the Red Chris operations in northwestern British Columbia.

within the cave propagation zone, and material properties were upscaled. Different upscaling assumptions were applied based on approaches of modifying the intact-rock parameters (i.e., unconfined compressive strength [UCS]) or the Geological Strength Index (GSI), proposed by Elmo et al. (2010), Elmo and Stead (2017) and Guajardo (2020). This paper presents the results of one scenario tested to highlight the importance of understanding upscaling limitations.

Structure

Subvertical features are important with regard to caving propagation, thus the evaluation of different structural scenarios was included in the FDEM model investigation. Structural variations were investigated: the first structural scenario contained all the discrete faults within the 2021 PFS, while alternative structural patterns derived from Rees et al. (2015) consider a more complex structural framework that includes primary and secondary structures (splays and relays). The alternative scenarios considered the replacement of moderately dipping faults with two steeply dipping structures that were modified from the interpretation of the Dead Zone (DZ) fault zone presented in Rees et al. (2015).

Preconditioning

Preconditioning was simulated within the FDEM models as pre-existing horizontal fractures, starting several metres above the undercut level (UCL) and continuing up toward the pit floor. Variations in the height of preconditioning and horizontal extent of the fractures were tested, with one case presented in this paper. The fractures were not continuous through faults and fault zones due to induced damage within the models at intersections and a conceptual idea that the fractures would not propagate through the heterogeneous cataclastic rock material within large fault zones.

Development of the FDEM Model

The schematic cross-section used in subsidence modelling for the 2021 PFS (location shown in Figure 2) was the basis of the primary FDEM model geometry (Figure 3). The section comprises a UCL that is 715 m below an approximately 300 m deep open pit with a northwest overall slope angle of 40° and a southeast overall slope angle of 37°. The caving UCL is 360 m in width, with an initial excavation height of 1 m. The entirety of the model measures 2640 m by 1100 m,

Table 1. Selected 2-D conceptual Finite-Discrete Element Method (FDEM) modelling scenarios for the Red Chris operations.

Model	Description
2.1	Base case scenario.
2.6	Upscaling materials using 88% unconfined compressive strength. Scaled caving area mesh size from 2 m to 4 m.
2.7	Modified structural pattern with steeply dipping faults and shallow northwest-dipping faults.
2.11	Modified structural pattern with steeply dipping faults and shallow northwest-dipping faults. Hydrofractures span the footprint laterally with partial extension of 40 m to the northwest. The hydrofractures continue at 4 m spacing vertically to midway between the undercut level and pit floor.

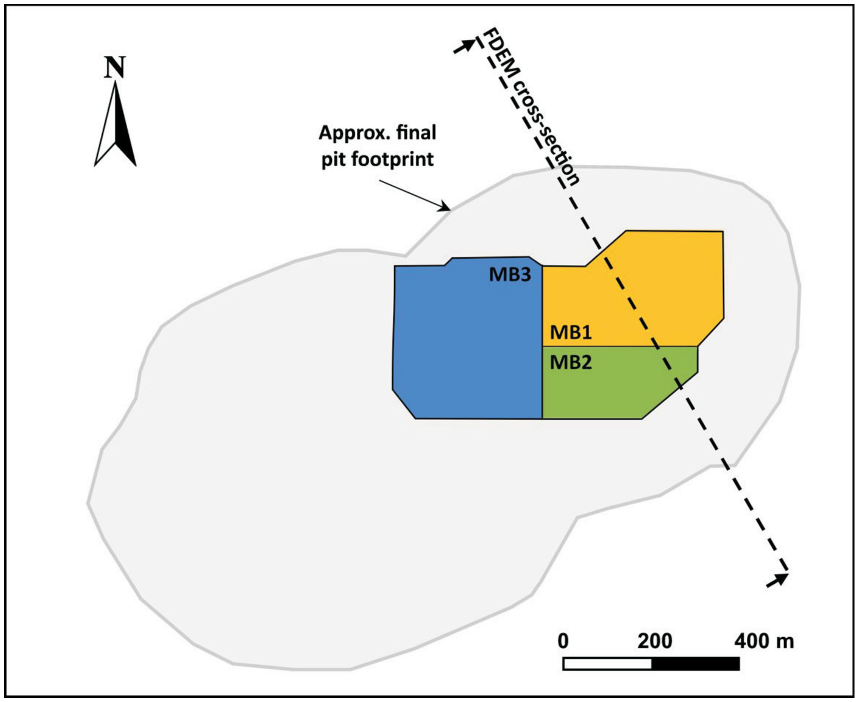

Figure 2. Location of cross-section used in FDEM modelling, relative to the Red Chris final pit footprint and macroblocks.

subdivided into elastic and elastoplastic regions with fracturing. The nonfracturing elastic region is required to minimize boundary effects and is modelled with a lower mesh resolution. The open pit is modelled elastically and excavated in four 70–80 m stages. The structures considered in all models include the South Boundary fault zone and the East Zone (EZ) fault. Alternate structural scenarios replace the Hanging Wall (HW1 and HW2) faults in the primary FDEM model with reinterpreted faults in the DZ fault zone and include shallow dipping faults.

Mesh resolution varies at 1 m within the UCL and 2 m above the undercut up to the pit bottom, and increases to 40 m near the model boundaries. The upscaled scenarios have a mesh size of 4 m within the cave propagation zone

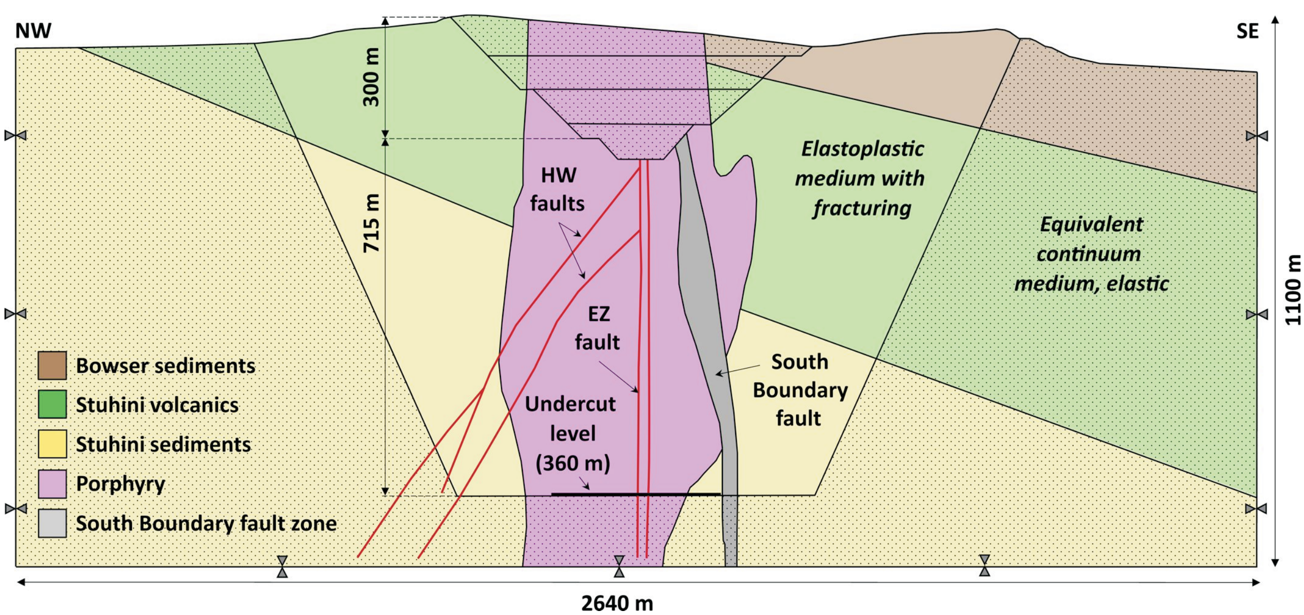

Figure 3. Schematic diagram of base FDEM geometry and boundary conditions for Red Chris Models 2.1 and 2.6. Dotted regions indicate elastic material, while solid regions are modelled as elastoplastic regions with fracturing. Abbreviations: EZ, East Zone (Fault); HW, Hanging Wall (Fault); NW, northwest; SE, southeast.

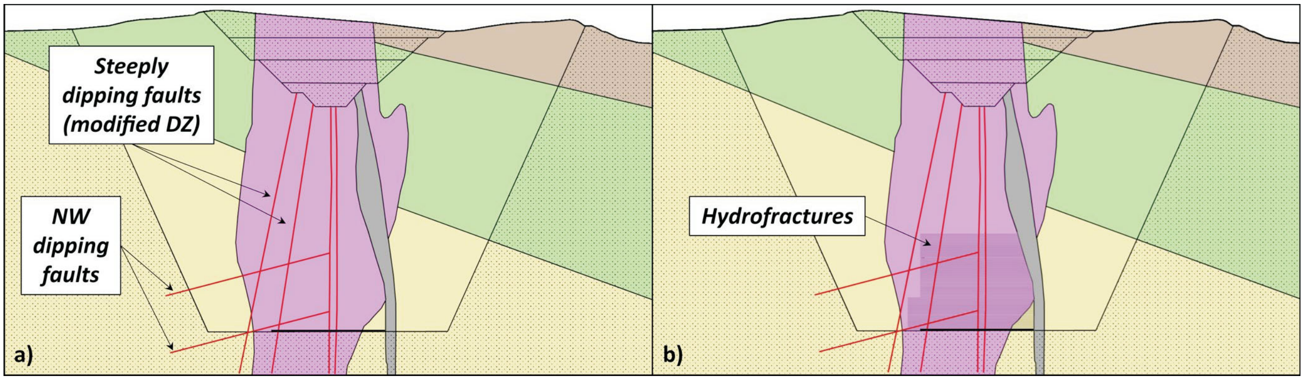

Figure 4. Schematic diagrams illustrating variations from the base FDEM geometries for **a)** Red Chris Model 2.7, with an alternate structural setting, and **b)** Red Chris Model 2.11, with an alternate structural setting and preconditioning. Abbreviations: DZ, Dead Zone (Fault), NW, Northwest.

(changed from 2 m). Model geometry variations described in Table 1 are illustrated in Figure 4.

Results from the FDEM Model

Conceptual Red Chris–based FDEM models were created to investigate the effects of structural variability, material upscaling and preconditioning. Due to the variation in model timing, comparable models were selected at a specific 2-D production value. Model results are presented after a 2-D production of 21 300 m^2 ± 5% (Figures 5–8). Height of draw (HOD) is reported as the maximum Y displacement, and model time is reported as time past the first deletion. Crater depth corresponds to the Y displacement at the pit floor.

In the majority of the models, slope failure and mobilization occurred due to caving-induced unloading; however, the magnitude of movement varied greatly between models.

The following subsections contain observations for each model based on the differences relative to Model 2.1 (Figure 5) at the same level of 2-D production, unless otherwise specified. Differences in total displacement (XY), HOD and model run times are reported in the corresponding summary figures. The resulting figures showcase the area of in-

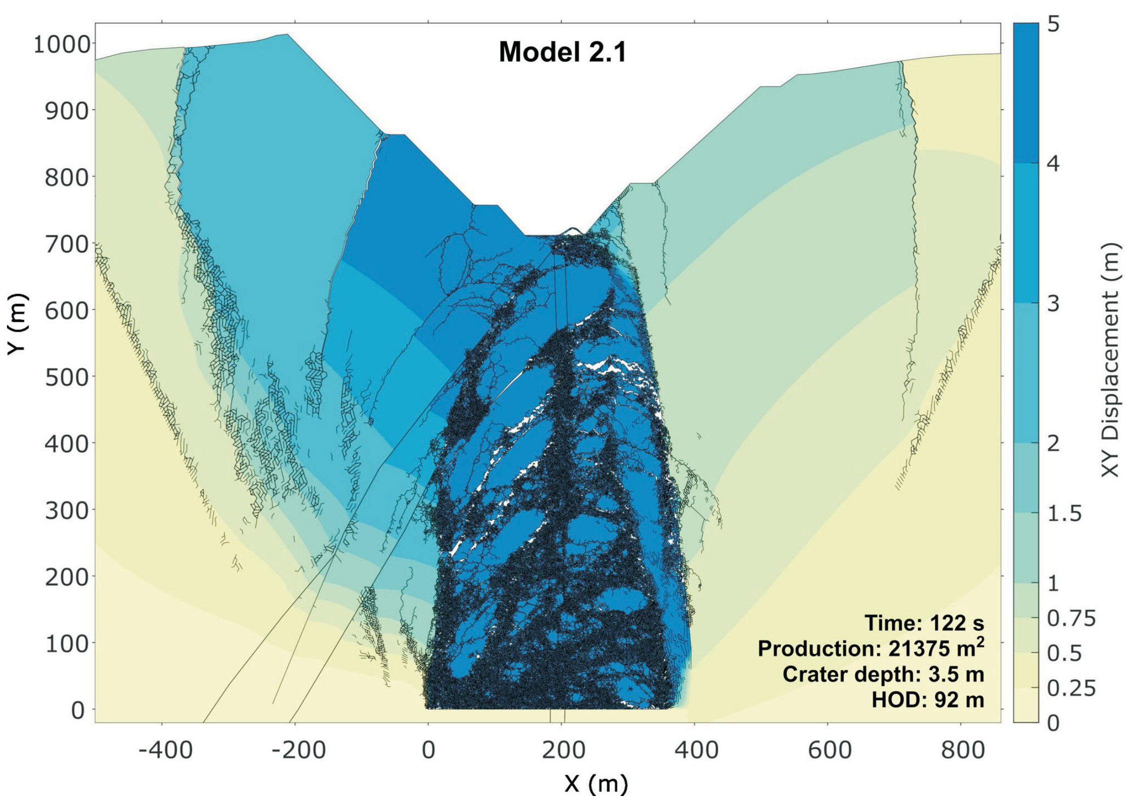

Figure 5. FDEM results for Red Chris Model 2.1, with XY displacement (m) contours. Abbreviations: HOD, height of draw (maximum vertical displacement at undercut level).

terest (i.e., fracturing area) within the overall model boundaries.

Model 2.1 (Figure 5) exhibits early fracturing (prior to cave initiation) near the pit floor resulting from the intersecting faults and rebound post excavation. Displacement of the lower southeast inter-ramp slope can be attributed to the weak material of the South Boundary fault zone. Maximum vertical displacement was located on the northwest side of the UCL, as expected with the draw sequence and timing.

The cave propagated at a greater rate southeast of the EZ faults, likely due to the stress conditions resulting in a greater stress ratio between the subvertical faults and the South Boundary fault zone. The HW faults provided some level of resistance to cave propagation; however, continued production and displacement of the northwest pit slope rendered these structures obsolete. The southeast boundary of the South Boundary fault zone limited the extent of the caved material, until production was such that major fracturing extended to the southeastern lithological contact of the Porphyry and the Stuhini volcanics. Due to the orientation of the South Boundary fault zone, continued production resulted in enough vertical displacement that an overhang was created. Without support of caved material below, the overhanging material fell and much of the southeast pit wall was included in the main cave body.

Upscaling Method

Model 2.6 (Figure 6) was selected to highlight the effects of upscaling. Model 2.6 was the only model in this study resulting in a stalled cave propagation and a large air gap. This model is significant because it exemplifies how material-input parameters are not independent from the mesh size. Without reducing the material strength enough to account for the mesh size increase, the model results in a very different outcome.

There was minimal interaction between the cave and the open pit. The cave started stalling at a stage of propagation similar to Model No. 2.1 at 97 seconds (48 seconds past first deletion), and the air gap continued to grow as production continued. Despite the stress concentration, the fracturing did not continue because of the relative strength of the material.

Structural Pattern

The Red Chris Model 2.7 (Figure 7) was selected to highlight the effects of different structural scenarios on cave propagation, particularly discrete subvertical faults. The main fracturing area in Model 2.7 was controlled by the modified DZ faults, resulting in narrowing as the cave propagated toward the pit bottom. The fracturing is more limited by the southeast DZ fault because fracturing did not

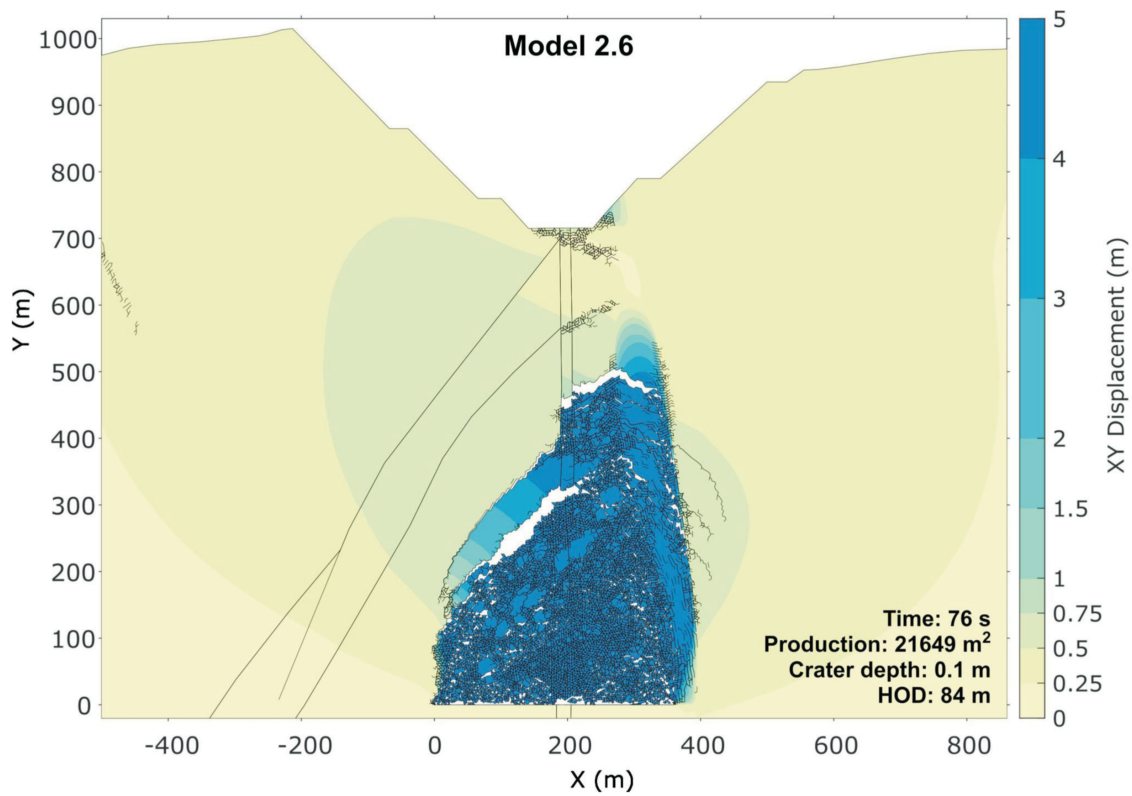

Figure 6. FDEM results for Red Chris Model 2.6, with XY displacement (m) contours. Abbreviations: HOD, height of draw (maximum vertical displacement at undercut level).

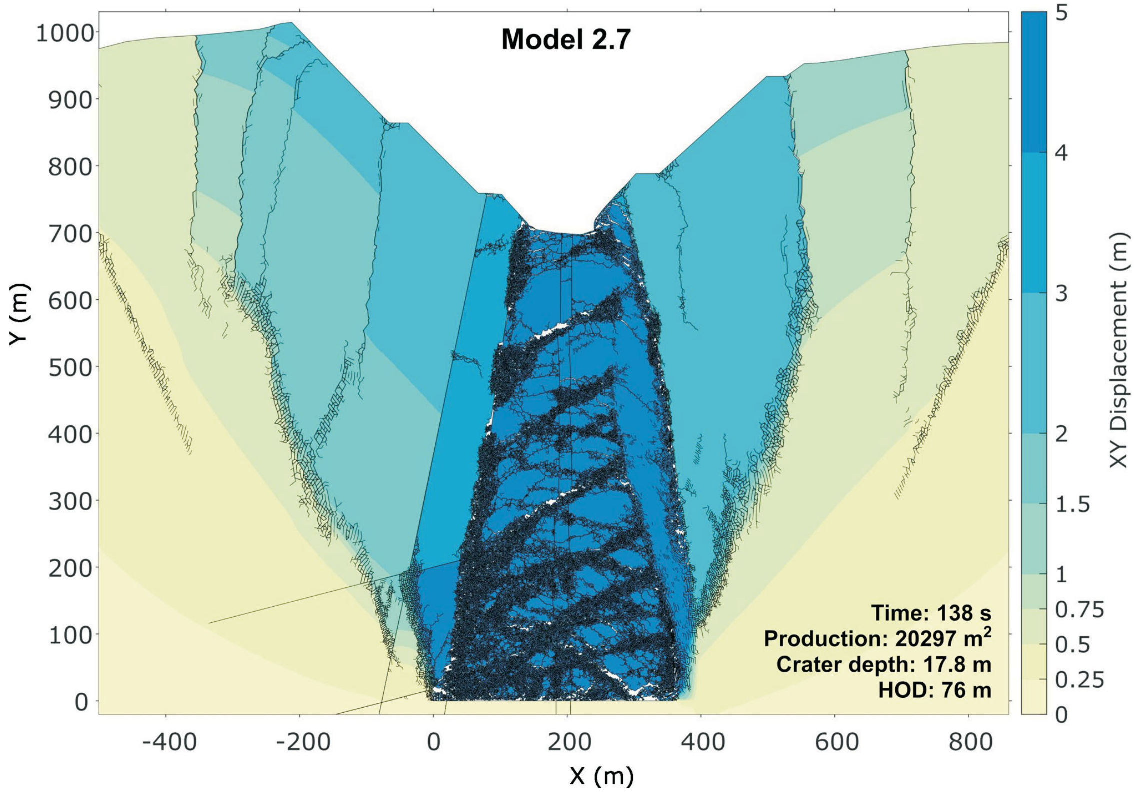

Figure 7. FDEM results for Red Chris Model 2.7, with XY displacement (m) contours. Abbreviations: HOD, height of draw (maximum vertical displacement at undercut level).

continue through the discrete feature, except where the shallow dipping faults intersected the DZ faults above the UCL. Cave propagation was overall more symmetrical with this structural scenario, as the high stress ratio (and horizontal stresses) were distributed between the South Boundary fault zone and the DZ faults. The larger subsidence zone included both pit walls up to the top of the pit, also with more symmetrical displacement.

Higher initial vertical displacement (defined by 1 m of movement) occurred on the southeast side of the UCL; however, subsequent vertical displacement was higher on the northwest side, as per the production sequencing. Increased fracturing occurred in a pattern of bands that dip at shallow to moderate angles toward the northwest, with lesser conjugate bands dipping to the southeast.

Preconditioning

Model 2.11 was selected to highlight the effects of preconditioning (Figure 8), using pre-existing horizontal discontinuities. This model contained the same structural pattern as Model 2.7. In comparison to Model 2.7, the addition of hydrofractures resulted in a more symmetrical and centralized cave propagation with less deformation of the pit slopes above the lower ramps (Figure 7).

Fragmentation resulting from the introduction of hydrofractures increased relative to the spacing heights between hydrofractures. Above the hydrofractures, increased fracturing occurred along the southeast DZ fault, but significant deformation occurred between the two DZ faults as well. This could be attributed to the hydrofractures causing fracturing damage and connection between the two faults, in contrast to Model 2.7 (at earlier stages).

The contrast between the continuum material and the hydrofractured areas provided a boundary for caving-induced fracturing to follow, limiting the extent of fracturing beyond the hydrofractured areas. However, extending the hydrofractures outside the footprint area did not cause increased fragmentation, fracturing or recovery of material in that area. Increasing the height of hydrofractures in this extended area may have caused better connection between the shallow dipping faults (as seen in Model 2.7, Figure 8), resulting in a different magnitude of deformation on the northwest side.

Learnings

An FDEM investigation was completed for a case study on the Red Chris operations and planned block-cave mine, albeit with many assumptions applied due to the lack of publicly available geotechnical information. The models presented in this paper are considered investigative forward-analysis models, created to further understand cause-and-effect of upscaling, structural geology and preconditioning

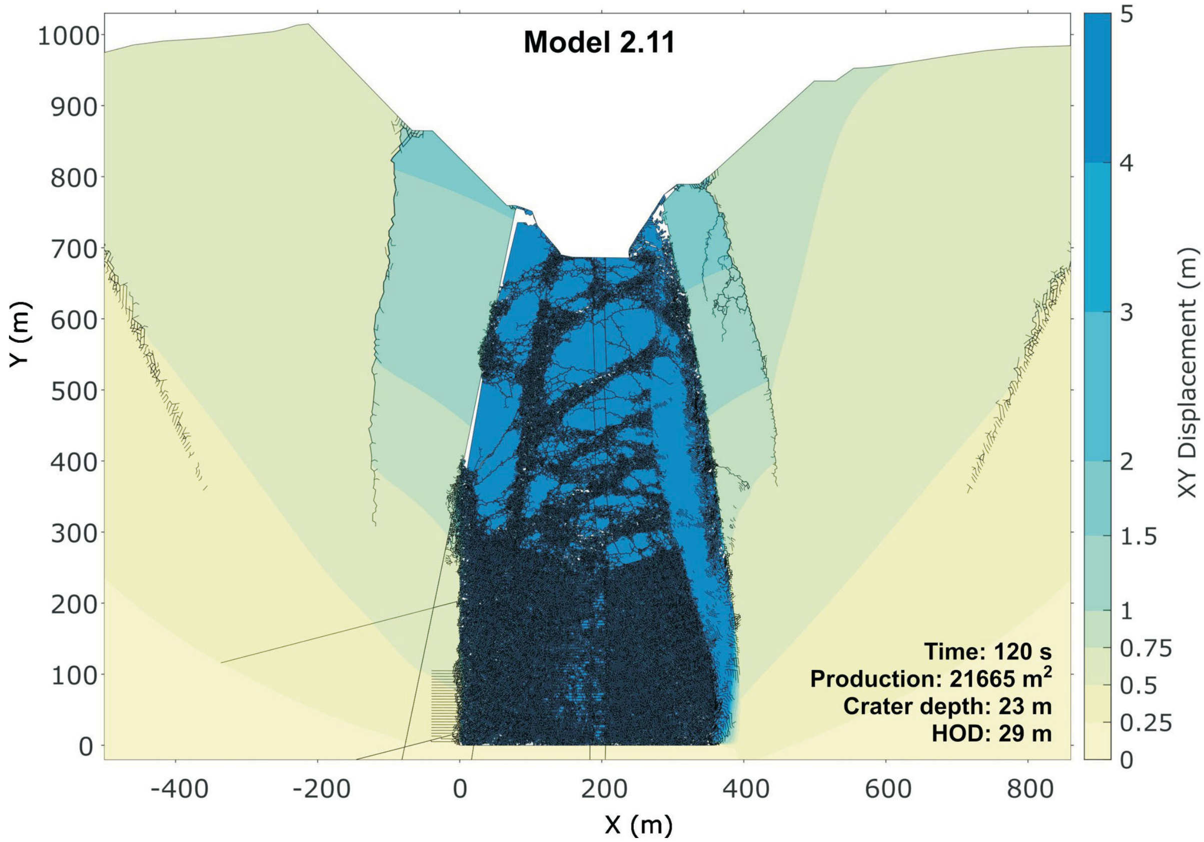

Figure 8. FDEM results for Red Chris Model 2.11, with XY displacement (m) contours. Abbreviations: HOD, height of draw (maximum vertical displacement at undercut level).

to predict cave-propagation processes. Results were presented based on each individual model; however, the key learnings from these models extend beyond the individual scenarios. While these models are 2-D, the same limitations discussed would apply to 3-D models, although 3-D models with the same fracturing capabilities would have significantly greater run times, thus rendering them impractical for investigative risk-based analysis. Key learnings from the Red Chris FDEM models are grouped under the following five subsections.

Common Modelling Artifacts

Large tension cracks occur in most models, resulting in significant deformation of the pit slopes. In models without a discrete fracture network (DFN), tension cracks may form due to the buildup of strain within the rock-mass continuum. Generally, cracks preferentially develop along material boundaries, whether lithological or defined fracturing limits. Also related to continuum-modelling artifacts is the fracturing damage at fault intersections due to the concentration of movement toward and along those discrete fault planes when the rest of the rock mass is modelled as a continuum (i.e., no DFN).

After large excavations, such as the excavation of the pit, the rebound of unexcavated material may cause fracturing, particularly in the pit floor. Increasing relaxation times and equilibrium stages may reduce fracturing, but this possibility was not tested as part of this study. Beams of unbroken elements form near the pit floor after deformation of the pit slopes cause squeezing. The cut-off strength between elements has not been reached, and these beams can be considered a relic of continuum rock masses. These beams also commonly occur when modelling hydrofractures as straight and horizontal features.

Induced-Stress Field

The stress ratio increases (i.e., horizontal stresses greater) below the pit floor as the pit is excavated. Early stages of caving result in horizontal stresses concentrating between subvertical faults within the cave-propagation zone, as the horizontal stresses cannot be transmitted across the discrete features. In models that contain hydrofractures, high stress ratios occur in an ellipsoidal shape centred above the caved material, as well as between subvertical faults. This is likely the cause of the increased speed of vertical movement of the cave back, and is due to the limited translation of vertical stresses across the horizontal fractures.

Fault-Material Parameters

If a particular fault zone has a high composition of granular material, it would be expected to unravel into the caved material and increase fines reporting to the production level. However, the mesh size is a limiting factor to model this concept, as it would have to be significantly finer to capture the same process.

Upscaling

Properties of rock-mass material are not unique to the geotechnical domain, but rather to both the material and the scale of discretization. Often, materials are modelled with a change in discretization scale such that mesh sizes are smaller in regions where fracturing is more expected. This raises an important consideration: with material parameters dependent on mesh size, when does a modeller start upscaling?

Preconditioning

Preconditioning changes the stress regime significantly, with early vertical propagation of the cave reaching the pit floor at lower production levels. The hydrofractures also add contrast boundaries, resulting in certain control over the location of cave propagation. However, adding hydrofractures above the UCL but outside the footprint area may not increase recovery.

Modelling hydrofractures comes with another suite of challenges, regardless of modelling method. Decisions include whether hydrofractures remain continuous through faults and the timeline of their creation (i.e., cannot be inserted at different stages). There is also limited understanding of how to implement realistic development of fractures during the preconditioning process due to incremental changes in principal stress orientation.

Conclusions

This paper highlights a portion of a completed thesis with research that has contributed to the field of numerical analysis in rock engineering by highlighting important aspects of numerical analysis applied to the study of large-scale problems, particularly pit-to-cave transition.

In FDEM models, a large focus of the process and conceptualization should be on rock-mass discontinuities—whether they be major structural features (i.e., faults and fault zones), discrete fracture networks and rock-mass fabrics, or induced hydrofractures for preconditioning for caving. These features impact primary failure mechanisms observed in the open pit–to–cave FDEM models, as well as magnitude of deformation, due to their effects on stress continuity.

Acknowledgments

The author would like to acknowledge D. Elmo (University of British Columbia) and L. Zorzi (Golder/WSP) for providing comments and assistance, and the financial contributions of Geoscience BC through their graduate scholarship program.

References

Elmo, D., Rogers, S., Beddoes, R. and Catalan, A. (2010): An integrated finite/discrete element method – discrete fracture network synthetic rock mass approach for the modelling of surface subsidence associated with panel cave mining at the Cadia East underground project; *in* Caving 2010: Proceedings of the Second International Symposium on Block and Sublevel Caving, Y. Potvin (ed.), Australian Centre for Geomechanics, April 20–22, 2010, Perth, Australia, p. 167–179, URL <https://doi.org/10.36487/ACG_rep/1002_9_Elmo>.

Elmo, D. and Stead, D. (2017): Applications of fracture mechanics to rock slopes; Chapter 23 *in* Rock Mechanics and Engineering, Volume 3: Analysis, Modeling & Design, X.-T. Feng (ed.), CRC Press, p. 705–735, URL <https://doi.org/10.1201/b20402>.

Gillstrom, G., Anand, R., Robertson, S. and Sterling, P. (2012): 2012 technical report on the Red Chris copper-gold project; National Instrument 43-101 report prepared for Imperial Metals Corporation, 334 p., URL <https://imperialmetals.com/assets/docs/2012-Red-Chris-43-101-Report.pdf> [March 2021].

Guajardo, C.A. (2020): Numerical investigation on strength upscaling and its application to a back analysis of an open pit slope failure; M.A.Sc. thesis, The University of British Columbia, 136 p., URL <https://open.library.ubc.ca/soa/cIRcle/collections/ubctheses/24/items/1.0388530> [November 2022].

Rees, C., Riedell, K.B., Proffett, J.M., Macpherson, J. and Robertson, S. (2015): The Red Chris porphyry copper-gold deposit, northern British Columbia, Canada: igneous phases, alteration, and controls of mineralization; Economic Geology, v. 110, no. 4, p. 857–888, URL <https://doi.org/10.2113/econgeo.110.4.857>.

Rockfield (2020): Elfen version 5.2.6; Rockfield Software Ltd., URL <https://www.rockfieldglobal.com> [November 2022].

Shapka-Fels, T. (2022): Numerical analysis of the geomechanical interaction between open pit and cave mining using the hybrid finite-discrete element method; M.A.Sc. thesis, The University of British Columbia, 138 p., URL <https://open.library.ubc.ca/soa/cIRcle/collections/ubctheses/24/items/1.0418437> [November 2022].

Shapka-Fels, T. and Elmo, D. (2022): Numerical modelling challenges in rock engineering with special consideration of open pit to underground mine interaction; Geosciences, v. 12, no. 5, p. 199, URL <https://doi.org/10.3390/geosciences12050199>.

Stewart, R., Swanson, B., Sykes, M., Reemeyer, L., Wang, B. and Stephenson, P. (2021): Red Chris Operations, British Columbia, Canada, NI 43-101 Technical Report; National Instrument 43-101 report prepared for Newcrest Mining Ltd. and Imperial Metals Corporation, 285 p., URL <https://www.newcrest.com/sites/default/files/2021-11/211130_Newcrest%20Technical%20Report%20on%20Red%20Chris%20Operations%20as%20of%2030%20June%202021.pdf> [March 2022].

Geoscience BC

SUITE 1101–750 WEST PENDER ST
VANCOUVER, BC V6C 2T7 CANADA

604 662 4147

info@geosciencebc.com
geosciencebc.com